Study of the Sensitivity to Flavour-Specific Asymmetries with the LHCb Detector

Paul Szczypka

A dissertation submitted to the University of Bristol in accordance with the requirements of the degree of PhD in the Faculty of Science, Department of Physics

Abstract

LHCb is a future detector which will take data at the CERN Large Hadron Collider proton-proton collider. It is optimised for B-physics and will make precision measurements of $\mathcal{CP}$ violation parameters and flavour mixing. Measurements of time-dependent asymmetries and decay rates require excellent particle identification which is achieved with the two RICH detectors in conjunction with the tracking system.

In this thesis, a tuning of the Pythia multiple interaction parameter, $p_{\perp_{\mathrm{Min}}}$, to central multiplicity data measured at CDF and DØ is presented. An extrapolation to LHC energies gives $p_{\perp_{\mathrm{Min}}}^{\mathrm{LHC}} = 3.36 \pm 0.16$.

The optical properties of the prototype beryllium spherical mirror for RICH 1 are measured. The mirror has a radius of curvature of 2675 ± 1 mm and a spot diameter of 3.33 ± 0.02 mm. Limitations of the measurement are discussed and factors affecting the quality of the optical surface are identified.

A measurement of the $\mathcal{CP}$-violating parameter, a_{fs}, from the time-dependent charge asymmetry in flavour specific decays is introduced. The measurement allows the simultaneous determination of two of the three asymmetries, a_{fs}, the B_s^0 production asymmetry and the detection asymmetry assuming one is measured externally.

Two channels are considered, $B_s^0 \to D_s \mu \nu_\mu$ and $B_s \to D_s \pi$. The sensitivity to the flavour-specific asymmetries is explored with a fast Monte Carlo. For $2\,\mathrm{fb}^{-1}$ of LHCb data, the statistical precision on a_{fs} is found to be $\sim 2 \cdot 10^{-3}$ in the semileptonic channel. This represents a factor of ten improvement on the current direct measurement.

Acknowledgements

Amongst the many people who have helped me through this PhD, I'd like to single out those who I'm particularly indebted to:

Prof. Nick Brook for his professional supervision and the opportunity to work in the High Energy Physics Group. For his excellent guidance, adroit reasoning and candid advice. Thanks!

Both Dr. Noel Cottingham and Dr. Jonas Rademacker deserve great thanks for their help and guidance during recent years. I am especially grateful for the illuminating discussions we've shared and their insightful and constructive comments during the writing of this thesis.

I would like to thank the LHCb RICH Group, in particular Dr. Fabio Metlica, Dr. Carmelo D'Ambrosio, Dr. Olav Ullaland and Didier Piedigrossi who were instrumental in my work on the prototype beryllium mirror.

Richard Croft, Jeremy Dickens, Nick Grant, Mark Grimes, Kenneth Lessnoff, Dr. Clare Lynch, Dr. Alex Muir, Dr. Stuart Paterson and Dr. Dan Walker, with whom it was a pleasure to work and share an office with.

I would like to thank all members of the LHCb Collaboration and the Bristol High Energy Physics Group for providing a friendly, stimulating and productive environment.

I owe special thanks to my flatmates, Dr. Robert Frazier and Dr. Simon Metson, whose understanding and willingness to discuss anything but my thesis has preserved my sanity.

And of course my family, who have been nothing but supportive.

Paul Szczypka, April 30, 2008

AUTHOR'S DECLARATION

I declare that the work in this dissertation was carried out in accordance with the Regulations of the University of Bristol. The work is original except where indicated by special reference in the text and no part of the dissertation has been submitted for any other degree. Any views expressed in the dissertation are those of the author and in no way represent those of the University of Bristol. The dissertation has not been presented to any other University for examination either in the United Kingdom or overseas.

SIGNED: . . . . DATE: . . . .

Contents

List of Figures

List of Tables

Chapter 1

Introduction

The LHCb experiment is dedicated to the study of $\mathcal{CP}$ violation and other rare phenomena in the B-sector. In this thesis a new tuning for the Pythia Monte Carlo generator is presented, the prototype Beryllium Mirror for RICH 1 is characterised and the sensitivity to flavour-specific asymmetries at LHCb is assessed.

Chapter 2 gives an overview of the experiments which will benefit from the 14 TeV collisions produced by the LHC accelerator. The LHCb detector is presented and the individual LHCb subdetectors described.

Chapter 3 gives a summary of $\mathcal{CP}$ violation in the Standard Model. The mixing formalism of neutral mesons is introduced and the time-dependent decay rates of flavour-tagged B mesons to $\mathcal{CP}$-eigenstates are given. The Cabibbo-Kobayashi-Maskawa (CKM) triangle is presented and the current status of global CKM fits reviewed.

Chapter 4 describes the tuning of the Pythia Monte Carlo generator to minimum bias data after orbitally excited meson states were introduced to the generator. The excited mesons states decay strongly via pion emission and allow the initial flavour of the B meson to be identified in a process called same-side tagging (SST). The tuned Pythia parameter set used by the LHCb collaboration in Data Challenge 2004 is presented.

The prototype spherical beryllium mirror for RICH 1 is characterised in chapter 5. Factors affecting the quality of the optical surface are identified. Measurements of the mirror's radius of curvature and spot-size using optical methods are presented. Limitations of the measurement are discussed.

In chapter 6 the results of a study of the sensitivity to flavour specific asymmetries at LHCb are presented. A measurement of the $\mathcal{CP}$-violating asymmetry, a_{fs}, from the time-dependent charge asymmetry in flavour-specific decays is introduced. In the Standard Model a_{fs} is small $\sim \mathcal{O}(10^{-5})$, New Physics effects are expected to increase the size of a_{fs} a hundredfold. The current measurements of a_{fs} by the DØ and CDF collaborations are reviewed. The statistical uncertainties for a simultaneous measurement of a_{fs} and the $\mathrm{B_s^0}$ production asymmetry using a fast Monte Carlo, specifically developed for this study, are determined. A simultaneous measurement of the $\mathrm{B_s^0}$ production asymmetry and the detection asymmetry is briefly discussed.

Conclusions are drawn in chapter 7.

Chapter 2

The LHCb Experiment

2.1 The LHC

The Large Hadron Collider (LHC) is a proton-proton collider located at CERN near Geneva. The LHC will collide protons with a centre of mass energy of 14 TeV at a luminosity of $10^{34}\,\mathrm{cm}^{-2}\,\mathrm{s}^{-1}$ [6] during the initial stages of data taking. The LHC accelerator is housed in the 27 km tunnel originally used to house the Large Electron-Positron (LEP) accelerator.

2.1.1 LHC Detectors

A total of six experimental detectors are situated about the LHC ring. Two of the detectors, ATLAS (A Toroidal LHC ApparatuS) and CMS (Compact Muon Solenoid), are large general purpose detectors designed to directly identify new particles and physics processes. The other four detectors are smaller and more specialised.

ALICE (A Large Ion Collider Experiment) is a general purpose heavy ion detector [7] and aims to establish the existence of and analyse QCD bulk matter and the quark-gluon plasma (QGP). The ALICE detector will obtain data from a number of different nucleus-nucleus collision types including *Pb-Pb*, *Pb-p* and *pp*.

The TOTEM[1] experiment aims to measure the total cross-section, elastic scattering

---

[1] TOTal Elastic and diffractive cross section Measurement.

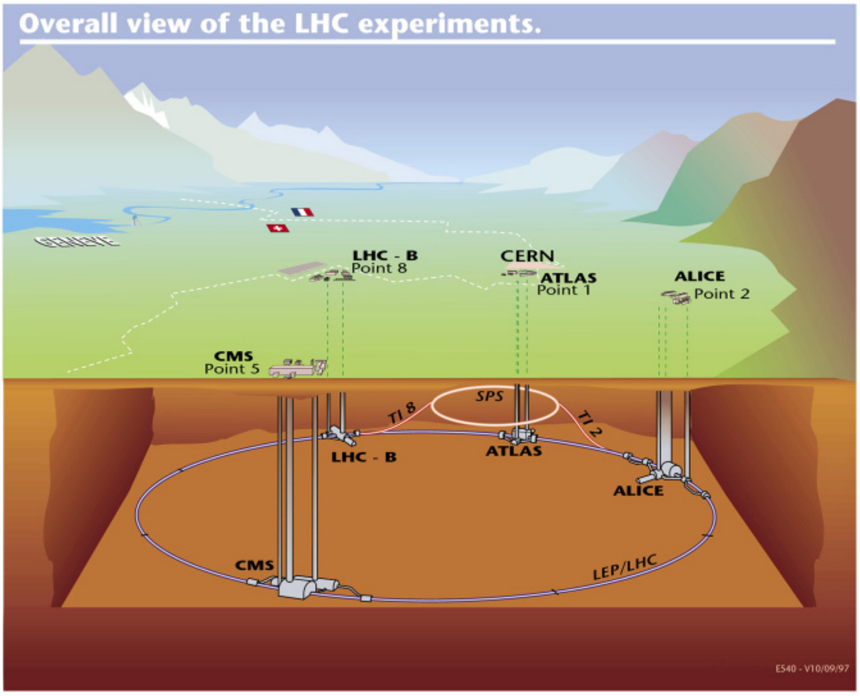

Figure 2.1: Overview of the locations of the four main LHC experimental detectors. The LHCb detector is located at point 8. (Not to scale.)

and diffractive dissociation at the LHC [8]. The TOTEM detector system is composed of roman pot detectors and forward inelastic detectors positioned symmetrically about interaction point 5 (IP5) which it shares with the CMS detector.

The Large Hadron Collider forward (LHCf) is primarily concerned with refining the Monte Carlo simulation of high energy cosmic ray (HECR) air showers [9]. The LHCf detector systems are placed $\sim\pm140\,\text{m}$ about the ATLAS interaction point (IP1). The detectors make use of sampling calorimeters to measure the energy spectrum of neutral particles produced in the extreme forward region.

A diagram of the LHC including the location of the four main experiments is shown in figure 2.1.

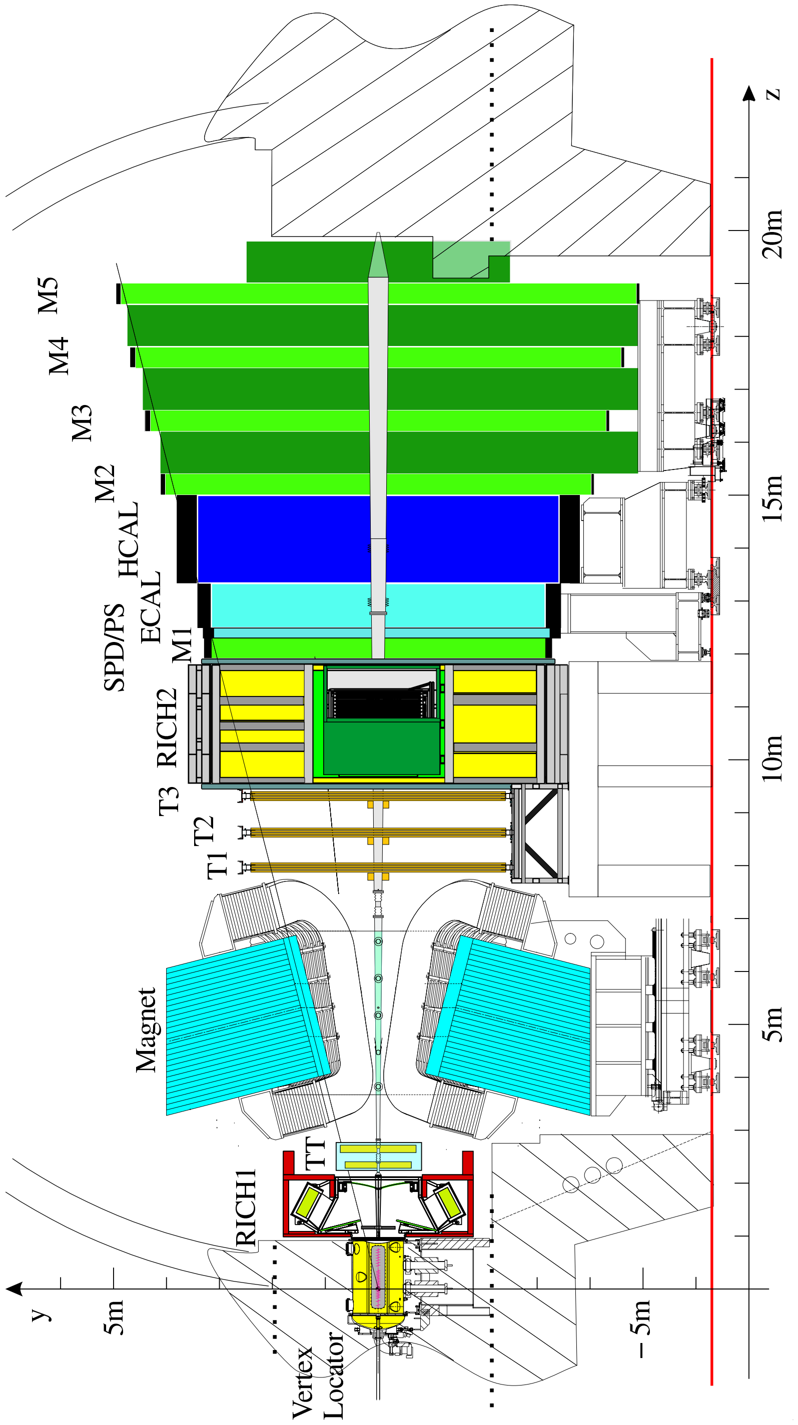

Figure 2.2: View of the Large Hadron Collider beauty (LHCb) detector in the non-bending plane. From the Interaction Point (IP) particles pass through the VErtex LOcator (VELO), the first Ring-Imaging CHerenkov Detector (RICH 1), the Trigger Tracker (TT), the Magnet, three Tracking Stations (T1 - T3), RICH 2, the Silicon Pad Detector and PreShower (SPD/PS), the first Muon Station (M1), the Electron and Hadron CALorimeters (ECAL, HCAL) and the remaining Muon Stations (M2 - M5).

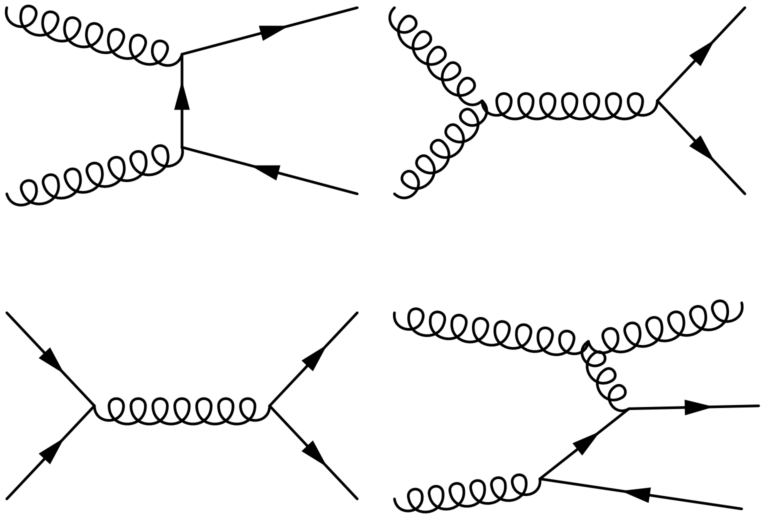

Figure 2.3: Production mechanisms of $b\bar{b}$ pairs at LHCb. Clockwise from bottom left: $q\bar{q}$ annihilation, gluon fusion, gluon fusion and flavour excitation.

2.2 The LHCb Experiment

The Large Hadron Collider beauty [10] (LHCb) experiment (Fig. 2.2) is a forward one-arm spectrometer dedicated to the study of $\mathcal{CP}$ violation and other rare phenomena in the decay of hadrons containing b-quarks at the LHC. The physics goals are to check the consistency of the Standard Model (SM) through precision measurements of the sides and angles of the Cabibbo-Kobayashi-Maskawa (CKM) triangle, and to search for new physics in decays that are rare, or forbidden, in the Standard Model.

Typical diagrams for $b\bar{b}$ production are shown in 2.3. The two incoming partons generally have dissimilar momenta which boosts the outgoing $b\bar{b}$ system. This has the result that in the majority of events, both B-hadrons originating from the same $b\bar{b}$ pair are located in the same forward region. LHCb's single arm design takes advantage of this fact. The polar angle distribution of B-hadrons formed from $b\bar{b}$ pairs in pp collisions at 14 TeV is shown in figure 2.4. Approximately one third of B-hadrons lie within the LHCb acceptance.

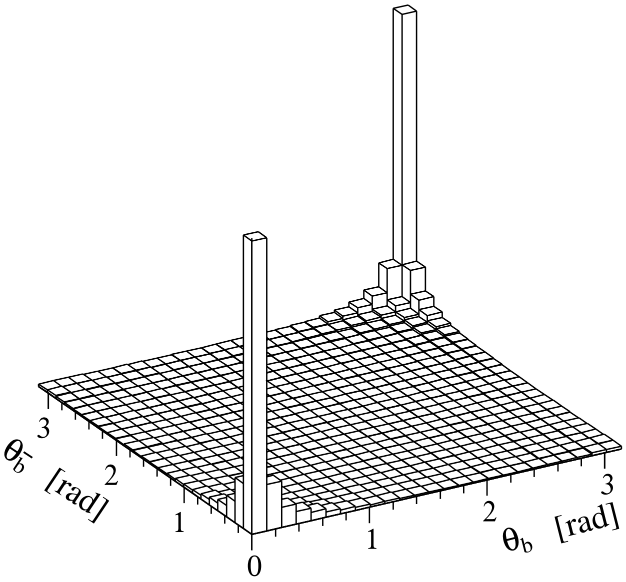

Figure 2.4: Polar angles of the B- and $\overline{\text{B}}$-hadrons generated by Pythia[1].

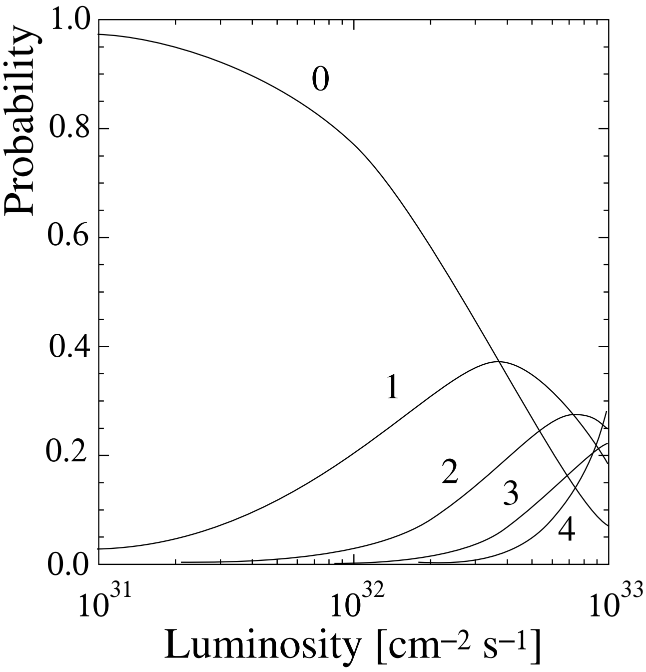

Figure 2.5: Probabilities for having 0,1,2,3 and 4 pp interactions per bunch crossing as a function of the machine luminosity at LHCb.

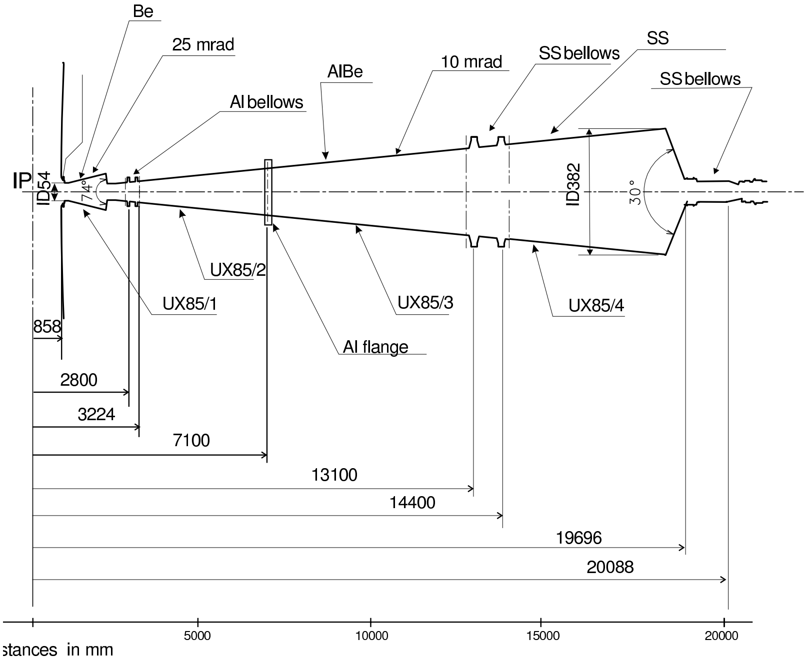

Figure 2.6: The layout of the LHCb beampipe, all dimensions are in mm. The position of each section, UX85/1 to UX85/4, is indicated.

At the LHC design luminosity of $10^{34}\,\mathrm{cm}^{-2}\mathrm{s}^{-1}$, most events would involve multiple *pp* interactions. Multiple *pp* interactions severely complicate both B-tagging and lifetime measurements due to the increased combinatorics. Figure 2.5 shows the probability of a given number of interactions per bunch crossing as a function of luminosity in *pp* events. The proton beams are defocused before they reach interaction point 8 which lowers the luminosity to $\sim 2 \cdot 10^{32}\,\mathrm{cm}^{-2}\mathrm{s}^{-1}$. At this luminosity the majority of bunch crossings only produce a single *pp* interaction. Events which are too complicated are discarded at the trigger level by the Level-0 Trigger.

2.3 The LHCb Beampipe

The LHCb beampipe (UX85) is designed to minimise the amount of material present in the detector acceptance and to preserve the LHC vacuum. The beampipe consists of a thin exit window sealed to the VErtex LOcator (VELO) vacuum tank followed by two conical parts with apertures of 25 mrad and 10 mrad respectively. Sections of the beampipe are numbered with increasing distance from the Interaction Point (IP).

The first section (UX85/1) is constructed from 1 mm thick beryllium and consists of a 25 mrad followed by a 10 mrad cone and is welded to the VELO exit window. Aluminium bellows connecting UX85/1 and UX85/2 absorb the thermal expansion of the vacuum chambers during bakeout Sections UX85/2 and UX85/3 are long conical sections constructed from an Al-Be alloy and have an aperture of 10 mrad. The lengths of sections UX85/3 and UX85/4 are optimised to reduce the number of low energy secondary particles produced in the connecting flange. Section UX84/4 is constructed of stainless steel approximately 3 mm thick.

Figure 2.6 shows the layout of the various sections of the beampipe in relation to the nominal interaction point.

2.4 VELO

The VELO provides precise measurements of track coordinates close to the interaction region [11]. The track coordinates are used to:

- Reconstruct the position of the Primary Vertex (PV).
- Identify tracks not originating from the PV.
- Reconstruct the position of B and C-hadron vertices.

The VELO surrounds the IP (Fig. 2.2) and is the main tracking device before the magnet. A schematic diagram of the VELO is shown in figure 2.7.

2.4.1 Silicon Sensors

Tracks are identified using 220 μm thick silicon strip sensors (Fig. 2.8). Each sensor contains 2048 strips and measures either the radial or azimuthal position of a track. Radial sensors are arranged into four sectors of 512 strips each. The strip pitch, p, of

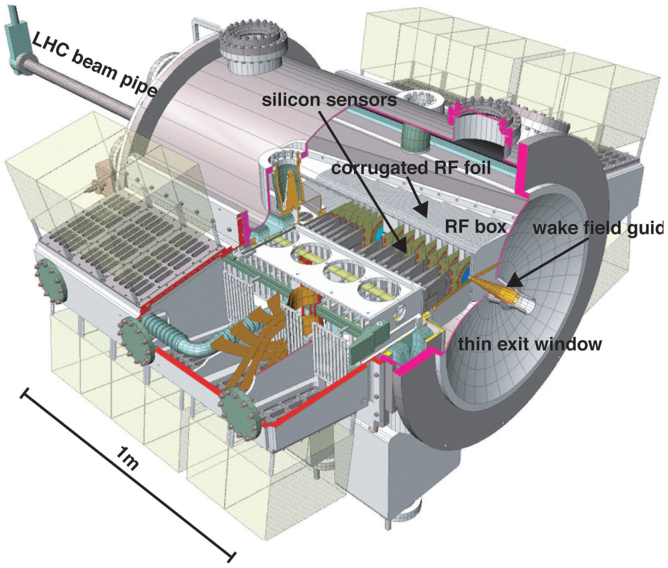

Figure 2.7: Cutaway diagram of the VELO showing the location of the silicon sensors.

radial sensors varies according to the following function:

$$p = 40 + (101.6 - 40) \times \frac{r - 8190}{41949 - 8190}, \tag{2.1}$$

where r is the radial position of the strip in μm. The ϕ-measuring sensors have their strips arranged quasi-radially in two regions. The inner region consists of 683 strips arranged at a 20^o stereo angle and the outer region consists of 1365 strips at a -10^o stereo angle. The sensitive area of each sensor starts at a radius of 8.17 mm and extends to a radius of 42 mm. Each sensor spans 182^o, the overlap is used to align the two halves relative to each other.

2.4.2 VELO Module

A VELO module consists of two strip sensors, one ϕ-measuring and one r-measuring, the front-end electronics, a carbon-fibre mechanical support and a cooling block. A schematic of an LHCb module is shown in figure 2.9. The key module components are:

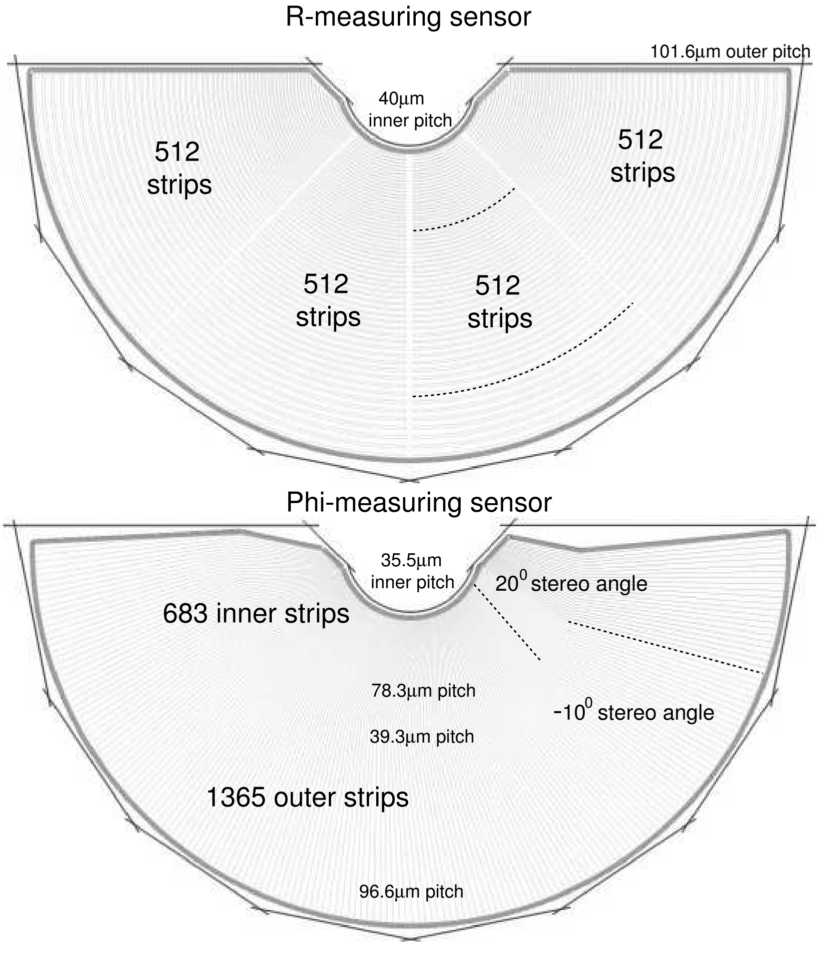

Figure 2.8: Strip layout of the radial (top) and ϕ-measuring (bottom) sensors. Selected strips are highlighted for clarification.

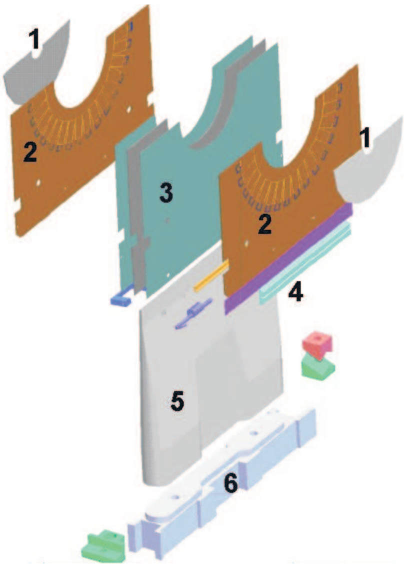

Figure 2.9: Exploded diagram of a VELO module: 1) Silicon sensors. 2) Front-end electronics. 3) Support substrate. 4) Cooling block. 5) Low-mass carbon-fibre paddle. 6) Paddle base.

1. The silicon sensors.
2. The front-end electronics mounted on a thin Kapton[2] sheet.
3. The substrate which provides mechanical support and a thermal pathway; it is constructed from a complex carbon-fibre thermo-pyrolytic graphite composite.
4. The cooling block which provides the thermal linkage to the cooling system.
5. The low mass carbon-fibre paddle.
6. The paddle base made of carbon-fibre.

The modules are positioned on a movable platform which supports the two halves of the VELO telescope with an accuracy of approximately 10 μm at 21^o C.

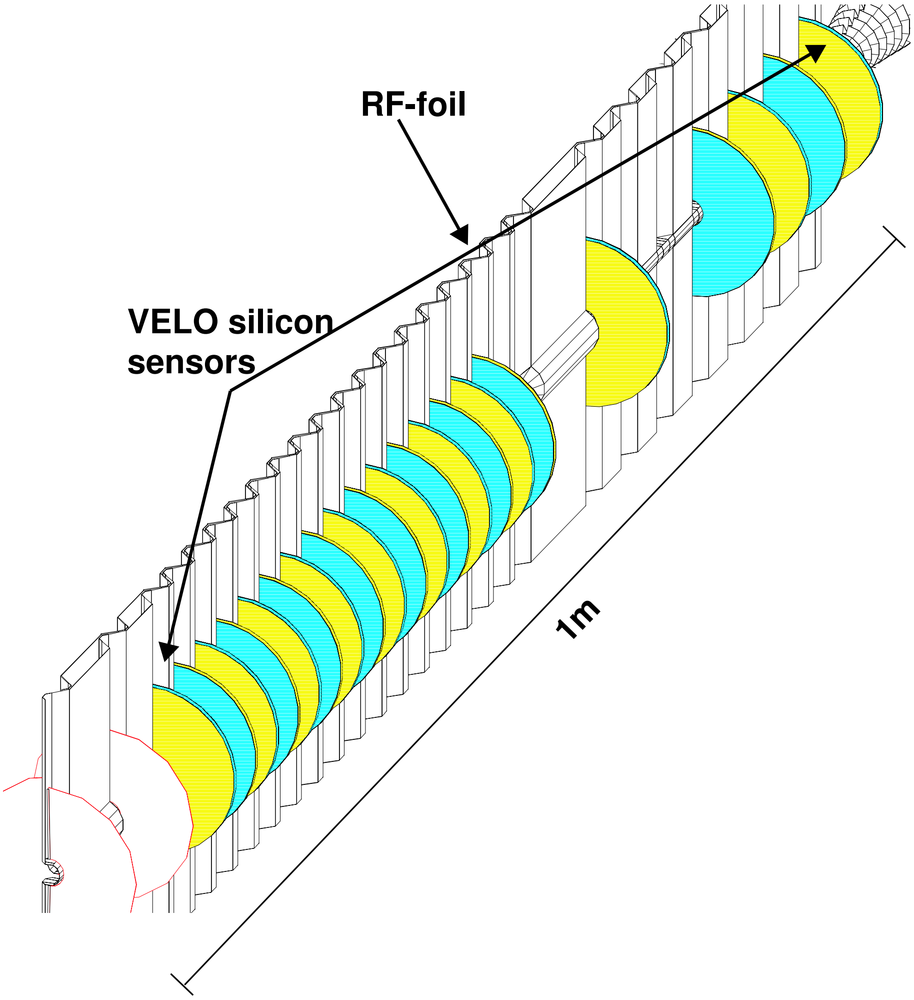

Figure 2.10: Arrangement of VELO stations along the beam axis. The first two stations (unshaded) belong to the pile-up system and contain only r-measuring sensors. Stations are positioned most densely about the interaction point. The RF-foil has the dual purpose of protecting the electronics from RF fields and preserving the LHC vacuum. Modules contain one ϕ (yellow) and one r-measuring (blue) sensor.

2.4.3 Module Arrangement

The VELO modules are arranged in 21 stations along the beam axis. Figure 2.10 shows the arrangement of the stations with respect to the beamline. The station arrangement minimises the amount of material in the LHCb acceptance whilst providing excellent impact parameter resolution. A degree of overlap is provided by displacing adjacent modules by approximately 1.5 cm. This overlap allows the two detector halves to be aligned online after injection. The modules are mounted on a platform which allows both halves of the sensor array to be retracted by 3 cm. This moves the sensors outside of the aperture required by the LHC machine during injection.

2.4.4 The VELO Vacuum Vessels

The silicon detectors operate in a secondary vacuum separated from the LHC vacuum by a detector vacuum box. In addition to maintaining the LHC vacuum, the box reduces the effect of wake-fields produced by beam bunches passing through the detector. The sides of the box which fall within the LHCb acceptance are constructed from 0.5 mm thick Aluminium. The top foil of the box is corrugated and constructed from an aluminium alloy with 3% magnesium. Due to the deformations, the thickness of the foil varies between 0.30 mm and 0.15 mm and has an average thickness of approximately 0.25 mm. A diagram of the top foil is given in figure 2.11.

2.4.5 Primary Vertex Resolution

The position of the primary vertex in $b\bar{b}$ events in which a B-hadron is produced within 400 mrad of the beam axis is expected to be determined with a longitudinal (z) resolution of 44 μm and a transverse (x, y) resolution of 7.8 μm [10].

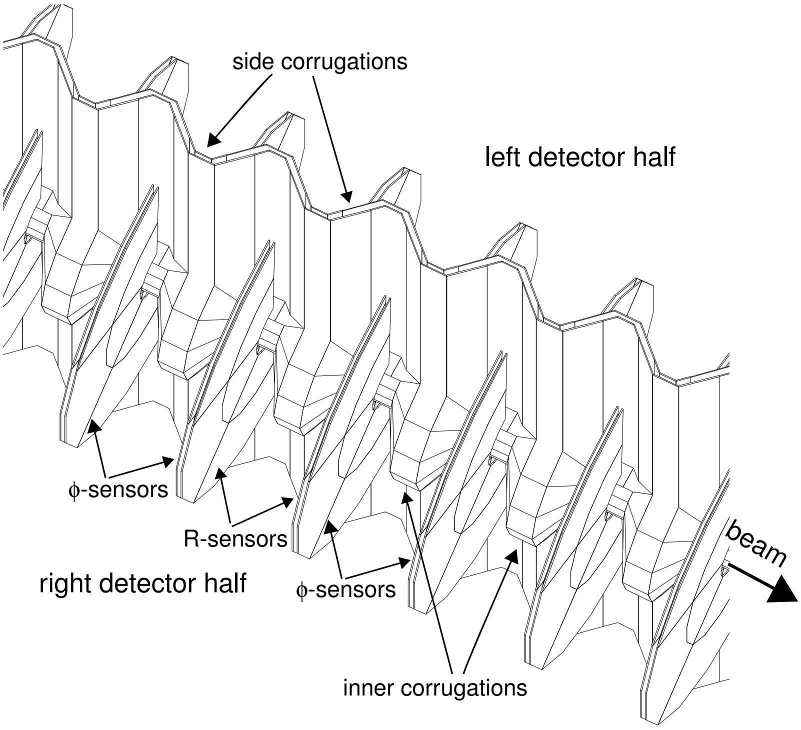

Figure 2.11: Close up of the secondary vacuum vessel showing the corrugated top foil. The distance between modules is 1.5 cm.

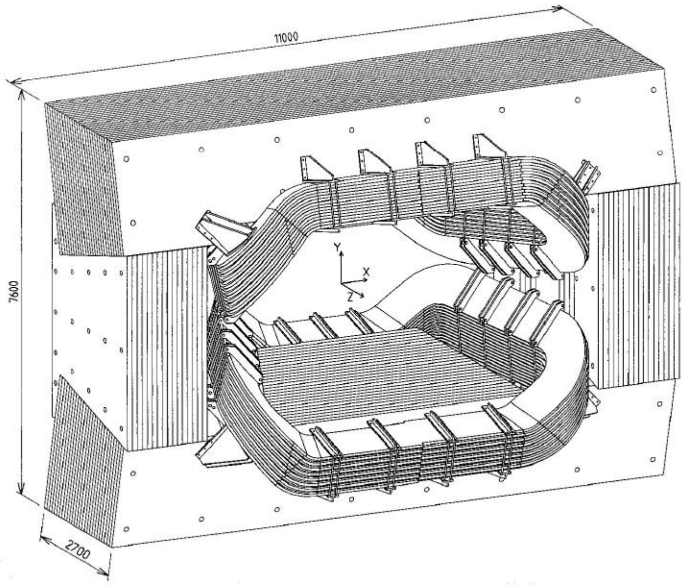

Figure 2.12: The LHCb dipole magnet and yoke.

2.5 LHCb magnet

The LHCb detector uses a non-superconducting dipole magnet [12] to measure the momentum of charged particles. The magnet consists of two trapezoidal coils bent at 45^o on the two transverse sides, arranged inside an iron yoke of window-frame configuration. The magnet gap is wedge-shaped in both the horizontal and vertical directions in order to follow the detector acceptance. Each magnet coil is constructed from 15 mono-layer pancakes with each pancake containing 15 turns of conductor. Regular field inversions may be carried out due to the short ramping-up time of the magnet.

The iron yoke guides and shapes the magnetic flux generated by the coils. It consists of two identical horizontal pieces and two identical vertical pieces. The horizontal pieces are orientated orthogonally to the plane of the coils. A vertical magnetic field is produced in the gap between the pole faces. The magnet provides an integrated field of 4 Tm for tracks originating near the primary interaction point.

---

[2] Kapton is a polyimide insulator which has a low outgassing rate and is resistant to radiation damage.

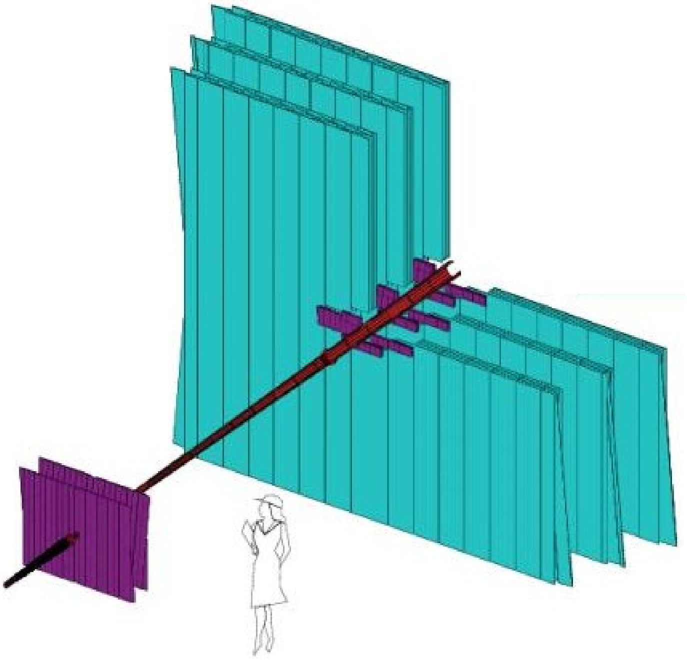

Figure 2.13: A view of the tracking detectors of LHCb in relation to the beampipe. The Trigger Tracker is shown at the bottom-left of the figure. The three tracking stations, divided into Inner (purple) and Outer Trackers (blue) are to the right of the figure.

2.6 Tracking System

The LHCb Tracking System consists of three main components, the VELO, the Trigger Tracker (TT) and the Tracking Stations. The Tracking Stations consist of an Inner Tracker (IT) and Outer Tracker (OT) detector and are optimised for momentum measurement. The VELO (Section 2.4) surrounds the interaction point and is optimised for vertexing. The Trigger Tracker is located downstream of RICH 1 and in front of the entrance to the LHCb magnet (Fig. 2.2 centre). There are three Tracking Stations in total, all of which are located between RICH 2 and the magnet. The tracking detectors are shown in figure 2.13.

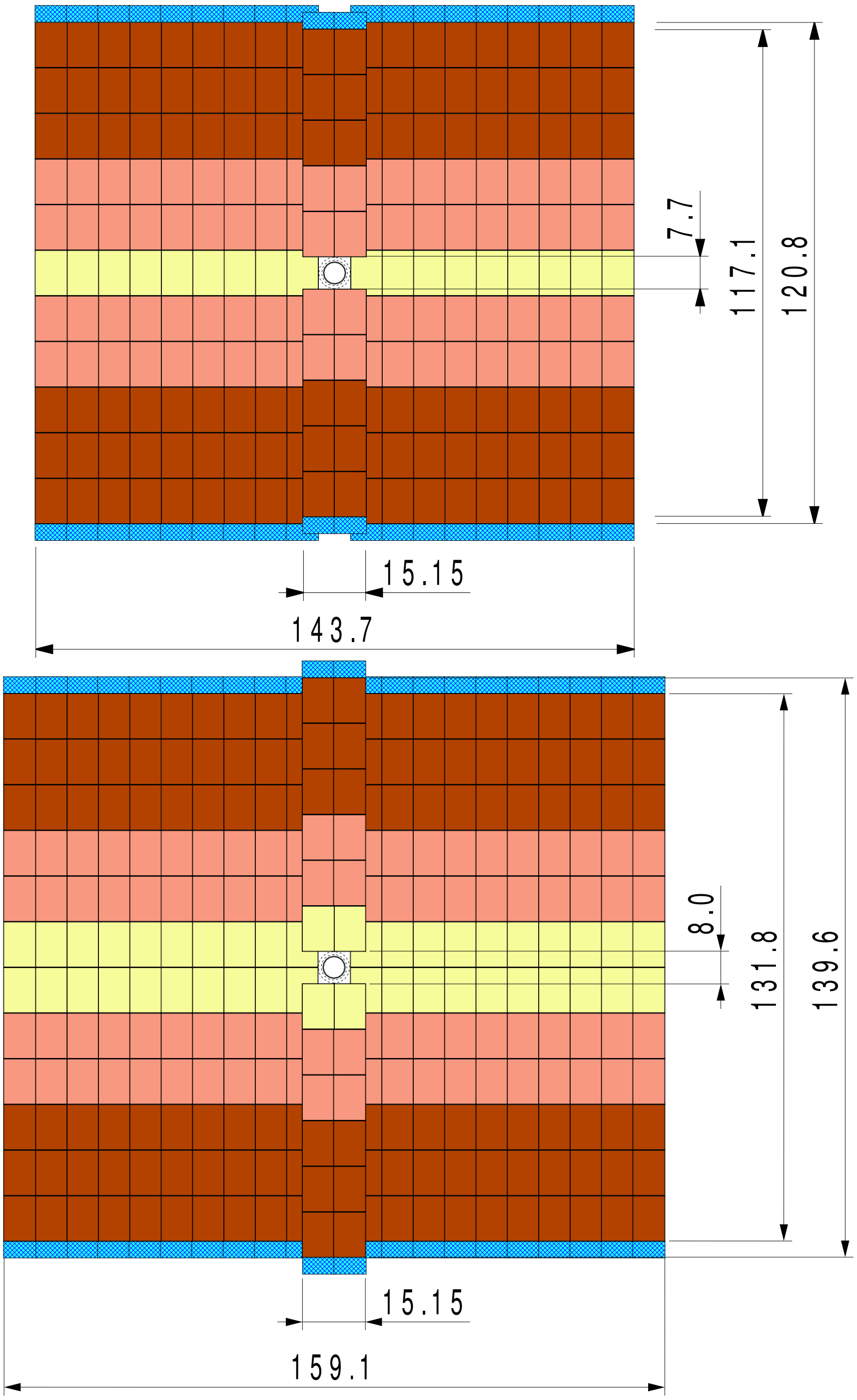

Figure 2.14: TTa x-layer (above) and TTb x-layer (below). The shading indicates the grouping of ladder readout sections. All dimensions are in cm.

2.6.1 The Trigger Tracker

The Trigger Tracker is located between RICH 1 and the Magnet (Fig. 2.2) and consists of four detection layers. The first and last layers (x-layers) have vertically arranged readout strips. The second and third layers (u/v-layers) have readout strips rotated by a stereo angle of $\pm 5^o$ respectively. The four layers are arranged into pairs and have a gap of approximately 30 cm between the pairs [10]. The first pair (TTa) is centred around z = 232 cm and the second pair (TTb) is centred around z = 262 cm. Both TTa and TTb cover the nominal LHCb acceptance and therefore are of slightly different dimensions. TTa measures 143.5 cm horizontally and 118.5 cm vertically whereas TTb has a width of 162.1 cm and a height of 133.8 cm.

The active area of the TT is covered entirely by silicon microstrip detectors with a strip pitch of 198 μm. Both TTa and TTb have a square shaped hole which accommodates the beampipe. The width of the hole at TTa is 7.7 cm and 8.0 cm at TTb.

The TT uses 11 cm long and 7.8 cm wide silicon strip sensors. The sensor layout of the two x-layers is shown in figure 2.14. In TTa nine ladders are arranged either side of the beampipe. Each ladder consists of eleven sensors. In addition to these, there are two five-sensor ladders which cover the area immediately above and below the beampipe. In TTb there are ten twelve-sensor ladders arranged horizontally and two six-sensor ladders covering the area above the beampipe. The inner layers have a sensor arrangement similar to their partner x-layers but with the ladders rotated by $\pm 5^o$. The front-end readout electronics for each sector are located out of the detector acceptance at either end of the ladders.

2.6.2 Tracking Stations

LHCb has three tracking stations located between the magnet and RICH 2 (Fig. 2.2). In order to limit the occupancy of the tracking sensors, each tracking station is divided into an Inner Tracker and an Outer Tracker. The Inner Tracker is composed of silicon microstrip sensors and the Outer Tracker from straw tubes. There is approximately 1 cm of overlap between the sensitive areas of the Inner and Outer Tracker at each station.

2.6.2.1 Inner Tracker

In each of the tracking stations the Inner Tracker covers a central area surrounding the beampipe. The Inner Tracker uses 320 μm thick single-sided sensors with a strip pitch of 198 μm [13]. The silicon sensors used are 11 cm long and 7.8 cm wide and are assembled on ladders containing either one (11 cm) or two (22 cm) sensors. The layers of each station follow the layout of the Trigger Tracker, namely two vertical layers surrounding two layers rotated by $\pm 5^o$.

Each station consists of four independent detector boxes composed of either one- or two-sensor long ladders. Adjacent ladders overlap by approximately 1 mm which provides full acceptance coverage.

2.6.2.2 Outer Tracker

The Outer Tracker [14] uses straw tube technology [15]. The straw tubes have an inner-diameter of 5 mm and use an Argon/CO_2 mixture as drift gas [16]. The anode wire has a diameter of 25 μm and is composed of gold-plated tungsten. Each straw tube has an inner radius of 2.45 mm and is filled with Ar(70%)-CO_2(30%) drift gas. The inner layer of the straw tubes is constructed from Kapton XC[3] and forms the cathode. The outer layer is made from a Kapton XC-aluminium laminate [17] that provides shielding and limits crosstalk from neighbouring channels. A second, staggered layer is introduced to cover the insensitive area between tubes.

Each station is made from four aluminium C-frames which hold two layers of modules each. Every module is mechanically stable, gas-tight and contains parallel straw tubes arranged in two staggered monolayers. A typical module cross section is shown in figure 2.15. The modules are arranged vertically and pseudo-vertically which allows precise determination of the hit position in the bending plane (x-plane). The straw tubes in the pseudo-vertical modules are positioned at a stereo angle of $\pm 5^o$ in the u/v-layers and allows the vertical hit position to be determined. Modules in the same detection layer do not overlap and have an inactive area equivalent to one tube width. A hit resolution

---

[3] Kapton XC is a trade-name of carbon-doped Kapton.

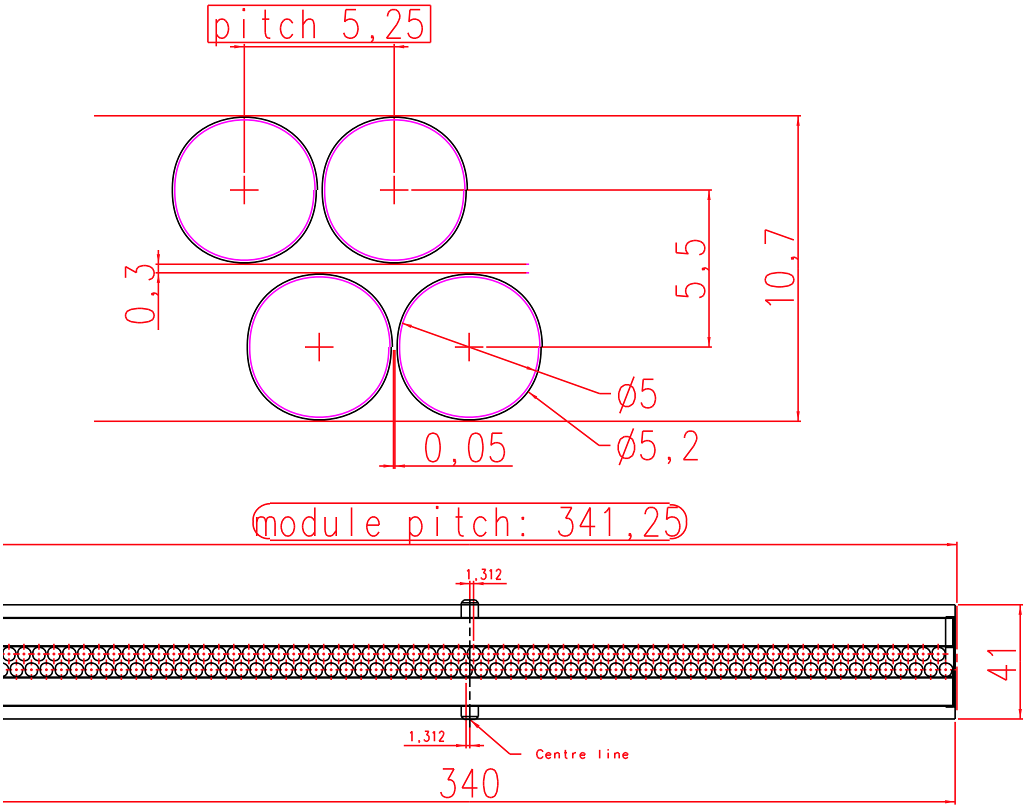

Figure 2.15: Top view of a module layer including the straw tube cross section. All dimensions are in mm.

of 200 μm is obtained using an anode voltage of 1600 V and the ASDBLR[4] preamplifier.

Modules span the full height of the LHCb acceptance except for areas above and below the IT. Those modules which span the full height of the acceptance are electrically split in the middle in order to reduce cell occupancy and signal propagation times. The wire ends in the central region are soldered to PCB[5] strips which span the width of a module. The PCB strips are 0.8 mm thick and 20 mm in the direction of the wires. The tubes are joined by a glass fibre epoxy cover which maintains proper flow of the drift gas through the tubes. Modules above and below the IT have a single anode wire and are

---

[4] Amplifier, Shaper, Discriminator, Base-Line Restorer.

[5] Printed Circuit Board

electrically identical to one half of a full-span module.

All readout electronics are located at the top and bottom of the upper and lower modules respectively. The OT has a readout window of 75 ns. Since the nominal time between bunch crossings is 25 ns, a window can contain responses from both the previous and subsequent bunch crossing. The spurious hits from the neighbouring events are handled in the pattern recognition algorithms.

2.6.3 Tracking and Physics Performance

The invariant mass resolution of reconstructed particles depends on the momentum measurements of individual tracks and the angular resolution of tracks at the decay vertex. The momentum is mainly determined by the tracking system. Simulation studies [15] show that the expected mass resolutions of the channels $\mathrm{B_s^0} \rightarrow \mathrm{D_sK}$ and $\mathrm{B_d^0} \rightarrow \pi^+\pi^-$, both of which are important for combinatoric background suppression, are $22\,\mathrm{MeV}/c^2$ and $11\,\mathrm{MeV}/c^2$ respectively.

The main tracking components achieve an average tracking efficiency of $> 90\%$ for indivdiual tracks originating from B-decays [15].

2.7 LHCb RICH detectors

The passage of charged particles through the radiator material of a Ring-Imaging CHerenkov (RICH) detector leads to the formation of rings of Cherenkov light [18]. The signal from an event in a RICH detector is thus a set of ring images, which may overlap in regions of high track density. Rings are identified in the pattern of detected photons and the Cherenkov emission angle, θ_c, of the associated photons is calculated [19]. The velocity, v, of the particle can then be calculated using the following relation:

$$\cos\theta_c = \frac{c}{nv}, \tag{2.2}$$

where n is the refractive index of the radiator. With a knowledge of the track momentum the particle mass can then be calculated.

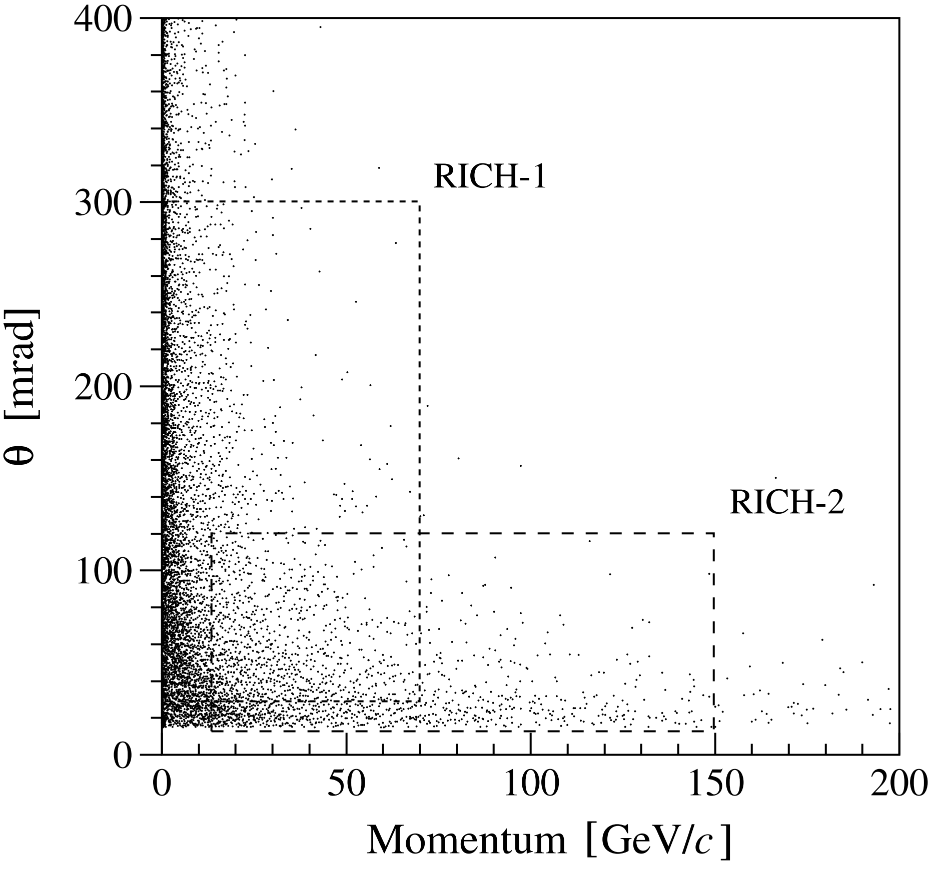

Figure 2.16: Track angle vs. momentum for all tracks from $B_0 \rightarrow \pi\pi$ events.

2.7.1 The LHCb RICHes

The LHCb detector includes two RICH detectors [20]. RICH 1 is located upstream of the Magnet (Fig. 2.2) and RICH 2 is located between the Tracking Stations and the Silicon Pad Detector and PreShower (SPD/PS). Both LHCb RICH detectors follow the same basic design. Cherenkov radiation is emitted by charged particles passing through the radiating material in the detector. The radiation is focused onto the photon detector plane by a set of spherical mirrors which are tilted in order to remove the photon detectors from the LHCb acceptance. In addition to the spherical mirrors, a secondary set of plane mirrors is used to minimise the overall detector length. Both detectors use Hybrid Photon Detectors (HPDs) which are sensitive to single photons in the range

$200\,\text{nm} < \lambda < 600\,\text{nm}$.

There is a strong correlation between the polar angle and momentum of tracks (Fig. 2.16). Low momentum particles are identified in RICH 1 (Fig. 2.17) which has an angular acceptance of $20-300$ mrad in the horizontal plane ($20-250$ mrad in the vertical plane) and uses a combination of silicon aerogel ($n = 1.03$) and C_4F_{10} gas ($n = 1.0014$) radiators. High momentum particles (up to $\sim 100\,\text{GeV}/c$) are detected by RICH 2 which has an acceptance of $15 - 120$ mrad and uses CF_4 gas ($n = 1.0005$) as a radiator.

2.7.2 RICH 1

The RICH 1 [10] detector uses silicon Aerogel ($n = 1.03$) and C_4F_{10} ($n = 1.0014$) as radiators. A 5 cm thick wall of aerogel tiles is located approximately 1 m from the IP. The C_4F_{10} radiator is contained within a gas-tight enclosure. The magnetic shielding draws the field created by the magnet away from the sensitive electronics of the HPDs whilst maintaining an effective magnetic field in the region of the VELO.

A set of four spherical mirrors ($R \approx 2.7\,\text{m}$) is used to focus the Cherenkov radiation onto the HPD planes. Material in the detector acceptance is minimised by using low-mass carbon-fibre mirrors.

A secondary set of “flat” mirrors ($R \approx 100\,\text{m}$) is used to minimise the overall detector length. The flat mirrors are split into two planes of eight mirrors and are mounted within the gas enclosure. A quartz window is used to separate the HPDs from the C_4F_{10} gas volume.

2.7.3 RICH 2

The second RICH detector, RICH 2 is located upstream of the muon stations and the calorimeter system and uses CF_4 gas ($n = 1.0005$) as a radiator. The optical system of RICH 2 is similar to that of RICH 1 in that it consists of a set of spherical mirrors and a set of flat mirrors. The optical system is arranged such that the HPD arrays are positioned either side of the beamline. The spherical mirror system is composed of 56 hexagonal segments arranged in two arrays. The arrays have a common centre of

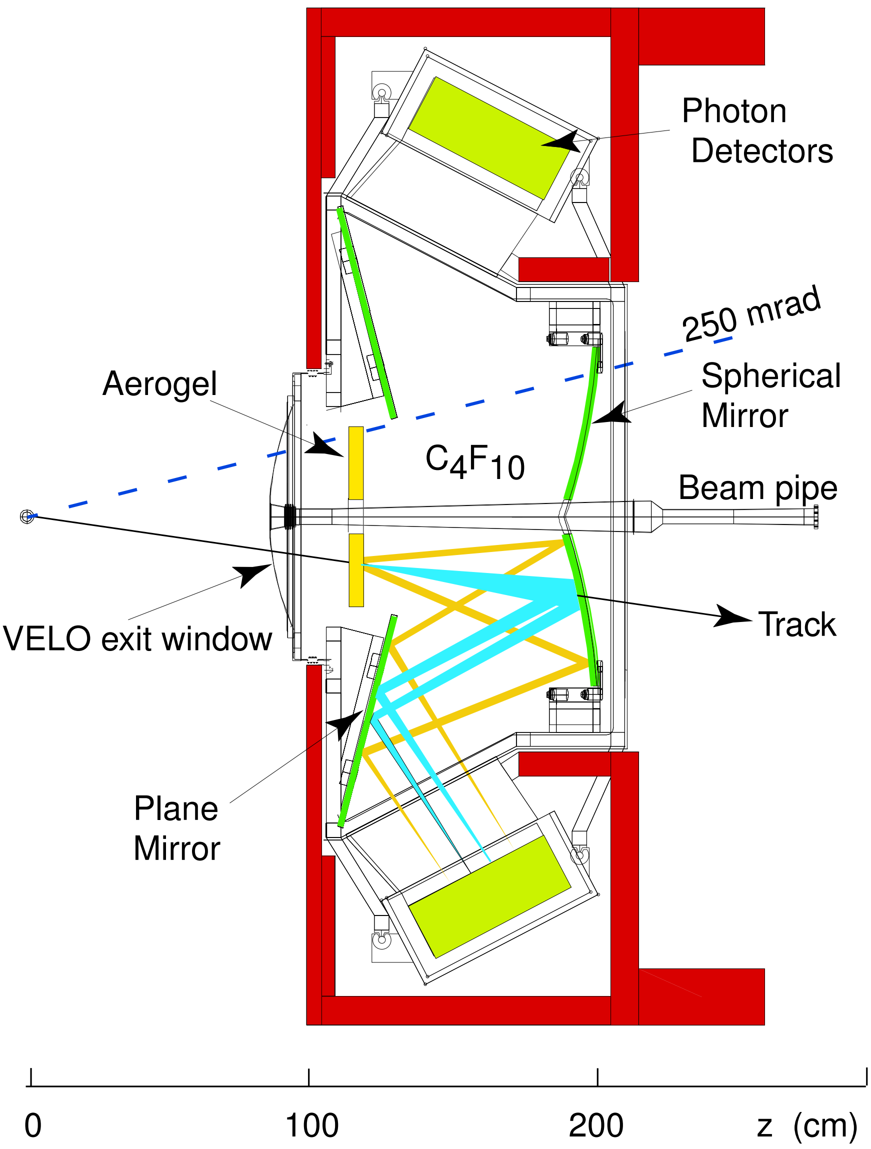

Figure 2.17: RICH 1 schematic. The magnetic shielding (red) protects the HPD arrays from excessive fields whilst maintaining bending power in the region of the VELO. A track originating from the interaction region is indicated.

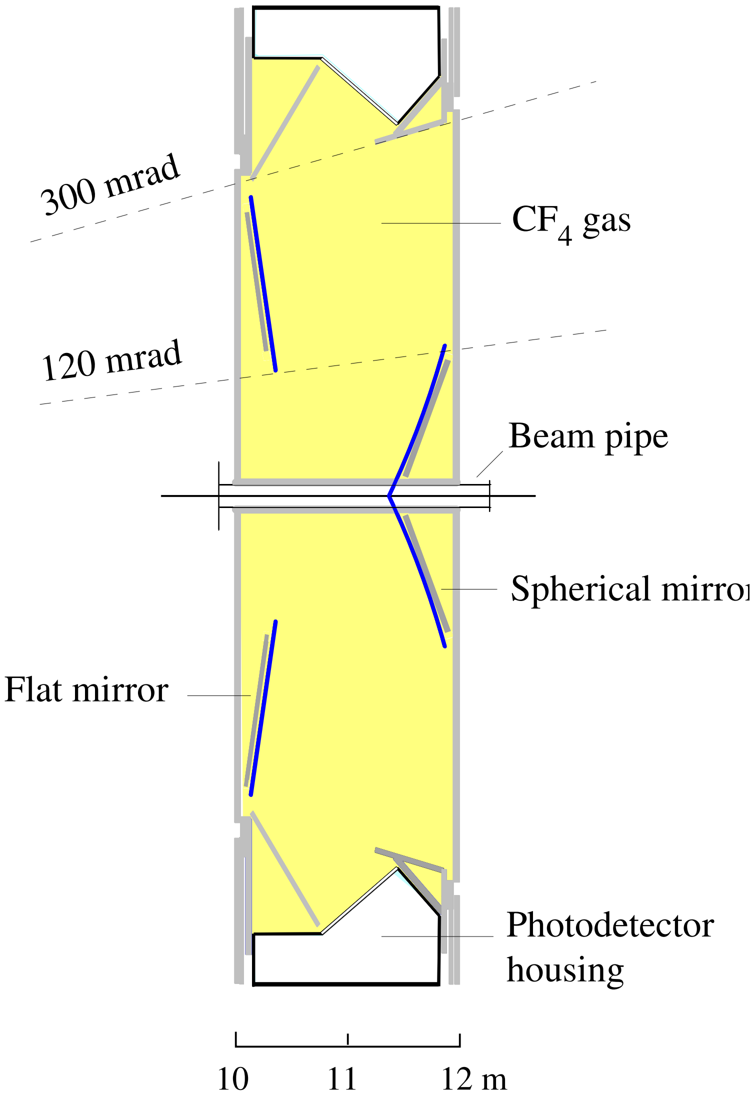

Figure 2.18: A schematic diagram of the RICH 2 subdetector.

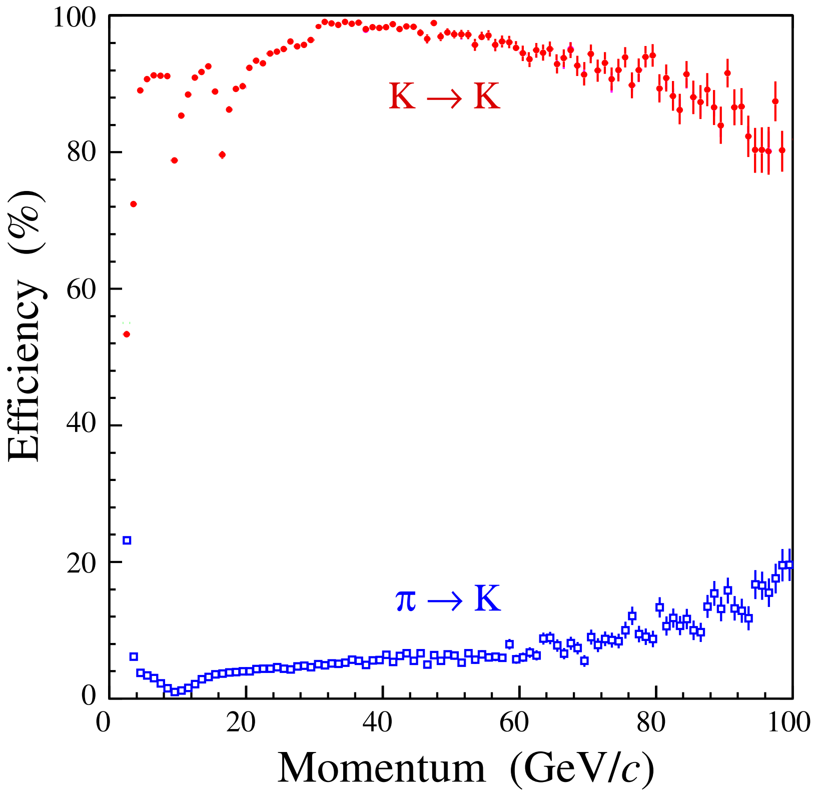

Figure 2.19: Kaon identification efficiency (top) and pion misidentification rate (bottom) using the RICH detectors.

curvature and are tilted horizontally away from the beamline by 450 mrad.

The flat mirror system is composed of forty 437 mm square mirrors. The flat mirror planes are tilted by 140 mrad with respect to the horizontal. A schematic diagram of the RICH 2 detector is shown in figure 2.18.

2.7.4 Particle Identification

Particle identification using the RICH system is performed as follows. For each event, a set of mass hypotheses for each reconstructed track is calculated. Using this data, the probability distribution for finding photons in each pixel of the detector is determined and then compared to the observed hit distribution. A likelihood is determined from

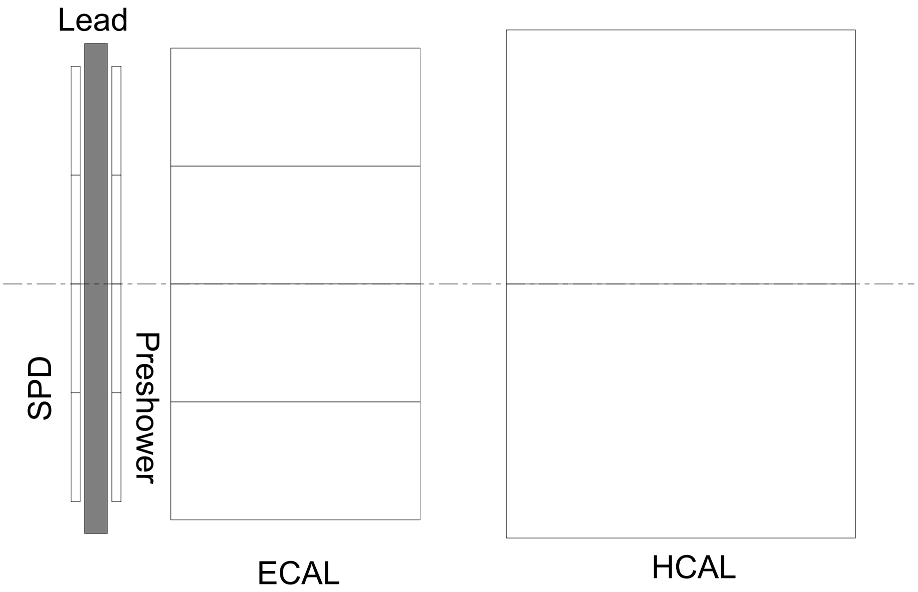

Figure 2.20: A schematic view of the LHCb Calorimeter Systems. The IP is to the left of the figure.

this comparison and then the track mass hypotheses are varied in order to maximise the likelihood. Efficient $\pi - K$ separation is achieved using this method, giving an average Kaon identification efficiency of $\sim$ 88% and an average pion misidentification rate of $\sim$ 3% (Fig. 2.19) [21].

2.8 Calorimeters

The LHCb Calorimeter System provides high E_T candidates at the first trigger level (L0) in addition to particle identification. π^0 reconstruction, essential for the full physics program at LHCb, is also possible using information from the ECAL [22].

The LHCb Calorimeter System (Fig. 2.20) is composed of the Scintillator Pad/PreShower (SPD/PS), the Electromagnetic Calorimeter (ECAL) and the Hadronic Calorimeter (HCAL) [22]. The calorimeter acceptance is 30 mrad to 300 mrad in the horizontal plane and 30 mrad to 250 mrad in the vertical plane and obeys a projective geometry centred on the nominal interaction point. The calorimeter systems are located upstream of the second Muon Station (Fig. 2.2).

The SPD/PS system is made from a 12 mm thick lead converter plate sandwiched between two layers of scintillator pads. The ECAL is based on "shashlik" technology [23] and uses a sampling structure of 2 mm lead sheets interspersed with 4 mm thick scintillator plates. The HCAL uses steel and scintillating tiles as absorber and active material respectively and is segmented into two sections with square readout cells of size 131.3 mm and 262.6 mm. All subsystems transfer scintillation light to phototubes via wavelength-shifting (WLS) fibres. The SPD and PS use a single WLS fibre per pad. Multiple fibres from the SPD and PS are read out using one Multi-Anode Photo-Multiplier Tube (MAPMT). The ECAL and HCAL use fibre bunches which are read out using individual phototubes.

2.8.1 SPD and Preshower

The SPD and PS detectors are two near identical planes of scintillator pads separated by 56 mm and encompass a 12 mm lead converter plane. The dimensions of the SPD plane are approximately 0.45% smaller than those of the PS due to the projectivity requirements. Both detector planes are split into two halves and mounted on horizontal rails. Each half can be independently retracted to allow for maintenance access.

Electron-photon separation at L0 is achieved with the SPD since charged particles will deposit energy in the detector whilst neutral particles will not. The probability of photon misidentification using the SPD is expected to be of the order of 1% at L0 for photon energies in the range 20 to 50 GeV. The SPD also provides a measure of event multiplicity.

Both the SPD and PS use the same 15 mm thick scintillating pads. Scintillation light is collected by 3.5 loops of WLS fibres embedded in the pads. The WLS fibres convert the scintillation light to green light which is then channelled via total internal reflection to a MAPMT. The arrangement of the cells is such that there is a one-to-one correspondence between cells and segments of the ECAL. The SPD/PS therefore has

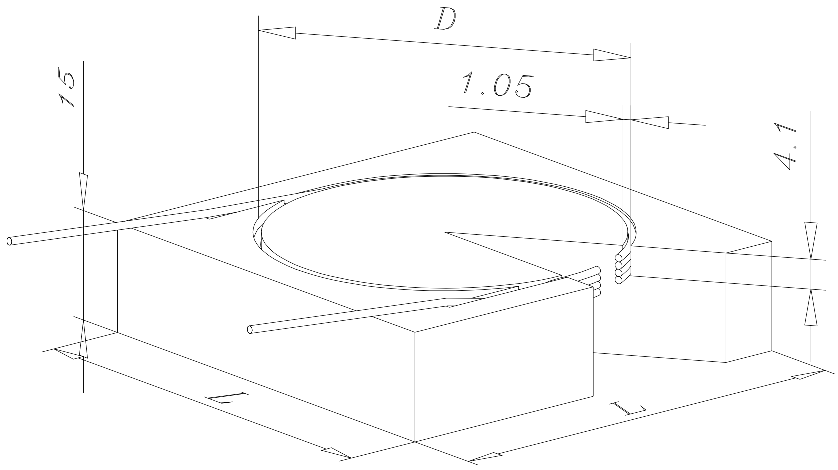

Region	*L,mm (SPD)*	*L,mm (PS)*	*D,mm*
inner	*39.2*	*39.5*	*37*
middle	*59.0*	*59.4*	*56*
outer	*118.4*	*119.1*	*110*

Figure 2.21: A scintillator cell. 3.5 loops of WLS fibre are embedded in a ring groove of rectangular cross section. The sides of the pad are wrapped with reflective paper.

three distinct regions, each containing a different pad size. The design and dimensions of the various pads is illustrated in figure 2.21.

Electron-pion separation is achieved with the PS. A pion rejection of 92% is expected with an electron purity of 95% for a threshold of 5 minimum ionising particles at L0.

2.8.2 ECAL

The ECAL has a sampling structure of 2 mm lead plates interspersed with 4 mm thick scintillating plates. The energy range of particles seen by the ECAL ranges from 200 GeV to tens of MeV. The hit density in the ECAL spans 2 orders of magnitude.

The cell size in the inner section is approximately equal to the Moliére radius which ensures that the majority of the energy deposited is contained within a 2 × 2 cluster of cells.

The three types of module that build up the inner, middle and outer sections of the ECAL detector have a very similar basic design. All module types have lead absorber plates of identical size, but they differ by the number of cells and therefore the number of scintillating tiles per module, as well as the fibre density. A module of the outer section consists of one single square cell of dimension 121.2 mm with 64 fibres running through the lead/scintillator stack. The middle section is made from modules that contain four square cells of dimension 60.6 mm and the inner section from modules that have nine cells of 40.4 mm size. Both the middle and inner section modules are read out through 144 fibres per module. The ECAL is shown in figure 2.22.

The average efficiency to identify electrons in the calorimeter acceptance from $\mathrm{J}/\psi \rightarrow \mathrm{e}^+\mathrm{e}^-$ decays in $\mathrm{B}^0 \rightarrow \mathrm{J}/\psi \mathrm{K}^0_\mathrm{S}$ events is 95%, with a pion misidentification rate of 0.7% [10].

2.8.3 HCAL

The HCAL (Fig. 2.23) is an iron/Scintillating tile calorimeter and has energy resolution of $80\%\sqrt{E} \oplus 10\%$. Tiles are positioned parallel to the beam axis. The HCAL is 1.2 m thick overall and has 4 mm of scintillator for every 16 mm of iron.

The HCAL is segmented into two sections with square cells of size 131.3 mm and 262.6 mm. The lateral dimensions of the two sections are ±2101 mm and ±4202 in x and ±1838 mm and ±3414 mm in y for the inner and outer section respectively.

2.9 MUON System

Muons provide a tag of the initial B-meson flavour states in semileptonic decays and are present in many $\mathcal{CP}$-sensitive decays, in particular the two “gold-plated” decays, $\mathrm{B}^0_\mathrm{d} \rightarrow \mathrm{J}/\psi(\mu^+\mu^-)\mathrm{K}^0_\mathrm{S}$ and $\mathrm{B}^0_\mathrm{s} \rightarrow \mathrm{J}/\psi(\mu^+\mu^-)\phi$. Requiring the muon candidate to have high

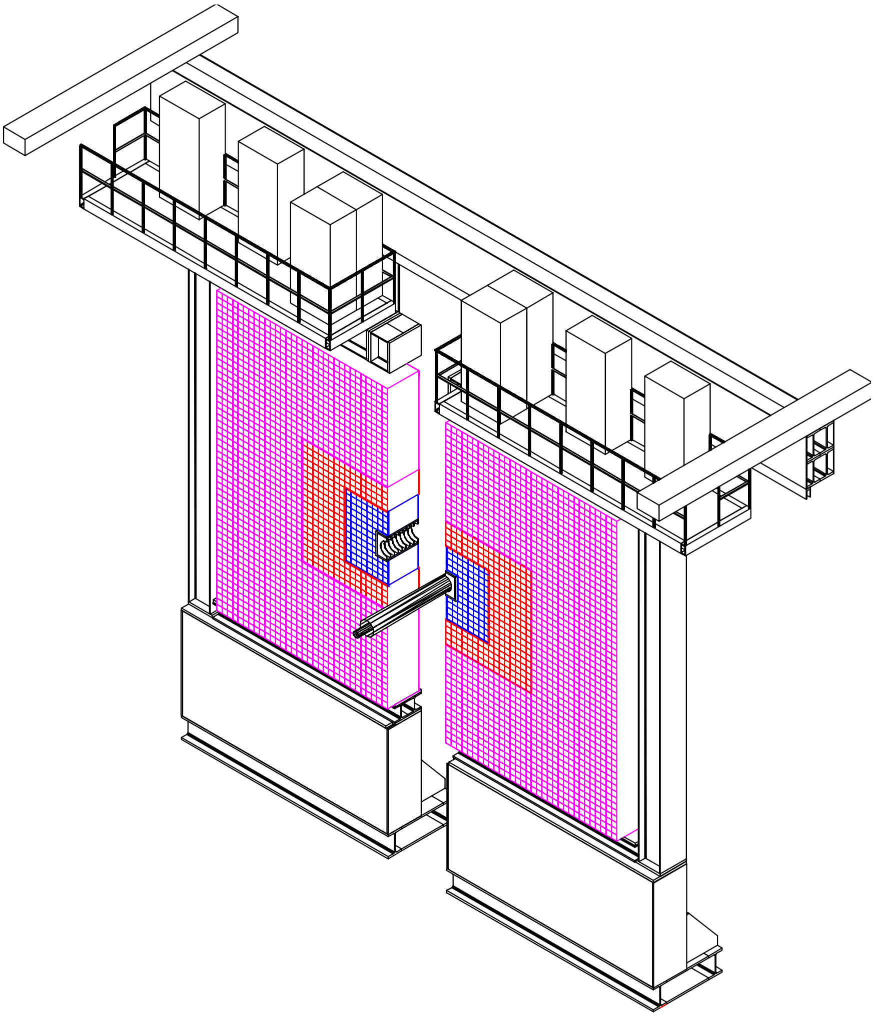

Figure 2.22: An isometric view showing the three sections of the ECAL. The readout electronics are located in the crates positioned at the top of the support structure. One detector half is partially retracted.

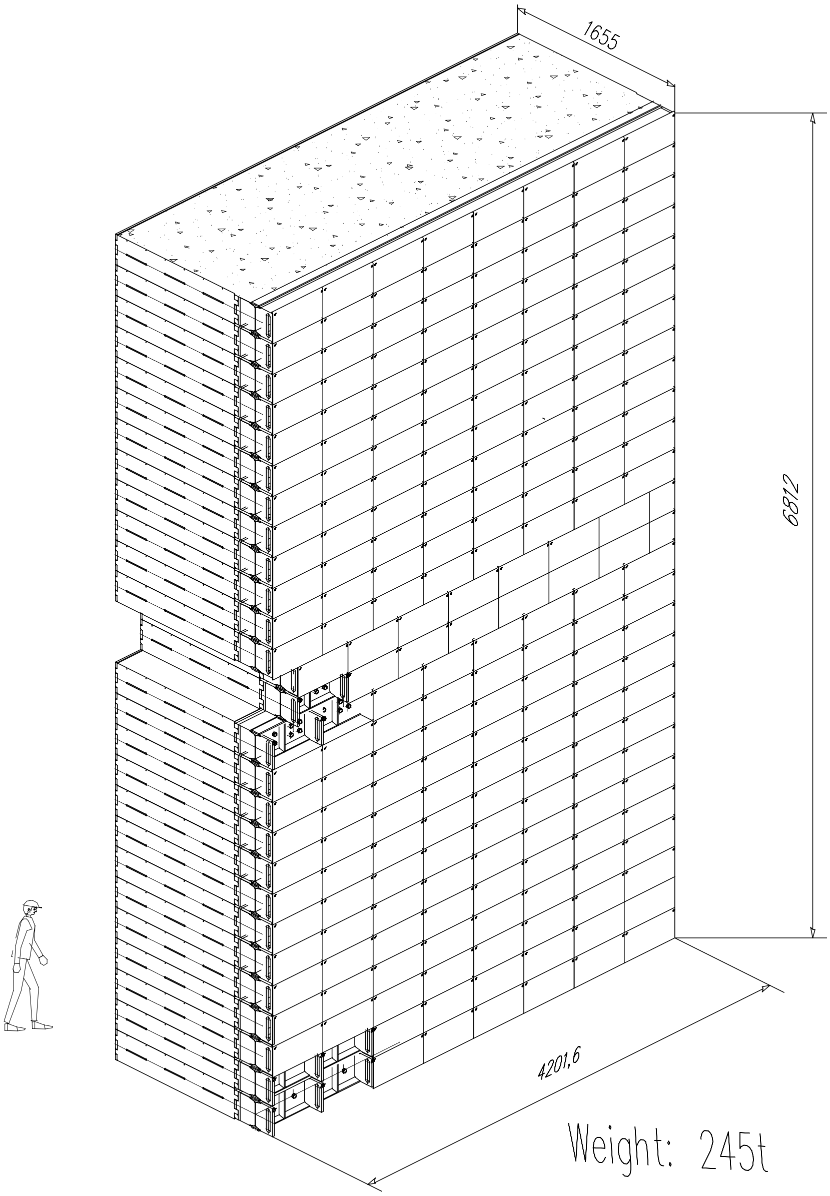

Figure 2.23: A schematic view of the HCAL. All detector modules are the of the same dimensions except those surrounding the beampipe.

transverse momentum, p_T, enriches the heavy flavour content of the triggered events.

The main requirement of the Muon Detectors is to provide a high p_T muon trigger at L0 [24]. The L0 muon trigger is based on a stand-alone muon track reconstruction and p_T measurement with 20% resolution. A muon candidate must hit all five stations to pass the trigger.

The muon system must also provide offline muon identification. Muons reconstructed in the tracking system with momenta down to $3\,\mathrm{GeV}/c$ must be correctly identified with an efficiency greater than 90% whilst keeping the pion misidentification probability below 1.5%. Efficient muon identification with low contamination is required for both tagging and the clean reconstruction of muonic final states.

The muon system consists of five stations, M1 - M5, positioned along the beam axis interspersed with shielding (Fig. 2.2). The stations obey a projective geometry and have an inner and an outer acceptance of 20 (16) and 306 (258) mrad in the bending (non-bending) plane. Each station is divided into four regions, R1 - R4, numbered with increasing distance to the beam axis. The shielding has a total thickness of approximately 20 nuclear interaction lengths and is composed of three iron absorbers, the ECAL systems and the HCAL. The granularity of the detector varies such that its contribution to the p_T resolution is approximately equal to the multiple-scattering contribution. The first station, M1, provides an important muon momentum measurement and is therefore placed before the calorimeters.

Two detector technologies are used, Multi Wire Proportional Chambers (MWPC) and Gas Electron Multipliers (GEM). Triple GEM detectors are used instead of MWPC in the inner region of M1 (M1R1) because the expected particle rate exceeds the safe MWPC ageing limit.

The triple GEM detector consists of three gas electron-multiplier foils sandwiched between anode and cathode planes. The foils are separated by millimetre-sized gaps.

The MWPC gas is Ar(45%), CO_2(15%) and CF_4(40%) and has a low sensitivity to neutron background since it contains no hydrogen. An average muon traversing the 5 mm gas gap generates approximately 50 drift electrons. In station M1 two single-gap

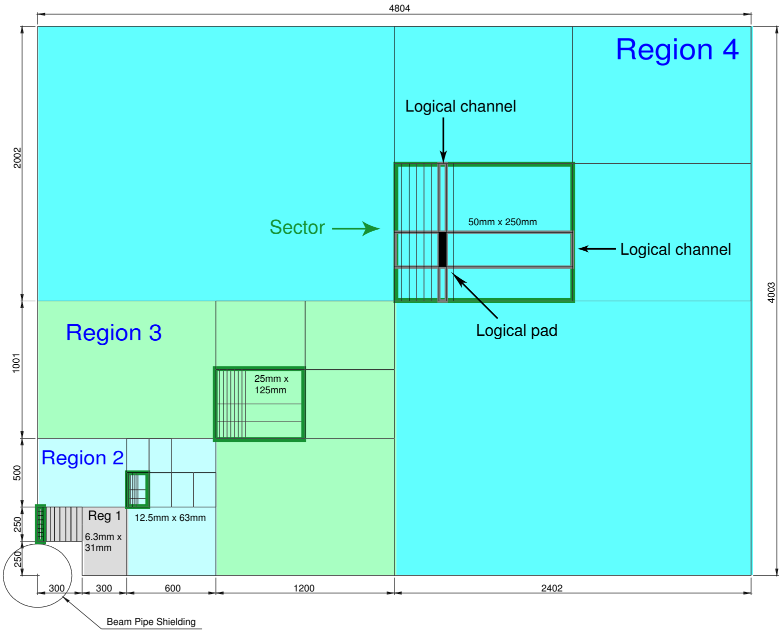

Figure 2.24: A view of one quadrant of muon station 2. A sector is highlighted in each region of the station. Dimensions of the channels scale by a factor of two between regions.

detectors (two triple-GEM in R1) are utilised in order to reduce the material in front of the ECAL. Stations M2 to M4 are composed of 4 gaps arranged in two independent double-gap detectors to increase redundancy.

All the chambers are segmented into physical pads. M1 - M3 have a higher spatial resolution along the x-plane (bending-plane) and are used to define the track direction and to measure the p_T of the candidate muon with a resolution of 20%. Stations M4 and M5 are mainly used to select penetrating particles and have a limited spatial resolution. The length of the wires dictates the resolution in the y-direction. The requirement on y-resolution limits the length of the chambers to less then 30 cm. In order to reduce the amount of data sent to the L0 trigger, the outer regions combine rows and columns of chambers into one logical pad. The required hit precision is then obtained by identifying the overlap between the hit row and column. Figure 2.24 shows the layout of the regions of M2.

2.9.1 Performance

Using a sample of $\mathrm{B}^0 \to \mathrm{J}/\psi\mathrm{K}^0_\mathrm{S}$ decays, the muon identification efficiency was measured to be $\epsilon(\mu) = 94.3 \pm 0.3\%$ with a pion mis-identificaion of $\epsilon(\pi \to \mu) = 2.9 \pm 0.1\%$. A high muon identification purity ($\sim 99\%$) can be achieved through the use of information from the RICH and calorimeter systems [10].

2.10 The Trigger System

LHCb will operate at a luminosity of $2 \cdot 10^{32}\,\mathrm{cm}^{-2}\mathrm{s}^{-1}$. At this luminosity, interactions producing a minimum of 2 reconstructible particles within the detector acceptance will occur at a rate of 10 MHz. Of these events, $b\bar{b}$ pairs are expected to be produced at a rate of approximately 100 kHz.

The LHCb trigger must select events which are interesting for B-physics studies [25]. A two-level system, Level-0 (L0) and the High Level Trigger (HLT) is used which exploits the fact that B-hadrons are heavy and have a long lifetime.

2.10.1 The Level-0 Trigger

The decay of a B-hadron will, in general, produce a large E_T hadron, lepton or photon. The L0 trigger makes use of this fact and uses information from the calorimeters and muon chambers to reconstruct the highest E_T photon, hadron and electron and the two highest E_T muons. In addition to reconstructing high E_T particles, the L0 trigger must also reject events which are too difficult to reconstruct in the given time-frame or stem from beam-halo particles.

The L0 trigger can be further broken down into three sub-triggers:

- The pile-up veto system.
- The L0 calorimeter trigger.
- The L0 muon trigger.

Information from all three sub-triggers is passed onto the L0 Decision Unit (L0DU). The L0DU combines this information into one decision per bunch crossing. The three sub-triggers are described below.

2.10.1.1 The Pile-up Veto System

The pile-up veto system estimates the number of primary pp interactions in each bunch crossing. It uses two planes of silicon microstrip sensors perpendicular to the beamline to measure the radial position of tracks. The z-position of the vertex is calculated using the simple formula:

$$z_v = \frac{kz_a - z_b}{k-1} \tag{2.3}$$

where k is the ratio of the radial hit position at plane a and plane b,

$$k = \frac{r_b}{r_a}. \tag{2.4}$$

An histogram is produced from the hits and the largest peak identified. Two-interaction crossings are identified with an efficiency of 60% and a purity of approximately 95%.

2.10.1.2 The L0 Calorimeter Trigger

The L0 trigger uses information from the calorimeters and muon chambers to reconstruct the two highest E_T muons and the highest E_T photon, hadron and electron. The purpose of the L0 calorimeter trigger is to identify the particles which deposit large transverse energy, E_T, in the calorimeters and obtain a measure of the particle multiplicity. Zones of 2×2 cells are used. Each zone is sufficiently small to minimise overlap between neighbouring particles but large enough to contain the majority of the energy deposit of each particle. The same front-end card is used for both the ECAL and HCAL.

A three stage selection system is used:

- The highest E_T measured a zone in both the ECAL and HCAL is selected.
- The Validation Card uses data from the ECAL, SPD and PS to identify the highest E_T candidate π^0, photon and electron in various sections of the calorimeter systems.

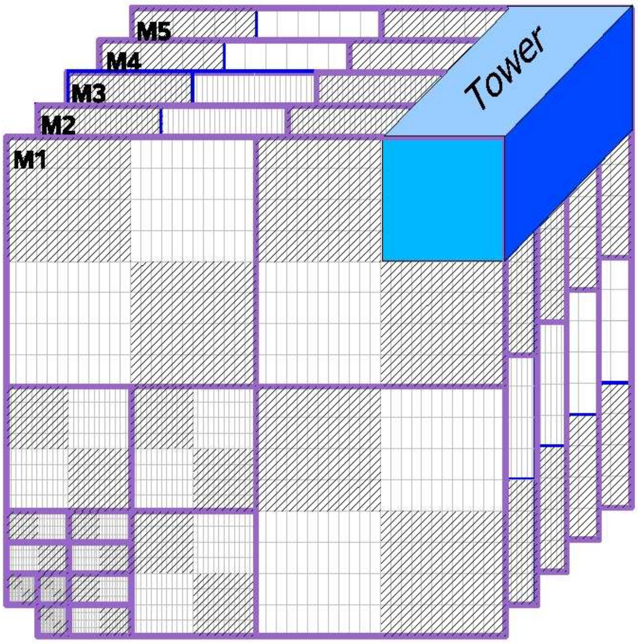

Figure 2.25: A schematic diagram of the muon stations showing the tower layout. The areas of the system analysed by one processing board are marked by thick lines. The interaction point is moved to infinity in this view.

- The Selection Crate then selects the highest global E_T candidate of each type, measures the total E_T in the HCAL and the total SPD multiplicity.

The total E_T, SPD multiplicity and highest E_T hadron, electron, photon and π^0 candidates are output to the L0DU.

2.10.1.3 The L0 Muon Trigger

High p_T muons are a characteristic of B-events. The L0 muon trigger searches for the two highest p_T muons in the the detector. The momentum of the muons is measured with a precision of $\sigma_p/p \approx 20\%$.

The four quadrants of the muon system are treated independently. The muon detector is subdivided into 192 towers which point towards the interaction region (Fig.

2.25). Each tower has the same layout of logical pads (Sec. 2.9) which allows the same processing to be performed for all towers. Each tower is connected to a Processor Unit (PU). The intersection of a tower and a station is termed a sector. Data from each tower is sent to one PU. In order to prevent inefficiencies from the boundary between regions, data from neighbouring regions is also sent to a PU.

Within each tower, a logical pad hit in the third muon station is used as a track seed. A straight-line extrapolation from the hit to the interaction point is performed. Hits are then searched for in Fields Of Interest (FOI) which are defined along the extrapolated line. If a minimum of one hit is found in each of the FOIs then a muon track is assumed. The logical pad closest to the extrapolation is then selected. The track position in M1 is then calculated using a straight-line extrapolation from M2 and M3.

The transverse momentum of the muon is evaluated using lookup tables based on the position of the hits in M1 and M2. The two highest momentum tracks in each quadrant are selected and the information transferred to the L0DU.

2.10.2 The High Level Trigger

The HLT receives events from L0 at a maximum rate of 1 MHz. All detector information is fed into an event-filter farm consisting of 1800 CPUs [26]. The HLT uses a number of "trigger alleys" to make the decision to write the event to tape. At present, there are four distinct alleys:

- The muon alley.
- The muon and hadron alley.
- The hadron alley.
- The ECAL alley.

The alleys can be run in any combination depending on the status of the L0DU [27].

In addition to the trigger alleys, inclusive and exclusive selections will also be applied by the HLT. The output rates for the various HLT components are expected to be:

- Exclusive b (∼200 Hz).
- D^* (∼ 300 Hz).
- Di-muon (∼600 Hz).
- Inclusive $b \rightarrow \mu$ (∼900 Hz).

for a total output rate of 2 kHz [28].

2.11 LHCb Software

The LHCb software framework is designed to be flexible enough to accommodate changes in requirements and technology over the lifetime of the experiment. The software architecture, called Gaudi, supports event data processing applications that run in different processing environments ranging from real-time triggers in the on-line system to the final physics analyses performed by physicists. The LHCb reconstruction (Brunel), the trigger application (HLT), the analysis framework (DaVinci), the digitisation (Boole) together with the simulation application (Gauss) based on Geant4 [29], and the event and detector visualisation program (Panoramix) are all based on the Gaudi framework. The software is developed in C++ and object-oriented technologies have been implemented throughout.

Detailed descriptions of the individual LHCb software packages and frameworks are outside of the scope of this document and can be found in the LHCb Computing Technical Design Report [30].

2.12 Summary

The LHCb experiment is a forward single-arm spectrometer dedicated to the study of $\mathcal{CP}$ violation and other rare phenomena in the B-system. High resolution particle lifetime measurements are made possible by the precision vertex system. Efficient particle identification is achieved through the twin RICH detectors. The features of the detector are essential for the time-dependent $\mathcal{CP}$ asymmetry measurement proposed in chapter 6.

Chapter 3

Theory

3.1 Introduction

The operators $\mathcal{C}$, $\mathcal{P}$ and $\mathcal{T}$ are introduced in the context of a Lagrangian field theory. $\mathcal{CP}$ violation within the Standard Model (SM) is described in section 3.3. The CKM matrix and the CKM triangle are introduced. The properties of the CKM matrix are detailed in section 3.4.

Section 3.5 introduces the formalism for neutral meson mixing and the expressions describing the time-dependent decay rates to $\mathcal{CP}$ eigenstates. The three types of $\mathcal{CP}$ violation are identified in section 3.6. Finally, the current status of the CKM parameters are reviewed in section 3.7.

3.2 $\mathcal{C}, \mathcal{P}$ and $\mathcal{T}$ in Field Theory

3.2.1 Charge Conjugation

Charge conjugation, $\mathcal{C}$, exchanges particles with their antiparticle counterparts:

$$\mathcal{C} : q^{+} \rightarrow q^{-}. \tag{3.1}$$

It changes the quantum numbers of the original particle to their negative values but preserves momentum, mass and spin.

3.2.2 Parity

The Parity operator, $\mathcal{P}$, has the effect of reflecting all vectors through the origin:

$$\mathcal{P} : x^{\mu} \rightarrow -x^{\mu}. \tag{3.2}$$

Polar vectors, x^{μ}_{V}, change sign under parity whereas axial vectors, x^{μ}_{av}, do not:

$$\mathcal{P} : x^{\mu}_{\mathrm{V}} \rightarrow -x^{\mu}_{\mathrm{V}}, \quad \mathcal{P} : x^{\mu}_{\mathrm{av}} \rightarrow x^{\mu}_{\mathrm{av}}. \tag{3.3}$$

Similarly, scalars, x_s, and pseudoscalars, x_{ps}, behave differently under parity:

$$\mathcal{P} : x_{\mathrm{S}} \rightarrow x_{\mathrm{S}}, \quad \mathcal{P} : x_{\mathrm{ps}} \rightarrow -x_{\mathrm{ps}}. \tag{3.4}$$

3.2.3 Time Reversal

Time reversal, $\mathcal{T}$, reflects t into $-t$:

$$\mathcal{T} : t \rightarrow -t, \tag{3.5}$$

and has the effect of reversing the direction of motion of particles.

3.2.4 General Properties

The operators $\mathcal{C}, \mathcal{P}$ and $\mathcal{T}$ are their own inverse:

$$\begin{aligned} \mathcal{C}^2 &= 1 \\ \mathcal{P}^2 &= 1 \\ \mathcal{T}^2 &= 1 \end{aligned} \tag{3.6}$$

i.e., they have eigenvalues of ± 1. They leave the vacuum state unchanged:

$$\mathcal{C}|0\rangle = |0\rangle, \quad \mathcal{P}|0\rangle = |0\rangle, \quad \mathcal{T}|0\rangle = |0\rangle. \tag{3.7}$$

Apart from the weak interactions, $\mathcal{C}$, $\mathcal{P}$ and $\mathcal{T}$ are symmetries of the SM.

3.2.5 The $\mathcal{CPT}$ Theorem

The transformation $\mathcal{CPT}$ can always be defined for any local field theory such that it represents an exact symmetry [31]:

$$(\mathcal{CPT})\mathcal{L}(t,x)(\mathcal{CPT})^{-1} = \mathcal{L}(-t,-x), \tag{3.8}$$

it follows from the locality, Lorentz invariance, and hermicity of the Lagrangian. Given that $\mathcal{CPT}$ invariance holds for the SM, the operation $\mathcal{T}$ is equivalent to $\mathcal{CP}$.

The $\mathcal{CPT}$ theorem implies that the masses and widths of particles and antiparticles are equal:

$$M(P) = M(\bar{P}), \quad \Gamma(P) = \Gamma(\bar{P}). \tag{3.9}$$

3.3 $\mathcal{CP}$ in the SM

The SM is composed of several "flavours" of quarks and leptons which interact through the exchange of gauge bosons. The interactions are determined by imposing local gauge invariance of the group

$$SU(3) \times SU(2) \times U(1)_Y, \tag{3.10}$$

where $SU(3)$ and $SU(2) \times U(1)_Y$ are the strong and electroweak gauge groups respectively.

The fermions are:

- Up-type quarks (u,c,t).
- Down-type quarks (d,s,b).
- Charged leptons (e^-, μ^-, τ).
- Neutrinos (ν_e, ν_μ, ν_τ).

The gauge bosons are:

- The electroweak bosons, the photon, $\mathrm{W}^\pm$ and Z.

- The strong boson, the gluon, g.

Masses are generated through the interaction of these particles with one scalar field:

- The Higgs boson, H.

3.3.1 Origin of $\mathcal{CP}$ Violation in the SM

$\mathcal{CP}$ violation in the SM is due to complex couplings. This can be demonstrated using the following argument: consider some operator, h, which causes some transition between two states. The relevant interaction Hamiltonian is:

$$H_{\text{int}} = ch + c^* h^\dagger, \tag{3.11}$$

where c is a complex constant. Under $\mathcal{CP}$ h transforms as:

$$\mathcal{CP} h \mathcal{CP}^{-1} = h^\dagger, \tag{3.12}$$

since $\mathcal{CP}$ is a linear operator. Applying $\mathcal{CP}$ to the Hamiltonian we have:

$$\mathcal{CP} H_{\text{int}} \mathcal{CP}^{-1} = ch^\dagger + c^* h. \tag{3.13}$$

It is now obvious that the Hamiltonian remains unchanged under $\mathcal{CP}$ only if c is real. $\mathcal{CP}$ violation therefore requires the presence of a complex phase[1].

3.4 The CKM Matrix

The CKM matrix links the mass eigenstates of the down-type quarks, (d, s, b), and the $SU(2)$ partners of the up-type quarks, $(\tilde{d}, \tilde{s}, \tilde{b})$:

$$\begin{pmatrix} \tilde{d} \\ \tilde{s} \\ \tilde{b} \end{pmatrix} = \mathbf{V}_{\text{CKM}} \begin{pmatrix} d \\ s \\ b \end{pmatrix}. \tag{3.14}$$

---

[1] Note that the presence of a complex phase does not guarantee the existence of a $\mathcal{CP}$-violating observable.

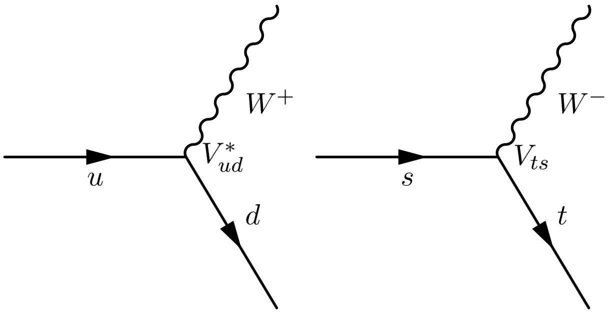

Figure 3.1: Simple weak interactions showing the points at which CKM elements are introduced.

Interactions with the charged weak bosons therefore allow the conversion of up-type quarks to down-type quarks of another generation. It is for this reason that the elements of the CKM matrix are labelled according to the relevant quark conversion:

$$\mathbf{V}_{\text{CKM}} = \begin{pmatrix} V_{ud} & V_{us} & V_{ub} \\ V_{cd} & V_{cs} & V_{cb} \\ V_{td} & V_{ts} & V_{tb} \end{pmatrix}. \tag{3.15}$$

Examples of weak interactions where the relevant CKM matrix element is explicitly identified are shown in 3.1.

3.4.1 Parameters of the CKM Matrix

It is instructive to determine the number of independent parameters required to fully describe the CKM matrix. We first note that the CKM matrix must be unitary to conserve probability. A 3×3 unitary matrix can have nine independent parameters. In this case, there are six possible fermions which are involved in the charged boson interaction. Since we are free to choose the phase of the quark fields, we may remove five of the nine parameters through relative phase definitions. The CKM matrix is therefore determined by four independent parameters.

If the CKM matrix were real, then only three parameters would be required to describe it. The CKM matrix for three generations can therefore be defined by three independent rotation angles (Euler angles) and one complex phase.

3.4.2 The Wolfenstein Parameterisation

A common parameterisation of the CKM matrix is the Wolfenstein Parameterisation (Eqn. 3.16). The matrix elements are expanded in powers of $\sin\theta_C = \lambda$, where θ_C is the Cabibbo angle and $\sin\theta_C \approx 0.22$. The expansion is chosen such that the real-valued parameters, A, η, and ρ, are all of order unity:

$$\begin{pmatrix} V_{ud} & V_{us} & V_{ub} \\ V_{cd} & V_{cs} & V_{cb} \\ V_{td} & V_{ts} & V_{tb} \end{pmatrix} \cong \begin{pmatrix} 1-\lambda^2/2 & \lambda & A\lambda^3\left(\rho - i\eta\right) \\ -\lambda & 1-\lambda^2/2 & A\lambda^2 \\ A\lambda^3\left(1-\rho-i\eta\right) & -A\lambda^2 & 1 \end{pmatrix} + \delta V, \qquad (3.16)$$

where

$$\delta V \cong \begin{pmatrix} 0 & 0 & 0 \\ -iA^2\lambda^5\eta & 0 & 0 \\ A\lambda^5\left(\rho+i\eta\right)/2 & A\lambda^4\left(1/2-\rho-i\eta\right) & 0 \end{pmatrix} + \mathcal{O}\left(\lambda^6\right). \qquad (3.17)$$

3.4.3 Unitarity Relations

There are six equations, stemming from the unitarity of the CKM matrix, which can be expressed as triangles in the complex plane. The triangles fall into three categories:

1. The triangles relating to strange and charm decays. Due to one of the complex-valued sides having a length of $\mathcal{O}(\lambda^5)$, these two triangles are extremely flattened. The K^0 Triangle:

$$\begin{array}{ccccccc} V_{ud}V_{us}^* & + & V_{cd}V_{cs}^* & + & V_{td}V_{ts}^* & = & 0, \\ \mathcal{O}(\lambda) & & \mathcal{O}(\lambda) & & \mathcal{O}(\lambda^5) & & \end{array} \qquad (3.18)$$

   and the D^0 triangle:

$$\begin{array}{ccccccc} V_{ud}V_{cd}^* & + & V_{us}V_{cs}^* & + & V_{ub}V_{cb}^* & = & 0. \\ \mathcal{O}(\lambda) & & \mathcal{O}(\lambda) & & \mathcal{O}(\lambda^5) & & \end{array} \qquad (3.19)$$

2. The B_s^0 and *ct* triangles. Again these triangles are flattened but slightly less so, one of the complex-valued sides is a factor $\mathcal{O}(\lambda^2) \approx 4.8\cdot10^{-2}$ smaller than the others.

The $\mathrm{B}_{\mathrm{s}}^0$ Triangle:

$$\begin{array}{ccccccc} V_{us}V_{ub}^* & + & V_{cs}V_{cb}^* & + & V_{ts}V_{tb}^* & = & 0, \\ \mathcal{O}(\lambda^4) & & \mathcal{O}(\lambda^2) & & \mathcal{O}(\lambda^2) & & \end{array} \tag{3.20}$$

and the *ct* triangle:

$$\begin{array}{ccccccc} V_{td}V_{cd}^* & + & V_{ts}V_{cs}^* & + & V_{tb}V_{cb}^* & = & 0. \\ \mathcal{O}(\lambda^4) & & \mathcal{O}(\lambda^2) & & \mathcal{O}(\lambda^2) & & \end{array} \tag{3.21}$$

3. The $\mathrm{B}_{\mathrm{d}}^0$ and *ut* triangles. All the sides of these triangles are of $\mathcal{O}(\lambda^3)$ and hence have angles which are all necessarily large.

   The $\mathrm{B}_{\mathrm{d}}^0$ Triangle:

$$\begin{array}{ccccccc} V_{ud}V_{ub}^* & + & V_{cd}V_{cb}^* & + & V_{td}V_{tb}^* & = & 0, \\ \mathcal{O}(\lambda^3) & & \mathcal{O}(\lambda^3) & & \mathcal{O}(\lambda^3) & & \end{array} \tag{3.22}$$

and the *ut* triangle:

$$\begin{array}{ccccccc} V_{td}V_{ud}^* & + & V_{ts}V_{us}^* & + & V_{tb}V_{ub}^* & = & 0. \\ \mathcal{O}(\lambda^3) & & \mathcal{O}(\lambda^3) & & \mathcal{O}(\lambda^3) & & \end{array} \tag{3.23}$$

The $\mathrm{B}_{\mathrm{d}}^0$ triangle is generally referred to as "The CKM Triangle". Both the $\mathrm{B}_{\mathrm{d}}^0$ and *ut* triangles are shown in figure 3.2.

3.4.4 CKM Angles

Two conventions for naming the internal angles of the CKM triangle are common. The first convention labels the angles α, β, γ and is used throughout this document, whilst the second uses the labels ϕ_2, ϕ_1 and ϕ_3 respectively. The angles of the CKM triangle are given by:

$$\begin{aligned} \alpha &= \arg\left(\frac{V_{td}V_{tb}^*}{-V_{ud}V_{ub}^*}\right) \\ \beta &= \pi - \arg\left(\frac{-V_{cd}V_{cb}^*}{-V_{td}V_{tb}^*}\right) \\ \gamma &= \arg\left(\frac{V_{ud}V_{ub}^*}{-V_{cd}V_{cb}^*}\right). \end{aligned} \tag{3.24}$$

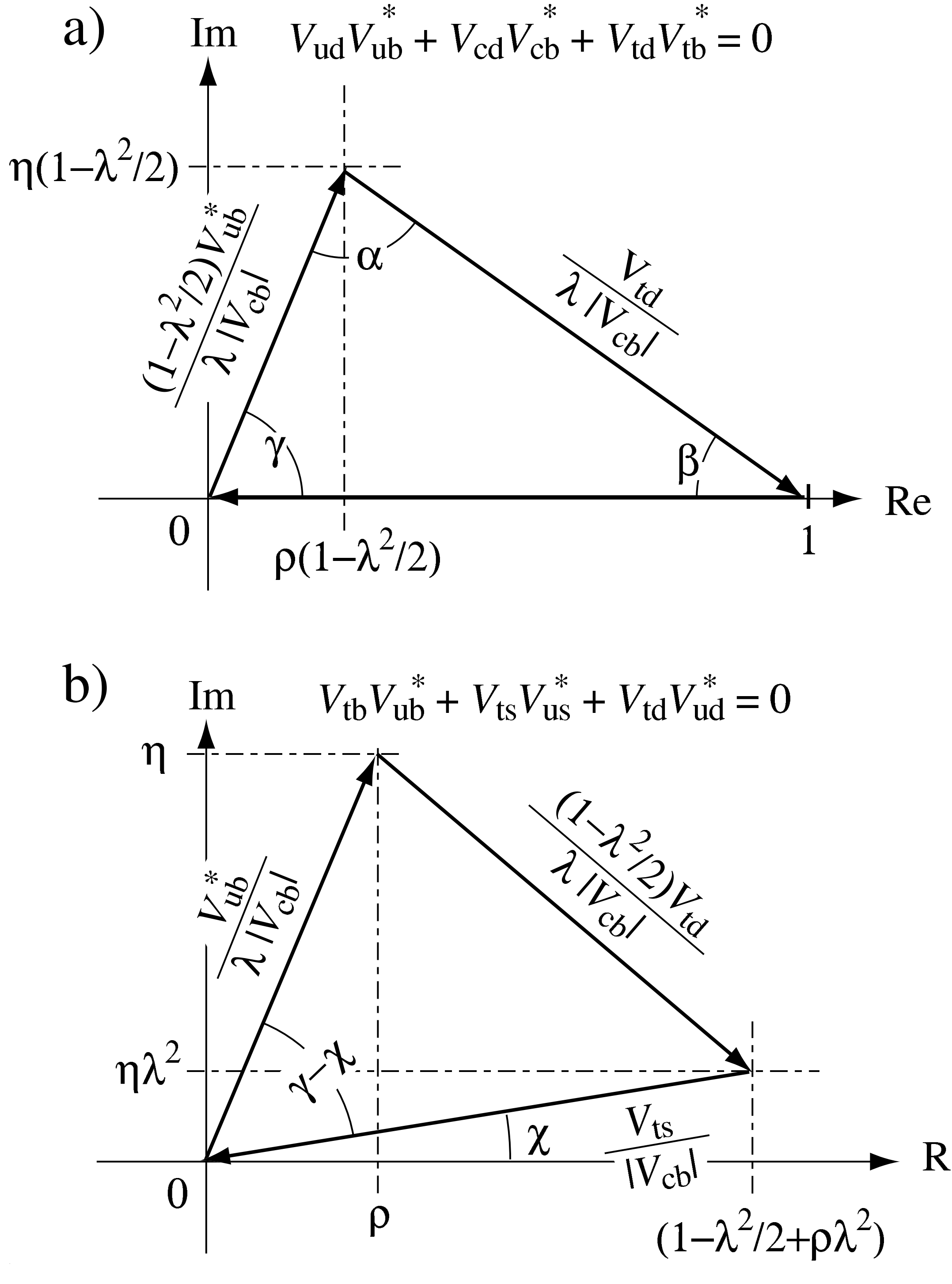

Figure 3.2: The two CKM triangles with sides of $\mathcal{O}(\lambda^3)$. Both triangles have been divided by $V_{cd}V_{cb}^*$ such that one side of the B^0 triangle lies on the real axis.

Up to $\mathcal{O}(\lambda^4)$ in the Wolfenstein parameterisation only three of the CKM matrix elements are complex. The elements associated with the angles β, γ and χ are:

$$\arg V_{td} = -\beta \tag{3.25}$$

$$\arg V_{ub} = -\gamma \tag{3.26}$$

$$\arg V_{ts} = \pi + \chi. \tag{3.27}$$

We can therefore readily identify processes with which to measure the CKM angles β and γ. Namely, $t \to d$ transitions for γ measurements and $b \to u$ transitions for measurements of β.

3.4.5 Area of CKM Triangles

All the CKM triangles have the same area, $|J|/2$. J is given by:

$$J = \mathsf{Im}\left[V_{ij}V_{kj}^{*}V_{kl}V_{il}^{*}\right]\sum_{m}\epsilon_{ikm}\sum_{n}\epsilon_{jln}, \tag{3.28}$$

where ϵ_{abc} is the Levi-Civita symbol.

3.5 Mixing Formalism

3.5.1 Time Evolution of Neutral Mesons

The Schrödinger Equation for a superposition of flavour eigenstates, $a|\mathrm{B}^0\rangle + b|\overline{\mathrm{B}}^0\rangle$, is:

$$i\frac{\mathrm{d}}{\mathrm{d}t}\begin{pmatrix} a \\ b \end{pmatrix} = \mathbf{H}\begin{pmatrix} a \\ b \end{pmatrix}. \tag{3.29}$$

This is the Schrödinger Equation restricted to the $|\mathrm{B}^0\rangle - |\overline{\mathrm{B}}^0\rangle$ subspace of state vectors. The system is allowed to leave the $|\mathrm{B}^0\rangle - |\overline{\mathrm{B}}^0\rangle$ subspace by decaying to other particles, hence $\mathbf{H}$ in equation 3.29 will not be Hermitian. A general matrix $\mathbf{H}$ can be expressed in term of the Hermitian matrices $\mathbf{M}$ and $\mathbf{\Gamma}$ as

$$\mathbf{H} = \mathbf{M} - \frac{i}{2}\mathbf{\Gamma}, \tag{3.30}$$

where the Hermitian part, $\mathbf{M}$, represents the energy (mass) of the system, while the non-Hermitian part, $\frac{i}{2}\mathbf{\Gamma}$, represents the decay to other states. $\mathcal{CPT}$ invariance implies

$$\langle \mathrm{B}^0|\mathbf{H}|\mathrm{B}^0\rangle = \langle \overline{\mathrm{B}}^0|\mathbf{H}|\overline{\mathrm{B}}^0\rangle. \tag{3.31}$$

Therefore the diagonal elements of $\mathbf{H}$ are the same and $\mathbf{H}$ can be written as:

$$\mathbf{H} = \begin{pmatrix} H_{11} & H_{12} \\ H_{21} & H_{11} \end{pmatrix},$$

with

$$\mathbf{M} = \begin{pmatrix} M_{11} & M_{12} \\ M_{12}^* & M_{11} \end{pmatrix}, \quad \text{and} \quad \mathbf{\Gamma} = \begin{pmatrix} \Gamma_{11} & \Gamma_{12} \\ \Gamma_{12}^* & \Gamma_{11} \end{pmatrix}. \tag{3.32}$$

The effective Hamiltonian can be more simply expressed as:

$$\mathbf{H} = \begin{pmatrix} m - \frac{i}{2}\gamma & M_{12} - i\Gamma_{12} \\ M_{12}^* + i\Gamma_{12}^* & m - \frac{i}{2}\gamma \end{pmatrix} \tag{3.33}$$

where $m = M_{11}$ and $\gamma = \Gamma_{11}$. The physical meson states with well-defined mass and decay width are the eigenvectors of $\mathbf{H}$:

$$|B_{H,L}\rangle = p|\mathrm{B}^0\rangle \mp q|\overline{\mathrm{B}}^0\rangle \tag{3.34}$$

which have eigenvalues λ_H and λ_L respectively. The subscripts L and H stand for the "light" and the "heavy" physical B^0-states, which have masses $M_{H,L}$ and widths $\Gamma_{H,L}$. The mass and width difference between the two states is:

$$\Delta m = M_H - M_L, \quad \Delta\Gamma = \Gamma_L - \Gamma_H. \tag{3.35}$$

The average B^0 lifetime is

$$\Gamma \equiv \frac{1}{2}\left(\Gamma_L + \Gamma_H\right). \tag{3.36}$$

Solving the characteristic equation for the effective Hamiltonian we find that

$$\lambda_{H,L} = m - \frac{i\gamma}{2} \pm pq \tag{3.37}$$

where,

$$pq = \sqrt{\left(M_{12} - \frac{i}{2}\Gamma_{12}\right)\left(M_{12}^{*} - \frac{i}{2}\Gamma_{12}^{*}\right)} \tag{3.38}$$

and

$$\frac{q}{p} = \sqrt{\frac{M_{12}^{*} - \frac{i}{2}\Gamma_{12}^{*}}{M_{12} - \frac{i}{2}\Gamma_{12}}}. \tag{3.39}$$

3.5.2 Physical Observables, $\Delta m, \Delta\Gamma$ and a

Examining the time evolution of the eigenvectors we can identify the terms corresponding to the mass and width of the two states.

$$|B_{H,L}, t\rangle = e^{-i\mathbf{H}t}|B_{H,L}, t = 0\rangle \tag{3.40}$$

Since $|B_{H,L}, t = 0\rangle$ is an eigenvector of $\mathbf{H}$ we can replace $\mathbf{H}$ with the corresponding eigenvalue:

$$|B_{H,L}, t\rangle = e^{i\lambda_{H,L}t}|B_{H,L}, t = 0\rangle. \tag{3.41}$$

Writing this explicitly for the two states:

$$|B_{H,L}, t\rangle = e^{-it\left(m - \frac{i\gamma}{2} \pm \sqrt{\left(M_{12} - \frac{i}{2}\Gamma_{12}\right)\left(M_{12}^{*} - \frac{i}{2}\Gamma_{12}^{*}\right)}\right)}|B_H, t = 0\rangle. \tag{3.42}$$

It is now possible to identify terms corresponding to the mass and width of the $|B_H\rangle$ and $|B_L\rangle$ states:

$$m_{H,L} = m \pm \mathsf{Re}\left(\sqrt{\left(M_{12} - \frac{i}{2}\Gamma_{12}\right)\left(M_{12}^{*} - \frac{i}{2}\Gamma_{12}^{*}\right)}\right), \tag{3.43}$$

$$\Gamma_{H,L} = \gamma \mp 2i\mathsf{Im}\left(\sqrt{\left(M_{12} - \frac{i}{2}\Gamma_{12}\right)\left(M_{12}^{*} - \frac{i}{2}\Gamma_{12}^{*}\right)}\right). \tag{3.44}$$

The expressions for Δm and $\Delta\Gamma$ are:

$$\Delta m = 2\mathsf{Re}\left(\sqrt{\left(M_{12} - \frac{i}{2}\Gamma_{12}\right)\left(M_{12}^{*} - \frac{i}{2}\Gamma_{12}^{*}\right)}\right), \tag{3.45}$$

$$\Delta\Gamma = -4\mathsf{Im}\left(\sqrt{\left(M_{12} - \frac{i}{2}\Gamma_{12}\right)\left(M_{12}^{*} - \frac{i}{2}\Gamma_{12}^{*}\right)}\right). \tag{3.46}$$

The mass and width difference in the B^0 systems are related to M_{12}, Γ_{12} by:

$$\Delta m = 2\,|M_{12}| - \frac{|\Gamma_{12}|^2 \sin^2\phi}{4\,|M_{12}|}, \tag{3.47}$$

$$\Delta\Gamma = 2\,|\Gamma_{12}| \cos\phi, \tag{3.48}$$

where the phase, ϕ is defined through:

$$\frac{M_{12}}{\Gamma_{12}} = -\left|\frac{M_{12}}{\Gamma_{12}}\right| e^{i\phi}. \tag{3.49}$$

Equations 3.47 and 3.48 link two observables ($\Delta\Gamma$, Δm) to three parameters, $|M_{12}|$, $|\Gamma_{12}|$, ϕ. The third observable, allowing us to solve the system, is

$$a_{fs} \equiv \left|\frac{\Gamma_{12}}{M_{12}}\right| \sin\phi. \tag{3.50}$$

This parameter is related to p, q by:

$$\left|\frac{q}{p}\right| = 1 - \frac{a_{fs}}{2}. \tag{3.51}$$

So it measures the deviation of $\left|\frac{q}{p}\right|$ from unity and hence $\mathcal{CP}$ violation in mixing. The subscript on a_{fs} stands for "flavour-specific" since it is measured in flavour-specific decays.

3.5.3 Diagrams Contributing to M_{12} and Γ_{12}

The major contributions to M_{12} within the SM are from box diagrams containing an internal top quark. Γ_{12} originates from states into which both B^0 and $\overline{\mathrm{B}}^0$ can decay and is dominated by $c\bar{c}$ production.

Detailed derivations of the matrix elements M_{12} and Γ_{12} in terms of SM parameters are given in [32] and [33].

3.5.4 Time Dependence of $|\mathbf{B}^0(t)\rangle$

From equation 3.34 we can express the mass-eigenstates in terms of the $\mathcal{CP}$ eigenstates:

$$|B_H(t)\rangle = p|\mathrm{B}^0(t)\rangle - q|\overline{\mathrm{B}}^0(t)\rangle, \tag{3.52}$$

$$|B_L(t)\rangle = p|\mathrm{B}^0(t)\rangle + q|\overline{\mathrm{B}}^0(t)\rangle, \tag{3.53}$$

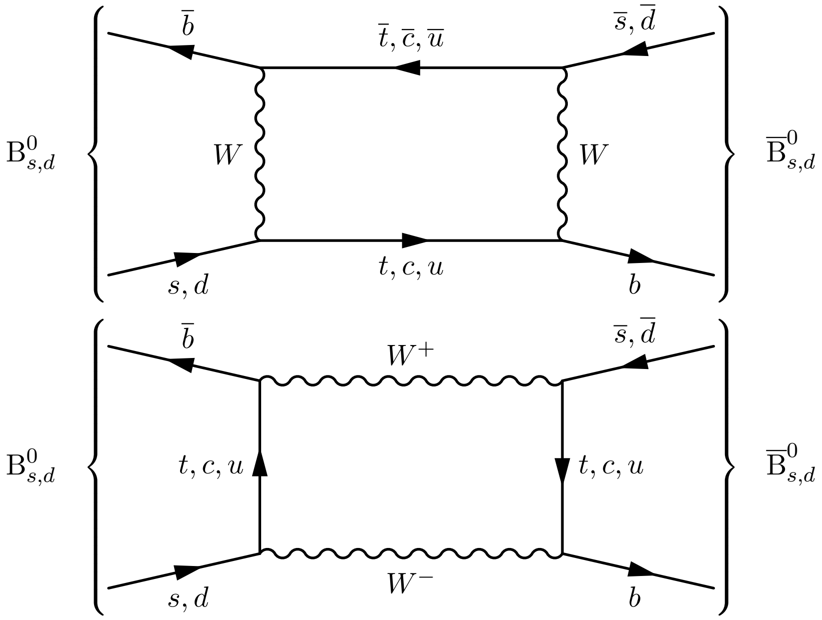

Figure 3.3: Leading order box diagrams involved in B-mixing.

which can be inverted to obtain:

$$|B^0(t)\rangle = \frac{1}{2p}\left(|B_L(t)\rangle + |B_H(t)\rangle\right), \tag{3.54}$$

$$|\overline{B}^0(t)\rangle = \frac{1}{2q}\left(|B_L(t)\rangle - |B_H(t)\rangle\right). \tag{3.55}$$

Using equation 3.40 to insert the time-dependence of $|B^0(t)\rangle$ and $|\overline{B}^0(t)\rangle$ explicitly:

$$|B^0(t)\rangle = \frac{1}{2p}\left[e^{-\left(iM_L+\frac{1}{2}\Gamma_L\right)t}|B_L\rangle + e^{-\left(iM_H+\frac{1}{2}\Gamma_H\right)t}|B_H\rangle\right] \tag{3.56}$$

$$|\overline{B}^0(t)\rangle = \frac{1}{2q}\left[e^{-\left(iM_L+\frac{1}{2}\Gamma_L\right)t}|B_L\rangle - e^{-\left(iM_H+\frac{1}{2}\Gamma_H\right)t}|B_H\rangle\right]. \tag{3.57}$$

Re-writing 3.56 in terms of $\mathcal{CP}$ eigenstates we arrive at:

$$|B^0(t)\rangle = \frac{1}{2p}\left[e^{-\left(iM_L+\frac{1}{2}\Gamma_L\right)t}\left(p|B^0\rangle + q|\overline{B}^0\rangle\right) + e^{-\left(iM_H+\frac{1}{2}\Gamma_H\right)t}\left(p|B^0\rangle - q|\overline{B}^0\rangle\right)\right], \tag{3.58}$$

with a similar expression for $|\overline{B}^0(t)\rangle$. Collecting terms leaves:

$$|B^0(t)\rangle = g_+(t)|B^0\rangle + \frac{q}{p}g_-(t)|\overline{B}^0\rangle, \tag{3.59}$$

$$|\overline{B}^0(t)\rangle = \frac{p}{q}g_-(t)|B^0\rangle + g_+(t)|\overline{B}^0\rangle, \tag{3.60}$$

where $g_{\pm}(t)$ is given by:

$$g_{\pm}(t) = \frac{1}{2}\left[e^{-\left(iM_L+\frac{1}{2}\Gamma_L\right)t} \pm e^{-\left(iM_H+\frac{1}{2}\Gamma_H\right)t}\right]. \tag{3.61}$$

Equation 3.61 can be re-written as:

$$g_{+}(t) = e^{-\frac{1}{2}mt}e^{-\frac{1}{2}\Gamma t}\left[\cos\frac{\Delta mt}{2}\cosh\frac{\Delta\Gamma t}{4} - i\sin\frac{\Delta mt}{2}\sinh\frac{\Delta\Gamma t}{4}\right], \tag{3.62}$$

$$g_{-}(t) = e^{-\frac{1}{2}mt}e^{-\frac{1}{2}\Gamma t}\left[-\cos\frac{\Delta mt}{2}\sinh\frac{\Delta\Gamma t}{4} + i\sin\frac{\Delta mt}{2}\cosh\frac{\Delta\Gamma t}{4}\right], \tag{3.63}$$

where:

$$m = \frac{M_H + M_L}{2}, \tag{3.64}$$

$$\Gamma = \frac{\Gamma_H + \Gamma_L}{2}, \tag{3.65}$$

and Δm and $\Delta\Gamma$ are defined in equation 3.35.

3.5.5 Decay Rates to a State f

The time-dependent decay rate, $\Gamma(\mathrm{B}^0(t) \to f)$, of an initially tagged B^0 to a final state, f, is defined as:

$$\Gamma(\mathrm{B}^0(t) \to f) = \frac{1}{N_B}\frac{dN(\mathrm{B}^0(t) \to f)}{dt} \tag{3.66}$$

where $dN(\mathrm{B}^0(t) \to f)$ is the number of decays of mesons tagged as B^0 at $t = 0$ into the state f in the period t to $t + dt$ and N_B is the total number of B^0 mesons produced at $t = 0$. In terms of decay probabilities we have:

$$\Gamma(\mathrm{B}^0 \to f) = \mathcal{N}_f\left|\langle f|\mathrm{B}^0(t)\rangle\right|^2 \tag{3.67}$$

and

$$\Gamma(\overline{\mathrm{B}}^0 \to f) = \mathcal{N}_f\left|\langle f|\overline{\mathrm{B}}^0(t)\rangle\right|^2, \tag{3.68}$$

where $\mathcal{N}_f$ is a time-independent normalisation factor which depends on the kinematics of the decay.

It is useful to define, $A_f, \bar{A}_f$ and λ_f:

$$A_f = \langle f|\mathrm{B}^0\rangle, \quad \bar{A}_f = \langle f|\overline{\mathrm{B}}^0\rangle, \tag{3.69}$$

$$\lambda_f = \frac{q}{p}\frac{\bar{A}_f}{A_f}. \tag{3.70}$$

We now have:

$$\begin{aligned}\Gamma(\mathrm{B}^0 \to f) = \mathcal{N}_f \left|A_f\right|^2 e^{-\Gamma t} \Bigg[& \frac{1+|\lambda_f|^2}{2}\cosh\frac{\Delta\Gamma t}{2} + \frac{1-|\lambda_f|^2}{2}\cos(\Delta m t) \\ & -\mathsf{Re}\lambda_f \sinh\frac{\Delta\Gamma t}{2} - \mathsf{Im}\lambda_f \sin(\Delta m t)\Bigg],\end{aligned} \tag{3.71}$$

$$\begin{aligned}\Gamma(\overline{\mathrm{B}}^0 \to f) = \mathcal{N}_f \left|A_f\right|^2 (1+a_{fs})\, e^{-\Gamma t} \Bigg[& \frac{1+|\lambda_f|^2}{2}\cosh\frac{\Delta\Gamma t}{2} - \frac{1-|\lambda_f|^2}{2}\cos(\Delta m t) \\ & -\mathsf{Re}\lambda_f \sinh\frac{\Delta\Gamma t}{2} + \mathsf{Im}\lambda_f \sin(\Delta m t)\Bigg],\end{aligned} \tag{3.72}$$

where we have used $|p/q|^2 = (1 + a_{fs})$.

Decay rates to the $\mathcal{CP}$-conjugate state, $|\bar{f}\rangle = \mathcal{CP}|f\rangle$, are developed in a similar manner. We have:

$$\begin{aligned}\Gamma(\mathrm{B}^0 \to \bar{f}) = \mathcal{N}_f \left|\bar{A}_{\bar{f}}\right|^2 (1-a_{fs})\, e^{-\Gamma t} \Bigg[& \frac{1+|\lambda_{\bar{f}}|^{-2}}{2}\cosh\frac{\Delta\Gamma t}{2} - \frac{1-|\lambda_{\bar{f}}|^{-2}}{2}\cos(\Delta m t) \\ & -\mathsf{Re}\frac{1}{\lambda_{\bar{f}}} \sinh\frac{\Delta\Gamma t}{2} + \mathsf{Im}\frac{1}{\lambda_{\bar{f}}} \sin(\Delta m t)\Bigg],\end{aligned} \tag{3.73}$$

$$\begin{aligned}\Gamma(\overline{\mathrm{B}}^0 \to \bar{f}) = \mathcal{N}_f \left|\bar{A}_{\bar{f}}\right|^2 e^{-\Gamma t} \Bigg[& \frac{1+|\lambda_{\bar{f}}|^{-2}}{2}\cosh\frac{\Delta\Gamma t}{2} + \frac{1-|\lambda_{\bar{f}}|^{-2}}{2}\cos(\Delta m t) \\ & -\mathsf{Re}\frac{1}{\lambda_{\bar{f}}} \sinh\frac{\Delta\Gamma t}{2} - \mathsf{Im}\frac{1}{\lambda_{\bar{f}}} \sin(\Delta m t)\Bigg].\end{aligned} \tag{3.74}$$

3.6 Three Types of $\mathcal{CP}$ Violation

There are three $\mathcal{CP}$-violating physical observables which are phase-convention independent. They are:

$$\left|\frac{\bar{A}_{\bar{f}}}{A_f}\right|, \quad \left|\frac{q}{p}\right|, \quad \lambda_f = \frac{q}{p}\frac{\bar{A}_f}{A_f}. \tag{3.75}$$

Should the first or second observables assume a value other then 1 or $\mathsf{Im}(\lambda_f) \neq 0$, then that decay will violate $\mathcal{CP}$.

$\mathcal{CP}$-violating processes can be classed depending on which of the observables listed in 3.75 are relevant:

1. Direct $\mathcal{CP}$ violation.

2. $\mathcal{CP}$ violation in mixing.

3. $\mathcal{CP}$ violation in interference between decays with and without mixing.

3.6.1 Direct $\mathcal{CP}$ Violation

Consider a decay $\mathrm{B} \to f$; the amplitudes for the decay and its $\mathcal{CP}$ conjugate are:

$$A_f = \langle f|\mathrm{B}\rangle, \quad \bar{A}_{\bar{f}} = \langle \bar{f}|\overline{\mathrm{B}}\rangle. \tag{3.76}$$

The amplitudes can be written as a sum of all possible contributions:

$$A_f = \sum_k A_k e^{i(\delta_k+\phi_k)}, \quad \bar{A}_{\bar{f}} = \sum_k A_k e^{i(\delta_k-\phi_k)}, \tag{3.77}$$

where each contribution has magnitude, A_k, strong phase, δ_k, and weak phase, ϕ_k. Weak phases enter into the amplitudes through the CKM matrix and change sign under $\mathcal{CP}$. Another phase can be introduced via the absorptive parts of the decay amplitudes. These additional phases are due to on-shell intermediate states which proceed through strong interactions into the final state. There is no experimental evidence that strong interactions violate $\mathcal{CP}$ [32], therefore the strong phases remain unchanged under $\mathcal{CP}$.

If we consider a simple case where the amplitudes are given by only two contributions, the amplitude is:

$$A = A_1 e^{i\phi_1} e^{i\delta_1} + A_2 e^{i\phi_2} e^{i\delta_2}, \tag{3.78}$$

and the $\mathcal{CP}$ conjugate of the amplitude is:

$$\bar{A} = A_1 e^{-i\phi_1} e^{i\delta_1} + A_2 e^{-i\phi_2} e^{i\delta_2}. \tag{3.79}$$

The difference in rates is given by:

$$|A|^2 - \left|\bar{A}\right|^2 = 2A_1A_2\sin\left(\phi_1 - \phi_2\right)\sin\left(\delta_1 - \delta_2\right). \tag{3.80}$$

Inspection of 3.80 shows that both the strong and weak phases of the two terms in the amplitude must be different if the decay in question is to exhibit a $\mathcal{CP}$-violating rate difference. This is called direct $\mathcal{CP}$ violation and is characterised by:

$$\left|\frac{\bar{A}}{A}\right| \neq 1. \tag{3.81}$$

Note that the weak phases can be altered by redefining the phases of the quark fields. Any two terms which contribute to the same rate must correspond to the same set of fields of the external particles. The phase convention adopted will therefore change both terms in the same way and only phase differences are convention-independent and have any physical meaning.

3.6.2 $\mathcal{CP}$ Violation in Mixing

Mixing occurs in pairs of neutral pseudoscalar mesons such as $\mathrm{K}^0\,\overline{\mathrm{K}}^0$, $\mathrm{D}^0\,\overline{\mathrm{D}}^0$, $\mathrm{B}^0\,\overline{\mathrm{B}}^0$ and $\mathrm{B}^0_\mathrm{s}\,\overline{\mathrm{B}}^0_\mathrm{s}$. From equation 3.39 we can see that:

$$\left|\frac{q}{p}\right|^2 = \left|\frac{M^*_{12} - \frac{i}{2}\Gamma^*_{12}}{M_{12} - \frac{i}{2}\Gamma_{12}}\right|. \tag{3.82}$$

If $\mathcal{CP}$ were conserved, the relative phase between M_{12} and Γ_{12} would vanish and $|q/p| = 1$. Therefore, if $|q/p| \neq 1$ then $\mathcal{CP}$ is violated. This type of $\mathcal{CP}$ violation is a direct result of the mass and $\mathcal{CP}$ eigenstates being different.

A method to determine $a_{fs}/2$, which represents the deviation of $|p/q|$ from unity, is discussed in chapter 6.

3.6.3 $\mathcal{CP}$ Violation in Interference Between Mixing and Decay

$\mathcal{CP}$ violation in neutral pseudoscalar mesons can arise from the interference between mixing and decay amplitudes, even when $\left|\bar{A}/A\right|$ and $|q/p| = 1$. It requires that the final

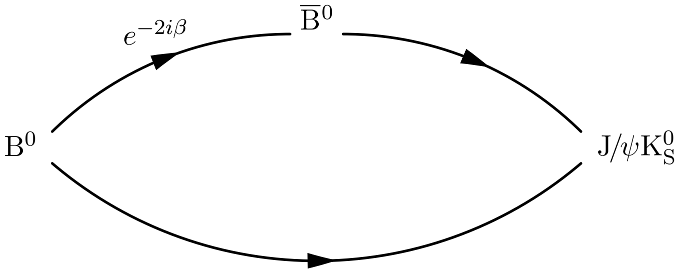

Figure 3.4: How the phase 2β is introduced into $\mathrm{B}^0 \to \mathrm{J}/\psi\mathrm{K}^0_\mathrm{S}$ decays.

state is accessible to both states. Consider decays from state B^0 and state $\overline{\mathrm{B}}^0$. They have amplitudes:

$$A_f \quad \text{and} \quad \bar{A}_f = \eta_f \bar{A}_{\bar{f}}, \tag{3.83}$$

where $\mathcal{CP}|f\rangle = |\bar{f}\rangle = \eta_f|f\rangle$ and $\eta_f = \pm 1$.

A particle which is a pure B^0 state at $t = 0$ can either decay directly to state f or by mixing first. The two paths interfere to produce a time-dependent asymmetry between the rates $\Gamma(\mathrm{B}^0 \to f)$ and $\Gamma(\overline{\mathrm{B}}^0 \to f)$, namely:

$$a_f(t) = \frac{\Gamma\left(\overline{\mathrm{B}}^0(t) \to f\right) - \Gamma\left(\mathrm{B}^0(t) \to f\right)}{\Gamma\left(\overline{\mathrm{B}}^0(t) \to f\right) + \Gamma\left(\mathrm{B}^0(t) \to f\right)}. \tag{3.84}$$

Defining:

$$\lambda_{f_{\mathcal{CP}}} = \frac{q}{p}\frac{\bar{A}_{f_{\mathcal{CP}}}}{A_{f_{\mathcal{CP}}}} = \eta_{f_{\mathcal{CP}}}\frac{q}{p}\frac{\bar{A}_{\bar{f}_{\mathcal{CP}}}}{A_{f_{\mathcal{CP}}}}, \tag{3.85}$$

the asymmetry is

$$a_f(t) = -\frac{\left(1 - |\lambda_f|^2\right)\cos\left(\Delta m t\right) - 2\mathsf{Im}\lambda_f \sin\left(\Delta m t\right)}{\left(1 + |\lambda_f|^2\right)\cosh\left(\Delta\Gamma t/2\right) - 2\mathsf{Re}\lambda_f \sinh\left(\Delta\Gamma t/2\right)} + \mathcal{O}(a) \tag{3.86}$$

where $a = \mathsf{Im}(\Gamma_{12}/M_{12})$. The asymmetry is non-zero if any $\mathcal{CP}$ violation occurs.

An example of this type of $\mathcal{CP}$ violation is in the "gold-plated" decay $\mathrm{B}^0 \to \mathrm{J}/\psi\mathrm{K}^0_\mathrm{S}$. Here $\Delta\Gamma \to 0$ and $|\lambda_f| = 1$ and the asymmetry simplifies to:

$$a_f(t) = \mathsf{Im}\lambda_f \sin\left(\Delta m t\right). \tag{3.87}$$

In this case, $\lambda_f = \lambda_{\mathrm{J}/\psi\mathrm{K}^0_\mathrm{S}}$ and is given by:

$$\lambda_{\mathrm{J}/\psi\mathrm{K}^0_\mathrm{S}} = -\left(\frac{V^*_{tb}V_{td}}{V_{tb}V^*_{td}}\right)\left(\frac{V^*_{cb}V_{cs}}{V_{cb}V^*_{cs}}\right)\left(\frac{V^*_{cs}V_{cd}}{V_{cs}V^*_{cd}}\right) = -e^{-2i\beta}. \tag{3.88}$$

Hence, a measurement which is sensitive to the phase difference between the different decay paths measures $\sin 2\beta$ directly. Figure 3.4 shows the introduction of the weak phase -2β into the decay diagrammatically.

3.7 Current Status of CKM Parameters

3.7.1 Magnitudes of CKM Matrix Elements

The magnitudes of the CKM matrix elements have been measured directly. All values are taken from [34]:

1. $|V_{ud}| = 0.97377 \pm 0.00027$ from lifetime measurements of superallowed $0^+ \to 0^+$ nuclear β decays.
2. $|V_{us}| = 0.2257 \pm 0.0021$ from the kaon semileptonic decay rate.
3. $|V_{cd}| = 0.230 \pm 0.011$ from charm production by neutrino and antineutrino beams off valence d-quarks.
4. $|V_{cs}| = 0.957 \pm 0.017 \pm 0.093$ from semileptonic decays of D mesons.
5. $|V_{cb}| = (41.6 \pm 0.6) \times 10^{-3}$ from semileptonic B meson decays to charm.
6. $|V_{ub}| = (4.31 \pm 0.30) \times 10^{-3}$ from semileptonic B meson decays.
7. $|V_{td}| = (7.4 \pm 0.8) \times 10^{-3}$ from B^0_d mixing assuming $|V_{tb}| = 1$.
8. $|V_{ts}| = (40.6 \pm 2.7) \times 10^{-3}$ from t-quark penguin contributions to $B \to X_s\gamma$ assuming $V_{cb}V^*_{cs} \approx -V_{tb}V^*_{ts}$.
9. $|V_{tb}| > 0.78$ (95% CL lower limit) from semileptonic top decays.

From the measurement of B^0_d and B^0_s oscillation periods, the mass differences in each system are found to be:

$$\Delta m_d = 0.507 \pm 0.004\,\mathrm{ps}^{-1} \tag{3.89}$$

$$\Delta m_s = 17.31^{+0.33}_{-0.18} \pm 0.07\,\mathrm{ps}^{-1}, \tag{3.90}$$

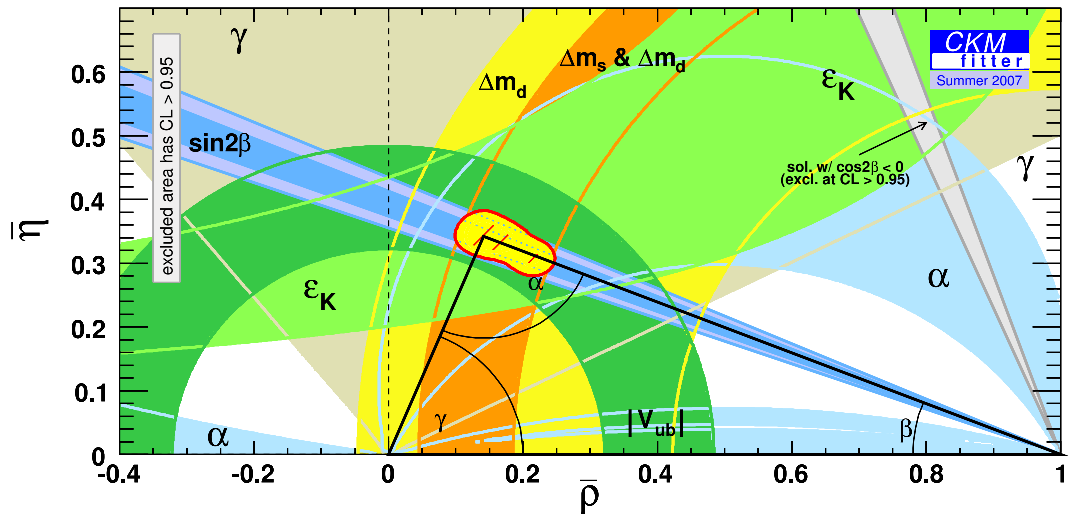

Figure 3.5: The global CKM fit to Summer 2007 data as provided by the CKM Fitter group [2].

which leads to the following constraint [35]:

$$\left|\frac{V_{td}}{V_{ts}}\right| = 0.208^{+0.001}_{-0.002}(\text{exp.})^{-0.008}_{-0.006}(\text{theo.}). \tag{3.91}$$

3.7.2 Global CKM Fits

The CKM triangle allows the measurements of the magnitudes of the CKM matrix elements to be combined with results from $\mathcal{CP}$ violation experiments. Global fits of the CKM triangle are performed by two groups, the CKM Fitter group and the UTfit group. The two groups differ in their fit strategy and choice of fit parameters. Both fit methods currently give consistent results for the upper vertex and internal angles of the CKM triangle (Table 3.1). Further details of the choice of fit parameters, fit methods and results can be found in [2] and [3].

A graphical representation of the constraints as of Summer 2007 as determined by the CKM Fitter group is given in figure 3.5. Both the real and imaginary axes have been rescaled, in this basis the apex of the triangle is located at:

$$(\bar{\rho}, \bar{\eta}) = \left(1 - \frac{\lambda^2}{2}\right)(\rho, \eta)\,. \tag{3.92}$$

Parameter	CKM Fitter	UTfit
$\bar{\rho}$	$0.189^{+0.088}_{-0.070}$	0.197 ± 0.031
$\bar{\eta}$	$0.358^{+0.046}_{-0.042}$	0.351 ± 0.020
$\alpha[^\circ]$	94^{+12}_{-10}	95.5 ± 4.8
$\beta[^\circ]$	$23.8^{+2.1}_{-2.0}$	23.6 ± 1.0
$\gamma[^\circ]$	62^{+10}_{-12}	60.6 ± 4.7

Table 3.1: Comparison of the fitted values of the upper vertex ($\bar{\rho} + i\bar{\eta}$) and the three internal angles of the CKM triangle as given by the CKM Fitter group [2] and the UTfit group [3].

The constraints from the CKM angles, the mass differences of the neutral b-mesons, ϵ_K and $|V_{ub}|$ are displayed. All the parameters have been previously introduced with the exception of ϵ_K which is the $\mathcal{CP}$-violating parameter of the kaon system [36]. The most stringent constraint in the fit is the precise measurement of $\sin 2\beta$. The value used in the fit is the 2004 Winter world average as provided by the Heavy Flavour Averaging Group (HFAG):

$$\sin 2\beta = 0.739 \pm 0.048. \tag{3.93}$$

The situation has improved in recent years and the current world average is [37]:

$$\sin 2\beta = 0.675 \pm 0.026. \tag{3.94}$$

3.8 Summary

$\mathcal{CP}$ violation in the Standard Model is governed by the CKM matrix which describes the relationship between the $SU(2)$ partners of the up-type quarks and the mass eigenstates of the down-type quarks. The CKM matrix is defined by three real parameters and a single $\mathcal{CP}$-violating complex parameter.

The B-factories and the Tevatron have advanced our knowledge of the CKM elements significantly however there is no evidence of new physics yet. The precision measurements possible at LHCb are required to fully explore the B-sector.

The expressions describing the mixing and time-evolution of neutral B-mesons are presented. A method to determine the $\mathcal{CP}$ violation in mixing parameter, a_{fs}, is introduced in chapter 6.

Chapter 4

Tuning Minimum Bias Events at LHCb

4.1 Introduction

Pythia [38] is a widely used Monte Carlo event generator which models a large number of physics processes and interactions. It is the main event generator used by the LHCb collaboration to simulate *pp* collisions.

Many of the B-mesons produced in primary collisions are expected to be orbitally excited $L = 1$ (B^{**}) states according to measurements performed at LEP [39, 40, 41] and the Tevatron [42]. The excited states decay strongly via the emission of a charged hadron which allows the initial flavour of the B-meson to be determined. This method of flavour identification is termed Same Side Tagging (SST).

The inclusion of excited states affects the average multiplicity of minimum bias events[1] since some settings are shared between heavy- and light-flavoured mesons in the Pythia hadronisation model. The track multiplicity distribution as well as the transverse momentum distribution of minimum bias events affect the performances of the low-level triggers and the detector occupancy of the LHCb experiment. It is therefore

---

[1] Minimum bias events are usually attributed to non-single-diffractive events but the exact experimental definition depends on the trigger used.

Parameter	Description	Default Value	LHCb Value
PARJ(1)	Baryon production	0.10	0.10
PARJ(2)	Strangeness production	0.30	0.30
PARJ(11)	P(light meson has spin 1)	0.50	0.50
PARJ(12)	P(strange meson has spin 1)	0.60	0.60
PARJ(13)	P(heavy meson has spin 1) (b,c)	0.75	0.75
PARJ(14)	$P(S=0,L=1,J=1)$	0.0	0.162
PARJ(15)	$P(S=1,L=1,J=0)$	0.0	0.018
PARJ(16)	$P(S=1,L=1,J=1)$	0.0	0.054
PARJ(17)	$P(S=1,L=1,J=2)$	0.0	0.09

Table 4.1: Spin and fragmentation parameters related to meson production in Pythia.

important to simulate both B-meson production and minimum bias events as accurately as possible.

4.2 B^{**} Settings

The parameters affecting the production of B-mesons are listed in table 4.1. The parameter set attempts to reproduce the measured B-meson fractions [43] and LEP B^{**} spin counting measurements in the produced B-hadrons. The specific B-hadron fractions and spin state ratios are given in 4.1 and 4.2.

$$f_{\mathrm{B}^0} : f_{\mathrm{B}^+} : f_{\mathrm{B}^0_s} : f_{\text{B-Baryon}} = 4 : 4 : 1 : 1, \tag{4.1}$$

$$f_{B_0^*} : f_{B_1} : f_{B_1^*} : f_{B_2^*} = 1 : 3 : 3 : 5, \tag{4.2}$$

where f_{type} represents the observed production fraction of B-hadrons of that particular particle type and the angular momentum properties of the spin-states are given in table 4.2.

The charged multiplicity of minimum bias events is increased by the inclusion of the excited states since the parameters which determine meson spin-state production affect both heavy and light mesons equally.

State	B_0	B_1^*	B_1	B_2^*
$J_{j_q}^P$	$0^+_{1/2}$	$1^+_{1/2}$	$1^+_{3/2}$	$2^+_{3/2}$

Table 4.2: Angular momentum properties of the four lowest $L = 1$ B-meson states. J is the meson total angular momentum, j_q is the total angular momentum of the light quark and P is the parity of the state.

$\sqrt{s}\,(\mathrm{GeV})$	Experiment	$< dN_{ch}/d\eta >_{\|\eta\|<0.25}$
53	UA5	1.96 ± 0.10
200	UA5	2.48 ± 0.07
546	UA5	3.05 ± 0.03
650	CDF	3.18 ± 0.15
900	UA5	3.48 ± 0.07
1800	CDF	3.95 ± 0.15

Table 4.3: Differential charged multiplicities for non-single-diffractive events measured in the central rapidity region by the UA5 [4] and CDF [5] experiments. The errors are calculated by linearly adding the statistical and systematic errors where possible.

4.3 Energy Dependence of Minimum Bias Multiplicity

Measurements of charged multiplicities, performed at lower energies up to 1.8 TeV, are available from the UA5 [4] and CDF [5] experiments. Table 4.3 contains a summary of the measurements in the central rapidity region.

The energy dependence of the mean charged multiplicity of minimum bias events at hadron colliders is phenomenologically well described by a quadratic logarithmic form [44]:

$$< dN_{ch}/d\eta >_{|\eta|<0.25} = A\,(\ln s)^2 + B \ln s + C, \tag{4.3}$$

where $< dN_{ch}/d\eta >_{|\eta|<0.25}$ is the mean charged multiplicity measured in the central rapidity region. Fitting equation 4.3 to the UA5 and CDF measurements one finds:

$$\begin{aligned} A &= 0.023 \pm 0.008, \\ B &= 0.24 \pm 0.18, \\ C &= 2.42 \pm 0.98. \end{aligned} \tag{4.4}$$

Extrapolating to LHC energies, one obtains a phenomenological prediction for the charged particle density in the central rapidity region of:

$$< dN_{ch}/d\eta >^{\text{LHC}}_{|\eta|<0.25} = 6.27 \pm 0.50. \tag{4.5}$$

4.4 Pythia Multiple Interaction Model

The workings of Pythia's multiple interaction models are fully described in [38]. However, it is useful to give a summary of the basic model and the main parameter which dictates the average multiplicity of an event.

Multiple interactions in hadron collisions can be separated into two categories:

1. A parton from one beam can interact several times with the partons from the other beam.
2. Several partons from both beams interact in separate 2 → 2 interactions.

Due to the increased combinatorics, only the second category is implemented in Pythia.

The basic premise of the Pythia multiple interaction model is to assume that the total rate of hard interactions, as a function of the transverse momentum scale, $p_\perp$, is given by purturbative QCD and then extend the framework into the low-$p_\perp$ region. Since the hard scattering cross section diverges as $p_\perp \to 0$ some cutoff or damping has to be introduced. The hard scattering cross section is given by:

$$\sigma_{\text{hard}}\left(p_{\perp\text{Min}}\right) = \int_{p^2_{\perp\text{Min}}}^{s/4} \frac{\mathrm{d}\sigma}{\mathrm{d}p^2_\perp} dp^2_\perp \tag{4.6}$$

where $p_{\perp\text{Min}}$ represents the scale of the cutoff.

The effective cutoff can be motivated by noting that incoming hadrons are colour neutral. An exchanged gluon with small $p_\perp$ has a large transverse wavefunction and is therefore unable to resolve individual colour charges and so experiences a smaller effective coupling.

The energy dependence of $p_{\perp\mathrm{Min}}$ is assumed to increase in the same way as the total cross section [45], i.e., to some power, $\epsilon \approx 0.08$:

$$p_{\perp\mathrm{Min}}(s) = Xs^{\epsilon}. \tag{4.7}$$

In terms of the default Pythia parameters, the energy dependence is:

$$\begin{aligned} p_{\perp\mathrm{Min}}(s) =& \mathrm{PARP}(81)\left(\frac{\sqrt{s}}{\mathrm{PARP}(89)}\right)^{2\times\mathrm{PARP}(90)}, & (4.8)\\ =& (1.9\,\mathrm{GeV})\left(\frac{s}{1800\,\mathrm{GeV}^2}\right)^{0.16}. & (4.9)\end{aligned}$$

The parameters are chosen such that the default settings reproduce the multiplicities observed at UA5 for centre of mass energies in the range 200 to 900 GeV [4]. The parameters are sensitive to changes in the hadronic matter distribution [38] and the parton distributions [46] used in the model.

Charged multiplicities have a strong dependence on $p_{\perp_{\mathrm{Min}}}$. Lowering $p_{\perp\mathrm{Min}}$ increases the average number of multiple interactions in an event and therefore increases the average charged multiplicity.

4.4.1 Tuning Motivation

The addition of orbitally excited meson states increases the multiplicity produced by Pythia at all energies. Since the output of Pythia no longer matches the multiplicities measured by UA5, the $p_{\perp\mathrm{Min}}$ parameter must be re-tuned to reproduce the measured data. The tuning method is described in section 4.5.

4.5 Fit Method and Results

We may choose one of two methods to re-tune the average charged multiplicity of minimum bias events:

1. Adjust the $p_{\perp \mathrm{Min}}$ parameter such that the 14 TeV phenomenological prediction is realised.

2. Tune the $p_{\perp \mathrm{Min}}$ parameter to charged multiplicity data from established hadron collider experiments and then extrapolate $p_{\perp \mathrm{Min}}$ to 14 TeV using a parameterisation in the form of equation 4.7.

The latter option follows more closely the manner in which the default values of the relevant parameters in Pythia v6.226 were determined and forms the basis of the tuning method described.

Pythia v6.226 was used to generate non-single-diffractive events at the various centre of mass energies ($\sqrt{s} = 53$, 200, 546, 630, 900 and 1800 GeV). The measured data is corrected for secondary decay tracks (mainly from $\mathrm{K^0_S}$ and Λ) and single-diffractive events. Accordingly, the $\mathrm{K^0_S}$, $\mathrm{K^0_L}$ and Λ particles were set as stable in addition to including the B^{**} settings.

$p_{\perp \mathrm{Min}}$ was varied over a suitable range at each energy such that the generated central charged multiplicities covered a minimum of ± two standard deviations of the charged multiplicities measured at UA5 and CDF. The difference between the produced charged multiplicity and the measured data, $\delta = \frac{1}{N_{ch}} \frac{dN_{ch}}{d\eta}|^{MC}_{\eta=0} - \frac{1}{N_{ch}} \frac{dN_{ch}}{d\eta}|^{data}_{\eta=0}$, is calculated and a linear fit performed using MINUIT [47].

The central multiplicity fits at the centre of mass energies listed in table 4.3 are illustrated in figures 4.1 to 4.3. The re-tuned value of $p_{\perp \mathrm{Min}}$ is obtained by inverting the equation of the fitted line. Sufficient events were generated such that the uncertainty on the fitted value of $p_{\perp \mathrm{Min}}$ is unaffected by Monte Carlo statistical errors. The fit results and tuned $p_{\perp \mathrm{Min}}$ values can be found in table 4.4.

To extrapolate $p_{\perp \mathrm{Min}}$ to LHC energy, a fit is performed (Fig. 4.4) using a form suggested by Pythia:

$$p_{\perp_{\mathrm{Min}}} = p^{LHC}_{\perp_{\mathrm{Min}}} \Big(\frac{\sqrt{s}}{14 \ \mathrm{TeV}} \Big)^{2\epsilon}. \tag{4.10}$$

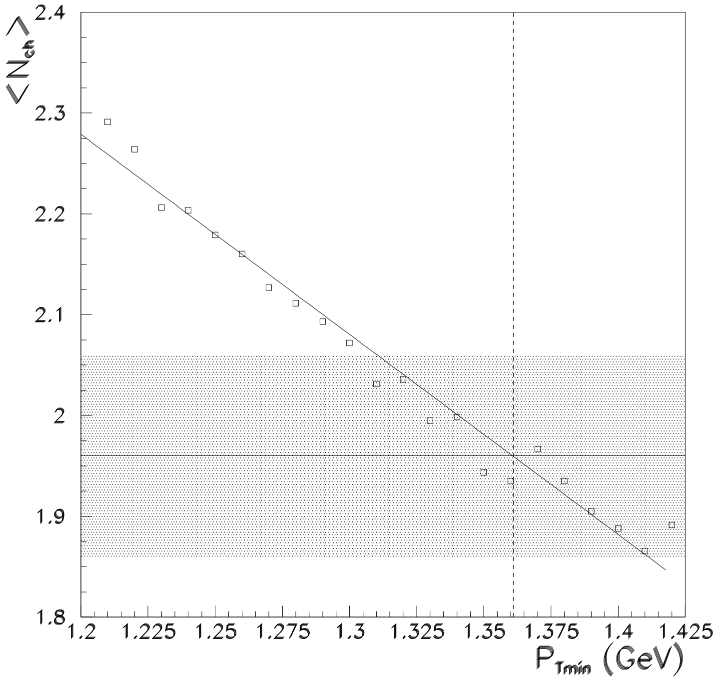

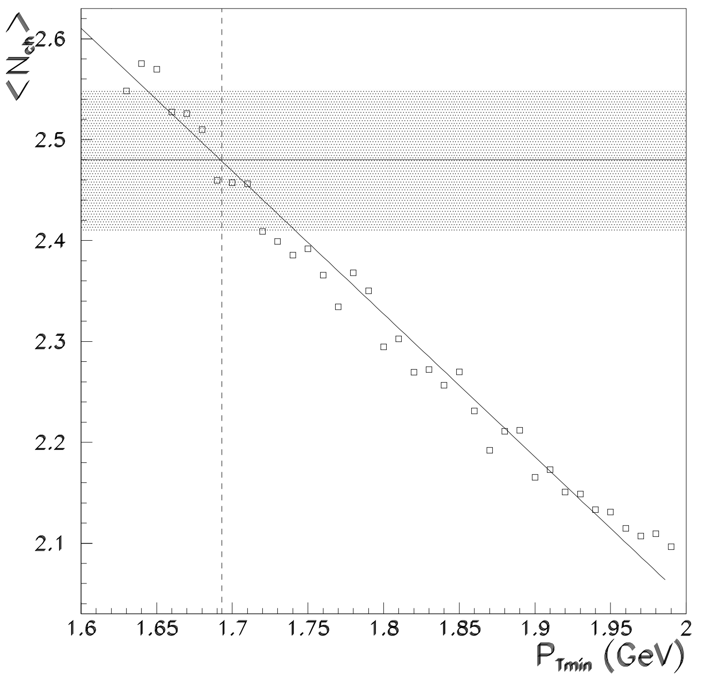

Figure 4.1: Generated charged multiplicity data at $\sqrt{s} = 53\,\mathrm{GeV}$ (upper) and $200\,\mathrm{GeV}$ (lower) with linear fits superimposed. Each point represents the average multiplicity generated by one million non-single-diffractive $p\overline{p}$ events. The optimum value of $p_{\perp\mathrm{Min}}$ is $1.36 \pm 0.148\,\mathrm{GeV}$ (upper) and $1.69 \pm 0.072\,\mathrm{GeV}$ (lower) respectively.

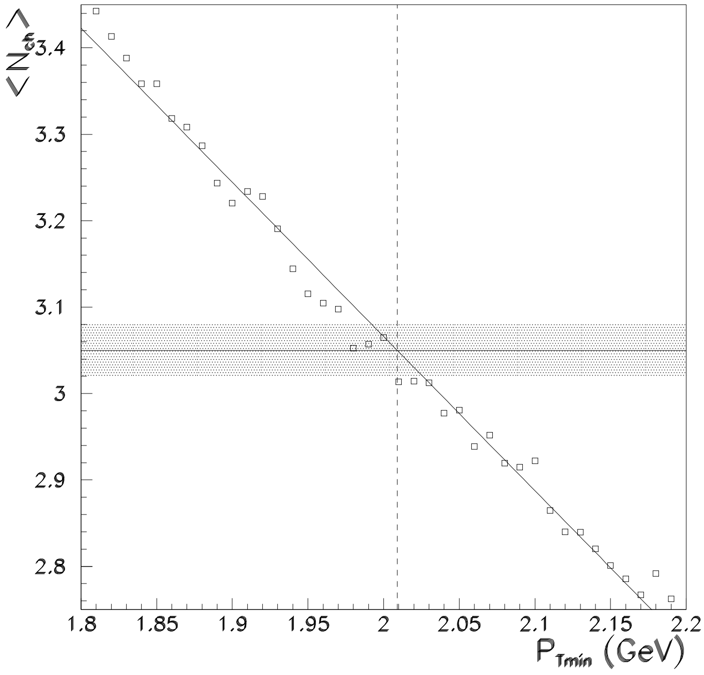

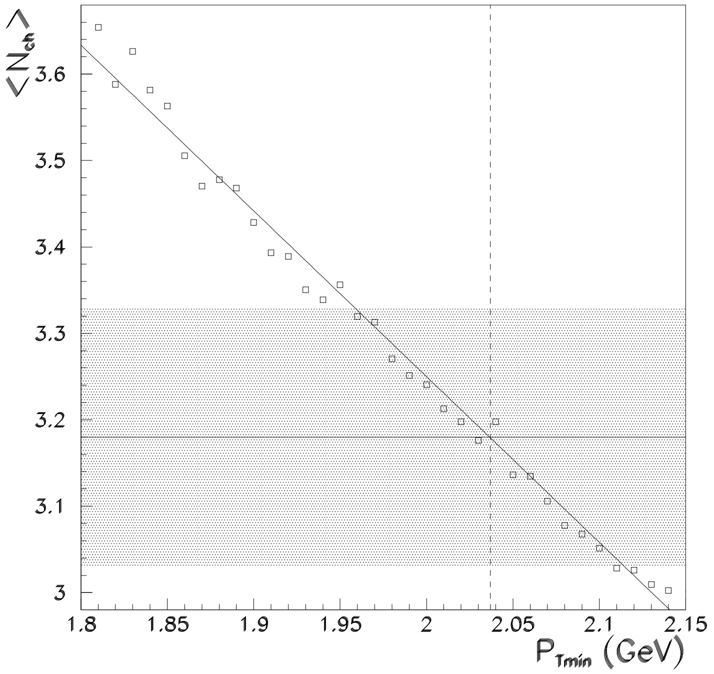

Figure 4.2: Generated charged multiplicity data at $\sqrt{s} = 546\,\mathrm{GeV}$ (upper) and $630\,\mathrm{GeV}$ (lower) with linear fits superimposed. Each point represents the average multiplicity generated by one million non-single-diffractive $p\overline{p}$ events. The width of the grey band represents the uncertainty on the measured data. The optimum value of $p_{\perp\mathrm{Min}}$ is $2.01 \pm 0.006\,\mathrm{GeV}$ (upper) and $2.04 \pm 0.142\,\mathrm{GeV}$ (lower) respectively.

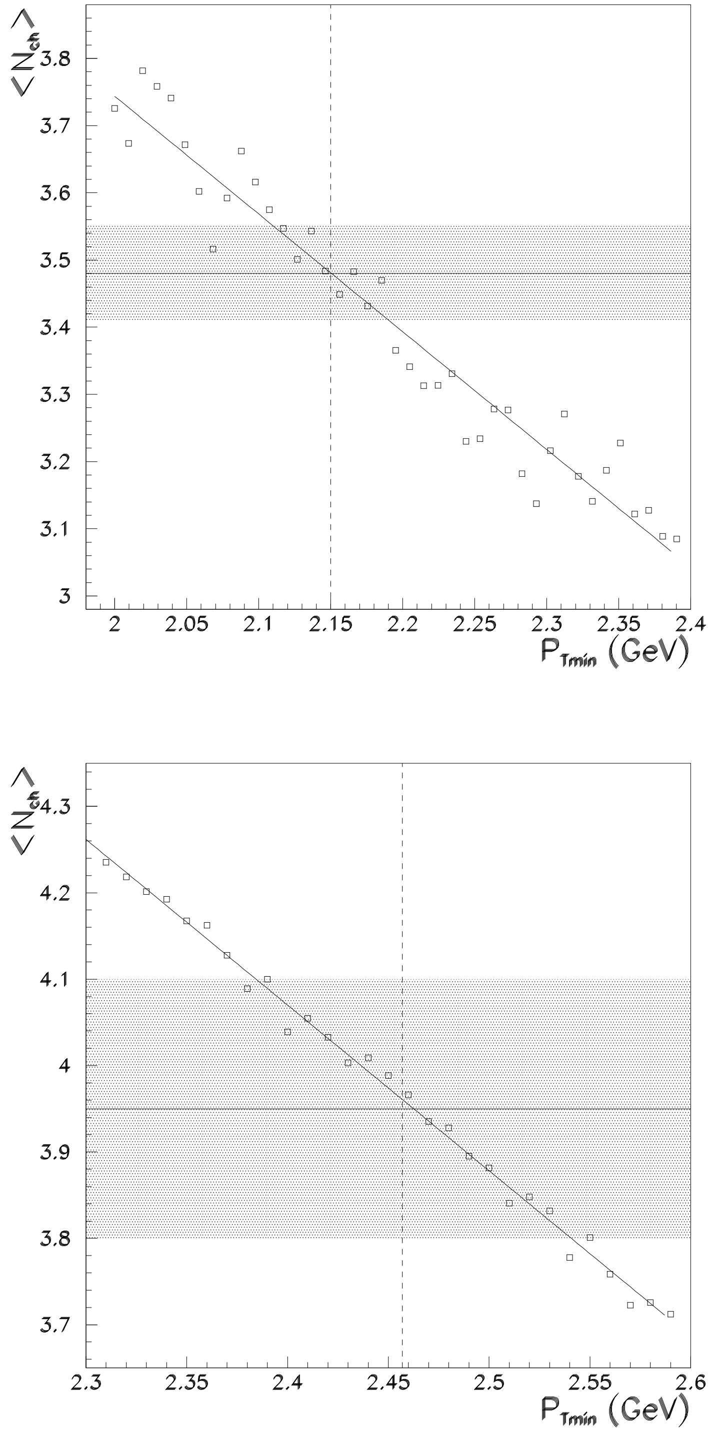

Figure 4.3: Generated charged multiplicity data at $\sqrt{s} = 900\,\text{GeV}$ (upper) and $1800\,\text{GeV}$ (lower) with linear fits superimposed. Each point represents the average multiplicity generated by one million non-single-diffractive $p\bar{p}$ events. The width of the grey band represents the uncertainty on the measured data. The optimum value of $p_{\perp\text{Min}}$ is $2.15 \pm 0.054\,\text{GeV}$ (upper) and $2.46 \pm 0.167\,\text{GeV}$ (lower) respectively.

$\sqrt{s}$ (GeV)	$p_{\perp\mathrm{Min}}$	$\sigma_{p_{\perp\mathrm{Min}}}$
53	1.36	0.148
200	1.69	0.072
546	2.01	0.006
630	2.04	0.142
900	2.15	0.054
1800	2.46	0.167

Table 4.4: Tuned values of $p_{\perp\mathrm{Min}}$ which reproduce the central charged multiplicities quoted in table 4.3 in non-single-diffractive events.

Parameter	Original	Tuned	Description
PARP(82)	3.45	3.39	Multiple interaction regularisation scale, $p_{\perp\mathrm{Min}}$
PARP(89)	14000.	14000.	Reference energy scale
PARP(90)	0.174	0.162	Power of $p_{\perp\mathrm{Min}}$ energy rescaling term, ϵ

Table 4.5: Comparison of the original and tuned LHCb multiple interaction settings.

Fitting equation 4.10 to the tuned $p_{\perp\mathrm{Min}}$ data gives:

$$p_{\perp\mathrm{Min}}^{LHC} = 3.39 \pm 0.16, \tag{4.11}$$

$$\text{with} \quad \epsilon = 0.081 \pm 0.007. \tag{4.12}$$

This produces a central charged multiplicity of:

$$\frac{1}{N_{ch}} \frac{dN_{ch}}{d\eta}|_{\eta \leq 0.25} = 6.37 \pm 0.52 \tag{4.13}$$

in minimum bias events at 14 TeV. The original $p_{\perp\mathrm{Min}}$ settings are compared to the tuned settings in table 4.5.

4.6 Effects of the Tuning on Minimum Bias Events at 14 TeV

Figures 4.5 to 4.8 show the charged particle rapidity, charged multiplicity, transverse momentum and maximum transverse momentum distributions for minimum bias events

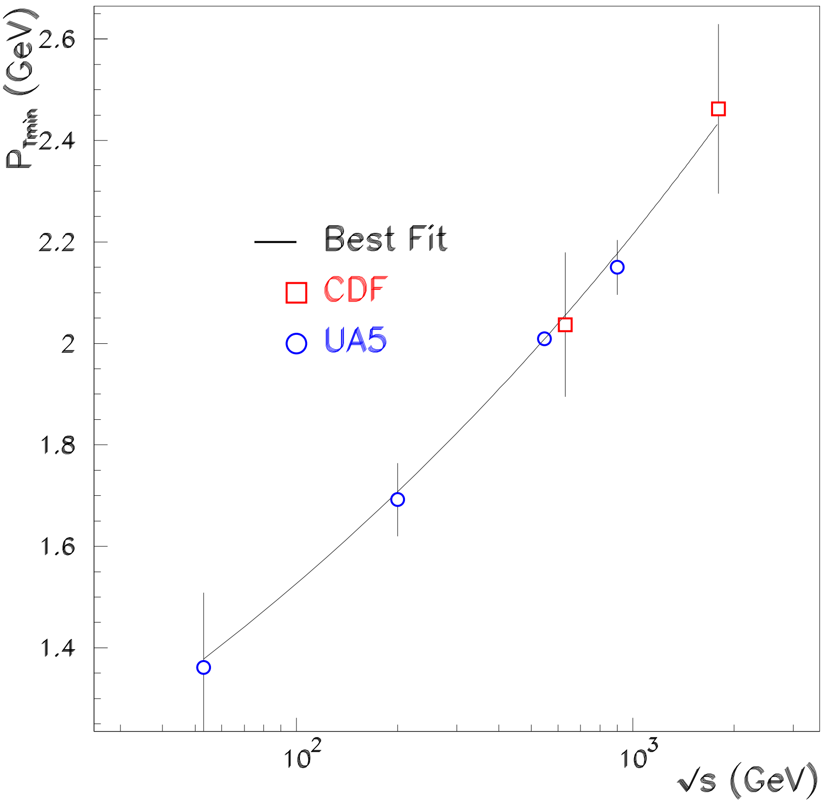

Figure 4.4: Tuned $p_{\perp \mathrm{Min}}$ data at various $\sqrt{s}$ superimposed with a fit to equation 4.10. The fit gives $P^{LHC}_{\perp \mathrm{Min}} = 3.39 \pm 0.16$ with $\epsilon = 0.081 \pm 0.007$.

created using the original LHCb settings and the tuned settings. Only charged stable particles which fall within the LHCb acceptance contribute to the distributions presented in figures 4.6 and 4.7. The shape of figure 4.7 can be understood as the majority of the low transverse-momentum particles fall outside the LHCb acceptance. The peak at zero in figure 4.8 is due to single-diffractive events.

The tuned settings produce an average central multiplicity of 6.37 ± 0.52 in 100 k minimum bias events. The result is compatible with the phenomenological prediction of 6.27 ± 0.50. The average event multiplicity within the LHCb acceptance was found to be 18.81 ± 0.06 using the tuned settings and 17.54 ± 0.06 using the original settings. The increased multiplicity has the effect of lowering the average transverse momentum of particles within the LHCb acceptance (Fig. 4.7). The maximum transverse momentum distribution remains unaffected because varying $p_{\perp_{\mathrm{Min}}}$ has no effect on the initial hard scatter of an event.

The tuned settings were adopted by the LHCb collaboration and used in Data Challenge 2004 (DC'04) for production. The parameters used in the tune can be found in appendix A.

4.7 Conclusions

Orbitally excited meson states were introduced to the LHCb generator settings. An increase in minimum bias event multiplicity was observed at the centre of mass energies used to determine the value of the Pythia parameter, $p_{\perp_{\mathrm{Min}}}$.

The $p_{\perp\mathrm{Min}}$ parameter of Pythia v6.226 was re-tuned using multiplicity data from the UA5 and CDF experiments at various centre of mass energies. The central multiplicity values measured at CDF and UA5 are accurately reproduced using the re-tuned values of $p_{\perp\mathrm{Min}}$ at several centre of mass energies. A fit to the obtained values was performed using the energy dependence of $p_{\perp_{\mathrm{Min}}}$ suggested by Pythia. An extrapolation of $p_{\perp\mathrm{Min}}$ to LHC energies gives $P^{LHC}_{\perp_{\mathrm{Min}}} = 3.39 \pm 0.16$ with $\epsilon = 0.081 \pm 0.007$ and a corresponding central multiplicity of $\langle n_{ch} \rangle |_{\eta=0} = 6.37 \pm 0.52$ in minimum bias events. The tuned central multiplicity is consistent with the phenomenological extrapolation of 6.27 ± 0.50.

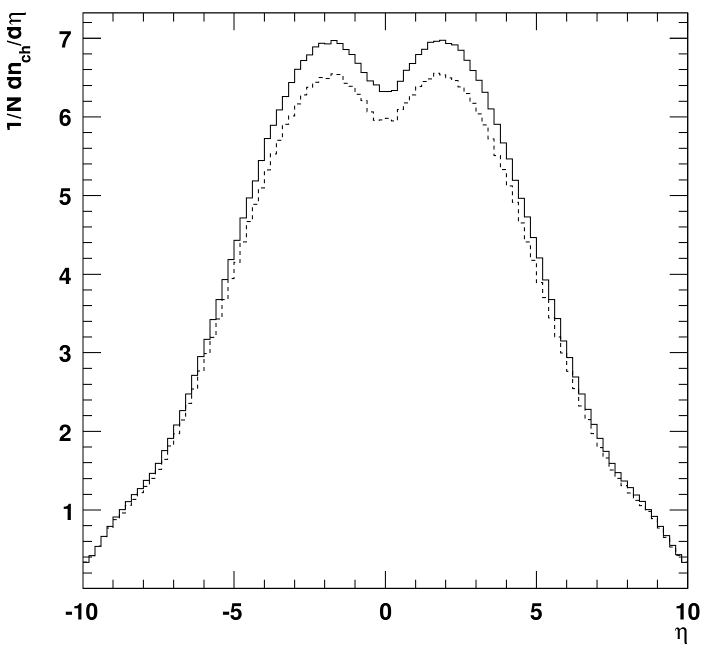

Figure 4.5: Multiplicity distribution of 100,000 minimum bias events generated with Pythia v6.226 at 14 TeV using the original LHCb settings (dashed line) and the tuned settings (solid line) normalised to the number of events. The tuned settings produce a central multiplicity of 6.37 ± 0.52.

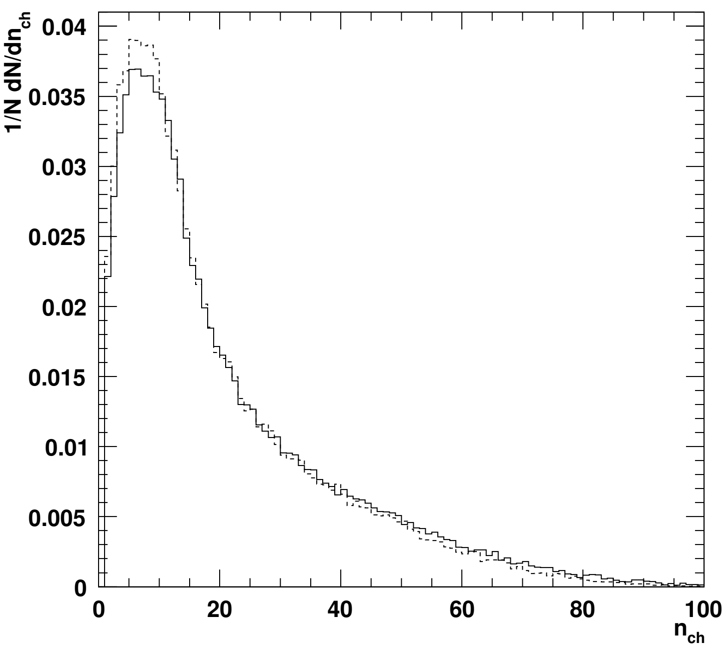

Figure 4.6: Event multiplicity distribution of 100,000 minimum bias events normalised to the number of events. The average event multiplicity within the LHCb acceptance for the tuned settings (solid line) is 18.81 ± 0.06 and 17.54 ± 0.06 for the original LHCb settings (dashed line).

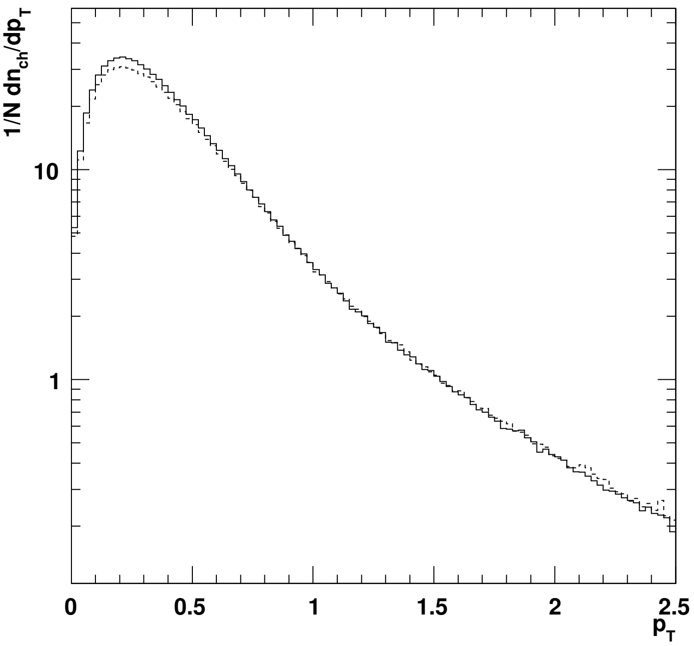

Figure 4.7: Transverse momentum distribution of particles within the LHCb acceptance in minimum bias events normalised to the number of events. The tuned settings (solid line) produce a lower average transverse momentum than the original LHCb settings due to the increased particle multiplicity.

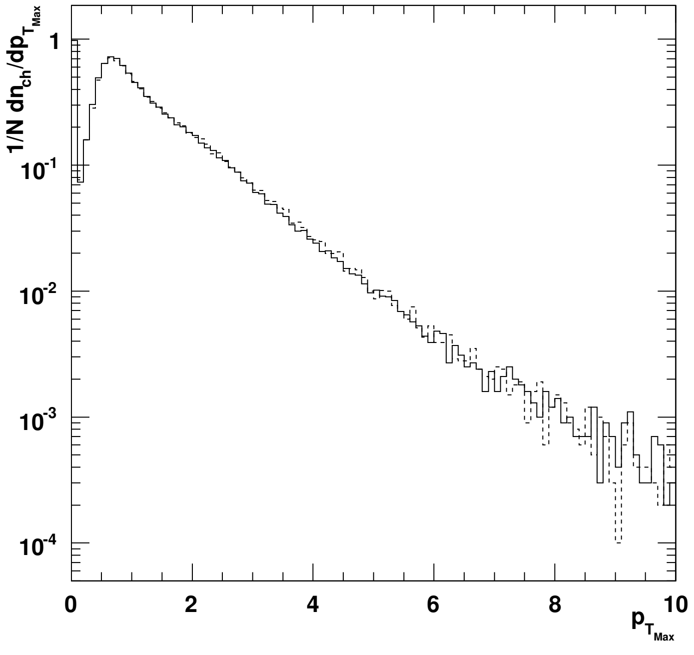

Figure 4.8: Maximum transverse momentum of particles produced in minimum bias events normalised to the number of events. The distributions generated using the tuned (solid line) and original (dashed line) settings show no appreciable differences.

Chapter 5

Prototype RICH 1 Spherical Mirror Characterisation

5.1 Introduction

In RICH 1, the focusing of Cherenkov light onto the HPDs is achieved using a combination of spherical converging mirrors which lie within the detector acceptance and secondary planar mirrors positioned outside the detector acceptance. The spherical mirrors must be lightweight to minimise the amount of material within the detector acceptance and must be stable in the RICH 1 C_4F_{10} fluorocarbon gas radiator environment.

For this application, the attractive properties of beryllium [48, 49] are: long radiation length, good rigidity, lightweight, non-magnetic, fluorocarbon compatibility, low coefficient of thermal expansion, and oxidation resistance in air. Polished beryllium surfaces have a high reflectivity, >95%, in the infrared, while in the visible and ultraviolet the reflectivity is approximately 50%. The typical average surface roughness of polished beryllium is ~20 - 30 nm rms. Reflective metals applied to beryllium evaporatively can produce surface finishes of ~1 - 3 nm rms with reasonable reflectivity in the visible and ultraviolet range but are costly and difficult to achieve [50]. A thin glass layer fused onto a beryllium substrate provides a glass surface which can be polished by standard optical methods and then coated with an aluminium reflective film, increasing the mir-

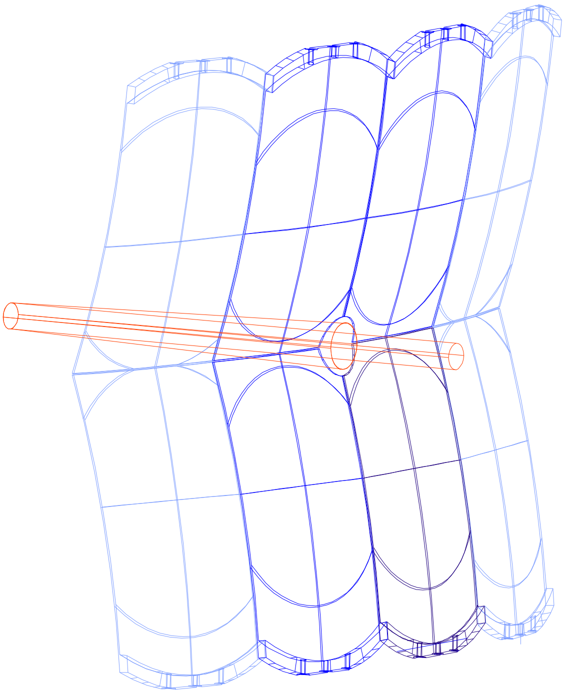

Figure 5.1: Schematic of the RICH1 spherical mirror array as viewed from the rear. The interaction point is located to the left of the image. The central four mirrors each have a section removed to accommodate the beampipe.

ror reflectivity to greater than 90%. The beryllium substrate serves to support the thin glass layer, being rigid enough to maintain the desired reflective spherical surface. The thermal expansion of the glass is tuned to match that of the beryllium.

Figure 5.1 shows the arrangement of the RICH1 spherical mirrors about the beampipe. The mirror arrangement obeys rotational symmetry i.e., the upper-left mirror is identical to the lower-right mirror. The four inner mirrors have their innermost corners removed to accommodate the beampipe.

5.2 Mirror Characterisation

The two main parameters defining the optical quality of a mirror are the radius of curvature, R, and the average geometrical quality, D_0. The parameter D_0 is defined as the diameter of the circle at the mirror centre of curvature (CoC) which contains 95% of the reflected light intensity from a point source placed at the CoC. The precision of the D_0 and R measurements are $\sigma_{D_0} = 0.06\,\mathrm{mm}$ and $\sigma_R = 1\,\mathrm{mm}$, respectively.

The quantity σ_s, defined as $\sigma_s = D_0/4$, would represent the rms value of the spot light distribution if it had a Gaussian shape. The angular precision of the mirror, σ_θ, is defined as the rms angular deviation of the normal to the mirror surface at a given point from the radius of curvature at that point and is related to D_0:

$$\sigma_\theta = \frac{\sigma_s}{2R} = \frac{D_0}{8R}, \tag{5.1}$$

where the factor 2 in the denominator takes account of the reflection at the mirror surface. D_0 is independent of the spot shape and distribution; while σ_θ, where a radial symmetry for the spot is supposed, can be considered an approximation of the rms of the spot distribution.

5.3 Prototype Beryllium Mirror

The full-sized prototype mirror was designed to be as thin as possible, minimising the fractional radiation length, X_0, of the detector, but at the same time rigid enough not to deform under its own weight. It is designed according to the RICH 1 specifications, so that if successful, it could be installed as a final RICH 1 mirror. It is the first beryllium-glass mirror ever fabricated with large geometrical dimensions ($\sim$ 400 mm×660 mm) and a thin beryllium substrate ($\sim$ 3.8 mm). The mirror dimensions are constrained by limitations in the manufacturing size of the beryllium blanks. The largest beryllium blank from which a mirror can be manufactured is disc shaped, 800 mm in diameter. The design consists of a 3 mm thick spherically shaped beryllium substrate (R=2700 mm) coated with a thin glass layer (0.3 - 0.5 mm) with a 20 mm thick beryllium rim at one edge

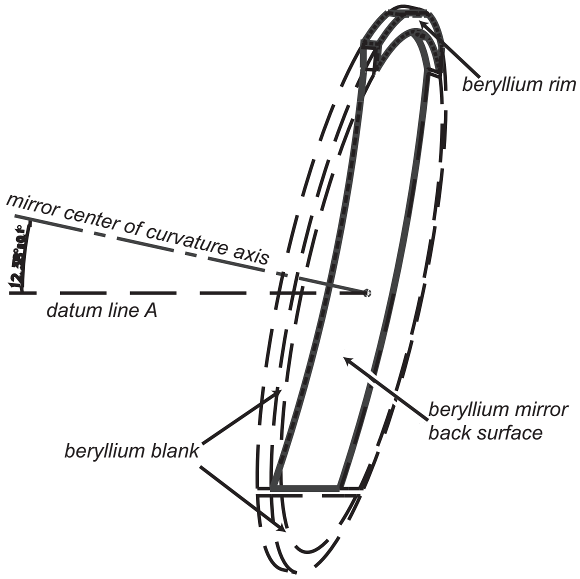

Figure 5.2: A drawing showing the outline of the mirror (continuous line) within the disk-shaped blank (dashed line) from which the mirror is machined. Datum line A is the horizontal axis.

for support (see Fig. 5.2). The mirror is rectangular in projection. The rim serves to bolt the mirror to the mirror support structure which lies outside the LHCb acceptance. The mirror specifications are listed in table 5.1.

The dimensions in table 5.1 refer to the drawings in figure 5.3. The thickness of the beryllium substrate (3 mm) and of the glass coating (0.3 - 0.5 mm) is to satisfy the material budget within the LHCb acceptance, i.e. contribute no more than 2% of a radiation length ($X_0 < 2\%$) and no more than 1% of an interaction length ($\lambda_I < 1\%$). The radius of curvature precision σ_R should be better than:

$$\sigma_R \simeq \frac{\sigma_d}{r_c} R \simeq 1.6\% \cdot R, \tag{5.2}$$

where σ_d ($\simeq$0.72 mm) is the photodetector precision (2.5 mm × 2.5 mm pixel size) and r_c is the maximum Cherenkov cone base radius on the mirror ($\simeq$45 mm for C_4F_{10} in

Property	Value
Dimensions (mm)	383.5×660
Average Thickness (mm)	3 (Be) and $0.3 - 0.5$ (glass)
Radius of Curvature, R (mm)	$2700 \pm 1\%$
Spot Size, D_0 (mm)	< 2.5
Contrib. to Radiation Length, X_0 (%)	< 2
Contrib. to Interaction Length, λ_I (%)	< 1
Surface Roughness (nm)	< 5

Table 5.1: RICH1 design specifications for the full-sized prototype beryllium mirror.

RICH 1). A radius of curvature of R±1% ensures proper focusing of the Cherenkov photons onto the RICH 1 photodetectors. The D_0 value is required to be smaller than the photodetector pixel size (<2.5 mm) to ensure a good mirror angular resolution (σ_θ<0.12 mrad) which will contribute negligibly to the total RICH 1 single photon Cherenkov angle resolution ($\simeq$1.6 mrad in C_4F_{10} gas). In order to minimise scattering of the reflected light, the smoothness of the polished glass surface is required to be $\sim \lambda/100$, which corresponds to a surface roughness of <5 nm rms for the wavelength region of interest, $\lambda \sim$200 nm to 600 nm.

5.3.1 Mirror Geometry

Drawings of the mirror are shown in Figure 5.3. The mirror rim has three holes into which titanium inserts are glued; this is in accordance with the beryllium safety rules which prohibit any direct fixing of bolts to the beryllium bulk. The central hole supports the mirror from the top (bottom) and is bolted to the support structure through the titanium insert. Two pins fixed to the support bar are inserted into the side holes as a safety mechanism to prevent rotation of the mirror about the central hole axis in case of accidental shocks. The outer part of the rim is cut to form an angled flat surface, such that the mirror is held at the required angle when bolted to the support bar in RICH 1.

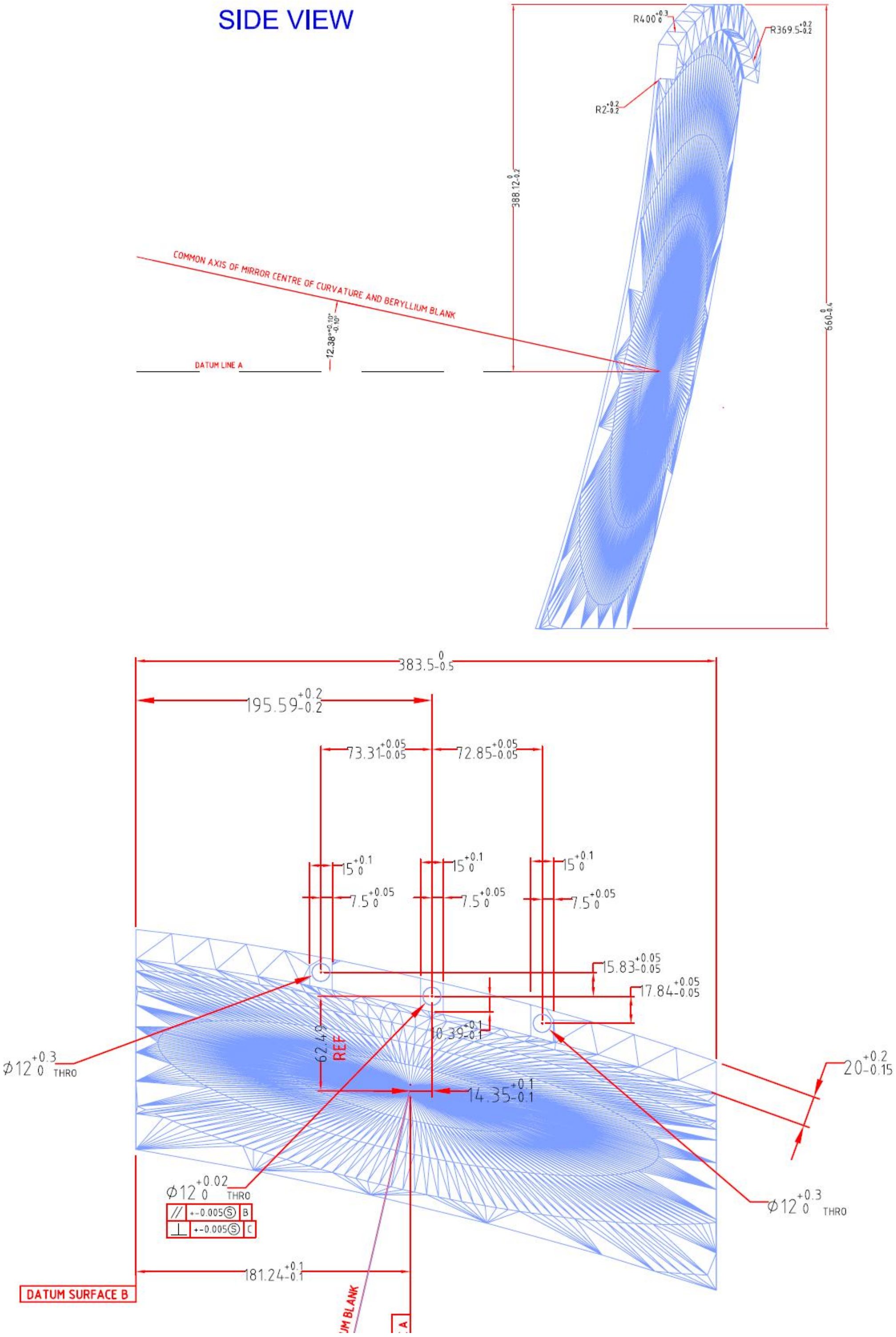

Figure 5.3: Two drawings of the mirror, side view (upper) and top view (lower). The mirror dimensions and the angular orientation are shown. The mirror vertical tilt is 12.38° i.e. the angle between the mirror centre of curvature axis (projection onto plane of this page) and the horizontal (datum line A). The mirror horizontal tilt is 12.97° i.e. the angle between the mirror centre of curvature axis (projection onto datum plane B) and the horizontal (datum line A). The web-like line structures in the drawings are to guide the eye.

5.3.2 Manufacturing Process

“Vacuum-hot-pressing” technology is used to produce the beryllium blank. Powder metallurgy is used to manufacture beryllium parts. Beryllium powder is placed into a disc-shaped die, the powder is vibrated to obtain a homogeneous distribution, while heat and pressure are applied to compress and consolidate the powder into a solid metallic object. At the same time a vacuum is applied to outgas and prevent the formation of air bubbles in the blank. The fabricated beryllium blank is rectangular shaped (800 mm × 800 mm) with a thickness of 40 mm. It is then machined down to a 20 mm thick spherical blank of diameter $\sim$800 mm with a radius of curvature approximately equal to the desired value for the mirror. The blank is then machined to the final shape and thickness of the mirror and repeatedly annealed to relieve internal stresses. The resultant beryllium substrate is $\sim$4 mm thick with a radius of curvature very close to its final value. The substrate was not machined to its design thickness of 3 mm due to concerns about the ability of the blank to withstand further machining. A radiation hard glue with low outgassing[1] is used to glue the titanium inserts into the holes of the beryllium substrate rim.

5.3.3 Optical Surface

The glass[2] type is selected to have a coefficient of thermal expansion which matches that of beryllium, $\alpha_{\mathrm{glass}} \cong \alpha_{\mathrm{Be}}$. Several small segments of glass are placed on the substrate front face such that the optical area is completely covered. The position of the segments can be seen in figures 5.4 and 5.5. The glass and substrate are then placed into an oven and heated to a temperature of $\sim$600°C to melt the glass. The individual glass segments merge into one layer and fuse to the beryllium substrate. The mirror is then left to slowly cool. The glass layer is then polished using standard optical methods. Fine tuning of the mirror radius of curvature is achieved by the glass polishing i.e., by varying

---

[1] The glue composition is propriety information.

[2] The glass properties and composition is propriety information. Its approximate composition is $SiO_2 \sim 60\%$, $CdO \sim 20\%$, $Nb_2O \sim 15\%$, $PbO \sim 5\%$, $B_2O_3 \sim 2\%$, $BaO \sim 1\%$.

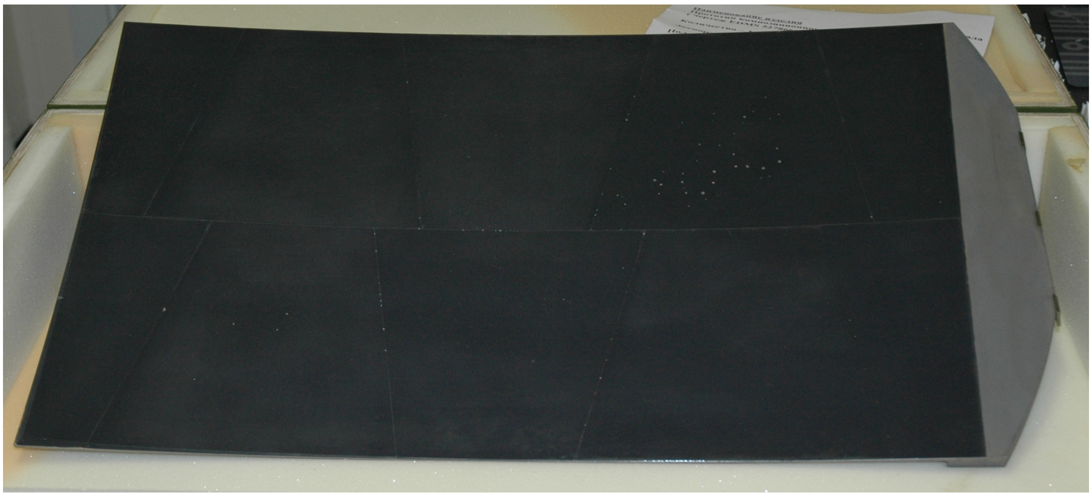

Figure 5.4: The optical surface (dark area) of the glass-coated beryllium mirror. The boundaries between the nine glass segments are just visible. The lighter spots present are defects in the glass layer where the beryllium substrate is exposed. The defects are concentrated in one glass segment and along joins between segments.

the thickness of the glass layer across the mirror, typically 0.3 - 0.5 mm.

The uncoated beryllium surface (rim and back side) is passivated by the natural formation of a beryllium oxide surface film resulting from its exposure to air.

The last step would be the application of a reflective coating after the successful testing and subsequent acceptance of the mirror. The reflective coating [51] increases the reflectivity to $\gtrsim 85\%$ for wavelengths in the range 250 - 500 nm and $\gtrsim 70\%$ for wavelengths in the range 200 - 250 nm. The coating consists of a thin chromium adherence layer followed by an aluminium layer protected by a SiO_2-HfO_2 reflective enhancement layer. This type of coating has already been successfully applied onto the surface of the LHCb RICH 2 glass mirrors.

5.3.4 Characterisation of the Optical Surface

On visual inspection a number of "dead" areas were identified on the mirror surface (Fig. 5.6). A number of pits are visible in the glass layer and are due to a defect in the glass coating process. There are approximately 70 pits varying $\sim$0.5 - 1 mm in diameter,

Figure 5.5: A view of the mirror showing the three titanium inserts and the glass coating.

concentrated mainly in one of the glass segments and along the glass segment boundaries. In addition, the mirror has a large chamfer, up to $\sim 5\,\mathrm{mm}$ from the mirror edge. The largest contribution to the optically dead area due to the chamfer is from the edges of the mirror farthest from the mount point. The large chamfer at the bottom edge of the mirror is due to correcting (shortening) the mirror radius of curvature which required a thicker layer of glass at the lower extremities of the mirror. The resulting optical dead area is very small, with the pits and chamfer contributing $\sim 0.1\%$ and $\sim 0.5\%$, respectively.

A uniform glass thickness is possible by manufacturing future substrates with a more accurate radius of curvature. Defects in the glass can be eliminated in future mirrors by refining the glass layering technique. The present glass layer could be removed and re-applied to remove the defects.

5.4 Radius of Curvature Measurements

The measurement of the mirror radius of curvature, R, and D_0 was performed in an optical laboratory at CERN, in a darkroom environment with air circulation and dust filters. The experimental setup is shown in Figure 5.7. A point-like source is obtained from a diode laser (λ=641 nm) connected to an optical fibre. The light from the point source is passed through a suitable lens to ensure that the mirror surface is adequately illuminated. The laser and a CCD camera[3] are mounted on a sliding table and can be moved together along the optical bench. The CCD camera is 16 bit, with a pixel size of $9\,\mu\mathrm{m} \times 9\,\mu\mathrm{m}$ and a sensitive area of $6.9\,\mathrm{mm} \times 4.6\,\mathrm{mm}$. The mirror is held by a three-point support mounted on the optical bench. The mount introduces no additional stresses in the mirror.

The mirror is positioned at a distance, d, from the sliding table, corresponding to the approximate expected radius of curvature of the mirror. The mirror spot is centred on the CCD camera by adjusting the orientation of the mirror mount. The approximate centre of curvature of the mirror is located by visually inspecting the spot image as

---

[3] DTA model HR400E with a KODAK sensor KAF-400E CCD.

Figure 5.6: The optical surface of the glass-coated beryllium mirror showing the two causes of optically-dead areas: pits in the glass layer (upper image) and the large chamfer due to the correction of the substrate's radius of curvature (lower image). The pits are confined to the boundaries between the glass segments and the centre of one particular segment. The large chamfer is only present at the edges of the mirror farthest from the mount point.

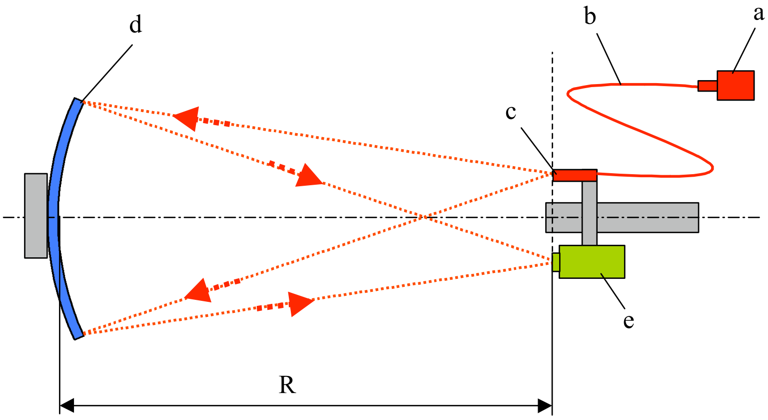

Figure 5.7: Schematic setup for the radius of curvature, R, and spot-size, D_0, measurements of a spherical converging mirror. A point-like source (c) is created by passing light from a 641 nm diode laser (a) through an optical fibre (b). The light source and a 16 bit CCD camera (e) are fixed to a sliding table mounted on the optical bench. The spherical mirror (d) is held in a three-point mount fixed to the optical bench.

the position of the sliding table is varied. Once the approximate centre is located the position of the sliding table is recorded.

The spot image is then assessed at several points about the centre of curvature using the CCD camera to ensure that the spot remains within the boundaries of the sensor for the duration of the measurement and does not saturate the CCD. If necessary, fine adjustments of the mount orientation are used to re-position the spot image and the laser current altered until the peak measured intensity is approximately 2/3 of the saturation intensity. The sliding table is then returned to the approximate centre of curvature position and secured to the optical bench. The radius of curvature measurement is performed using automated LabVIEW[4] software.

The LabVIEW program uses a stepping motor to vary the position of the camera and point source in a range $\pm \sim 20$ mm about their starting position. The camera and point

---

[4] LabVIEW (Laboratory Virtual Instrumentation Engineering Workbench) is a platform and development environment for a visual programming language from National Instruments.

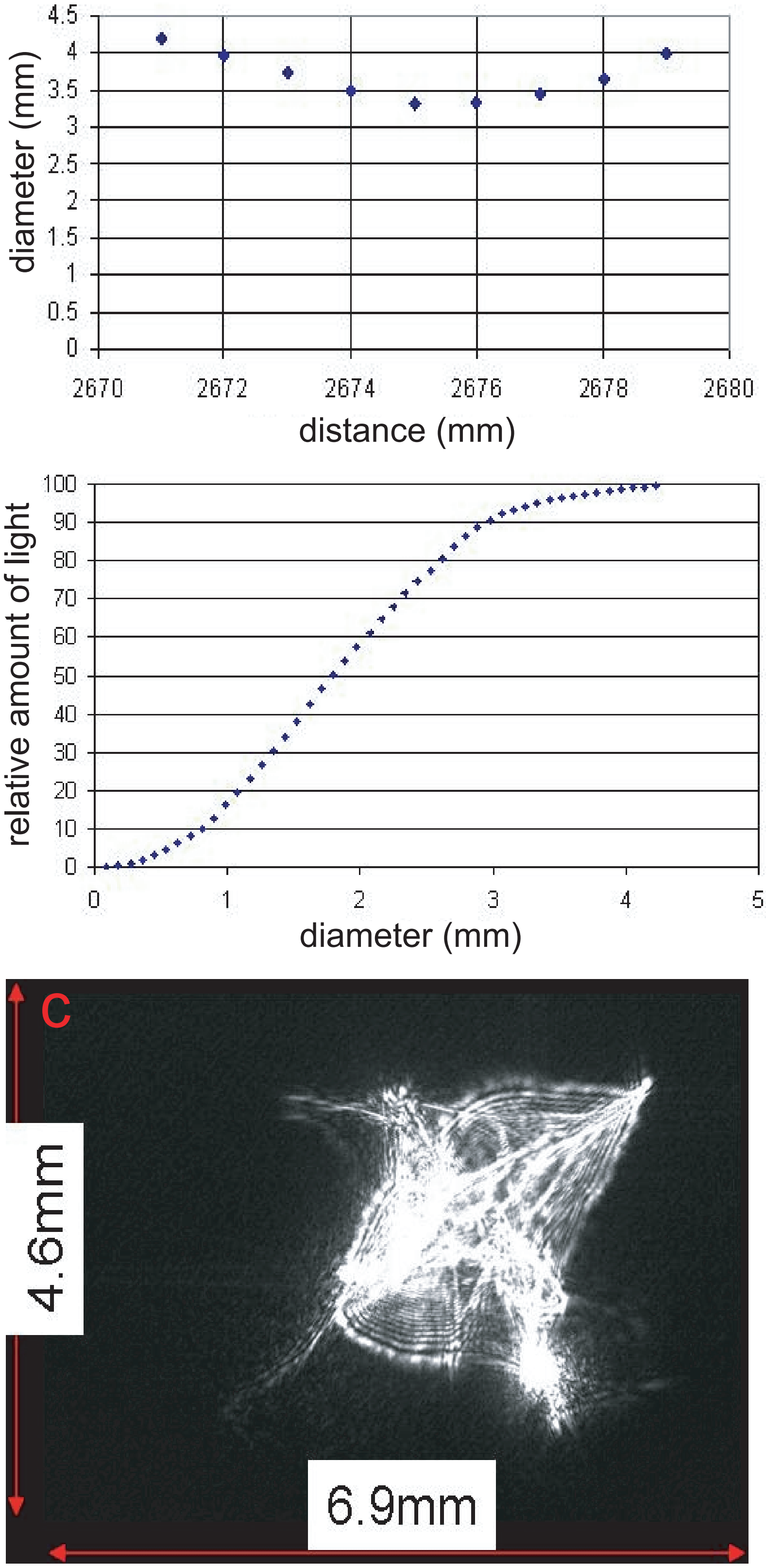

Figure 5.8: The spot size versus the distance of the mirror from the CCD camera, the minimum is for R=2675 mm (upper image). The relative amount of light (%) as function of the circle diameter for the smallest spot; 95% is contained by a circle of diameter 3.33 mm, i.e., $D_0 = 3.33$ mm (central image). Photograph of the smallest spot (lower image).

source are first positioned at one extreme of the range and subsequently moved towards the other extreme in steps of 1 mm. At each 1 mm step the spot is photographed by the CCD and the data stored. At the end of the scan, the LabVIEW program determines the spot-size of each image. The method of determining the spot-size is detailed in section 5.4.1.

The radius of curvature, R, of the mirror is defined as the distance between the mirror reflective surface centre and the CCD sensor for the smallest spot size. The measured values were $D_0 = 3.33 \pm 0.02\,\mathrm{mm}$ and $R = 2675 \pm 1\,\mathrm{mm}$. The spot with diameter D_0 is shown in the plots of figure 5.8 in addition to the spot intensity profile.

5.4.1 Determination of D_R

The determination of D_R is performed using labVIEW software to analyse the spot image captured at a distance, R, along the mirror optical axis. The procedure described below is based on the following assumptions:

- All the reflected light from the mirror strikes the CCD.
- The spot is positioned centrally.
- No CCD pixel is saturated.

5.4.1.1 CCD Output and Dark Current

The CCD produces a measurable output, $I_r(x_i, y_j)$, at each pixel position, (x_i, y_j). Background contributions to the output may be compensated for with direct measurement of the CCD output with no incident light, this contribution is called “dark current”. The signal, $I(x_i, y_j)$, is well-approximated as a linear response to the incident radiation once the dark current is compensated for. The CCD dark current is affected by the temperature of the chip. The CCD is therefore maintained at a constant temperature once the dark current has been measured.

5.4.1.2 Calculation of Spot Centre and Diameter

The spot-size, D_R, is determined using a centre of gravity method. In general, the centre of gravity is calculated using equation 5.3:

$$x_c = \frac{\int\limits_A x \cdot I\left(x, y\right) dA}{\int\limits_A I\left(x, y\right) dA}, \quad y_c = \frac{\int\limits_A y \cdot I\left(x, y\right) dA}{\int\limits_A I\left(x, y\right) dA}. \tag{5.3}$$

However, the CCD only measures the average light intensity incident on discrete areas i.e., the CCD pixels. In this case the approximate centre of gravity is given by:

$$x_c \approx \frac{\sum\limits_{i,j}^{M,N} x \cdot I\left(x_i, y_j\right)}{\sum\limits_{i,j}^{M,N} I\left(x_i, y_j\right)}, \quad y_c \approx \frac{\sum\limits_{i,j}^{M,N} y \cdot I\left(x_i, y_j\right)}{\sum\limits_{i,j}^{M,N} I\left(x_i, y_j\right)}, \tag{5.4}$$

where (x_i, y_j) and $I(x_i, y_j)$ represent the centre and measured intensity of pixel (i, j) respectively.

The intensity, S_D, falling within a distance, D, from the central pixel is then calculated. S_D is given by the integral of $I\left(x, y\right)$ over a region A_D, where A_D is a circle with diameter D and centre (x_c, y_c):

$$S_D = \int\limits_{A_D} I\left(x, y\right) dA, \tag{5.5}$$

or in the case of discrete pixels:

$$S_D = \sum_{i,j} I\left(x_i, y_j\right), \tag{5.6}$$

where the indicies i, j, run over all those pixels which lie completely within the region A_D. This process is repeated, with the diameter of the circles varying in steps of 10 pixels i.e., 0.09 mm. The analysis of an image is concluded when the edge of the current circle exceeds the boundaries of the image. The results are written to file in the form of a percentage of the total signal, P_D:

$$P_D = \frac{S_D}{S_{\text{tot}}}, \tag{5.7}$$

where S_{tot} is the total signal from the whole image. The spot diameter, D_R, is defined as the diameter of a circle containing 95% of the incident light.

Using this method we obtain the minimum spot diameter, D_R, at various radii, R. The minimum value of D_R is then identified as the mirror D_0 and the corresponding value of R as its radius of curvature. The radius of curvature measurement has a precision of $\sigma_R \approx 1\,\text{mm}$ and the D_0 measurement has a precision of $\sigma_{D_0} \approx 0.02\,\text{mm}$ [52].

5.4.2 Components of the Spot Image

An image of the spot approximately 30 cm from the focal point is shown in figure 5.9. Structures associated with the surface defects can clearly be identified. In addition, a number of large diameter rings are visible in the image.

Whilst the structures corresponding to the boundaries between the glass segments are most likely present on the actual mirror surface, the ring-like structures are not. The rings are concentric and their centres coincide with the centre of the blank itself. The standard optical polishing methods used to produce the finished optical surface are unlikely to have caused the ring-like structures since the polishing strokes traverse the mirror and their orientation is varied throughout the process. It is therefore reasonable to assume that the ring-like structures are due to the blank machining process and are present at the beryllium-glass interface.

Since the spot image at the centre of curvature contains contributions from reflections at the glass and beryllium surfaces, we assume that the measured D_0 value is likely to change once the reflective coating is applied to the mirror. It is impossible to determine the extent of the change theoretically since a detailed knowledge of the glass thickness over the entire surface of the mirror is required. However, we expect that in the worst case scenario, the D_0 of the coated mirror will be equal to that of the uncoated mirror.

5.4.3 Metrology Measurements

The CERN metrology service measured the overall dimensions and thickness of the mirror and it was found to be generally within the specifications. The beryllium substrate

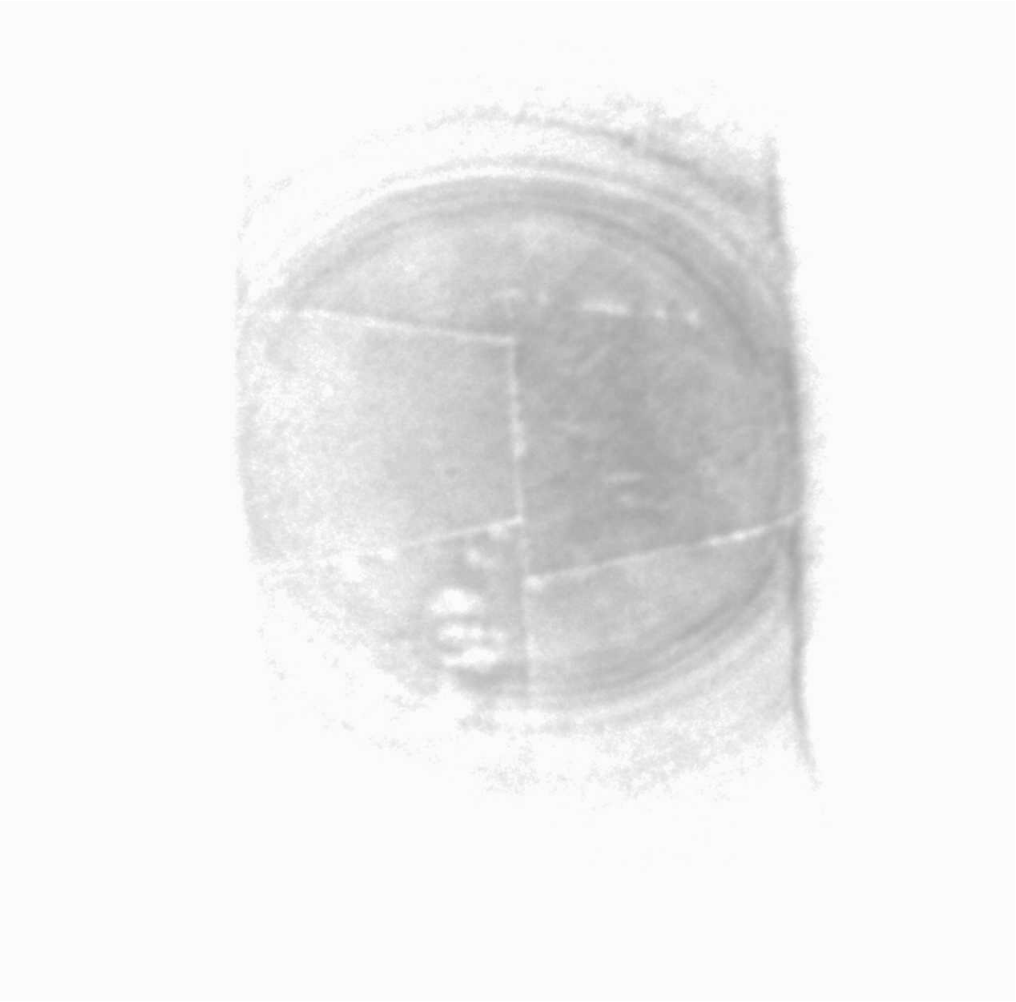

Figure 5.9: An enhanced and colour-inverted image of the light reflected from the beryllium mirror. The image clearly shows structures associated with the glass segment boundaries and surface defects. The glass segment boundaries are visible due to reflections from the glass-beryllium interface in addition to the air-glass interface. Applying the reflective coating to the mirror will change the spot image since only the reflective surface will contribute.

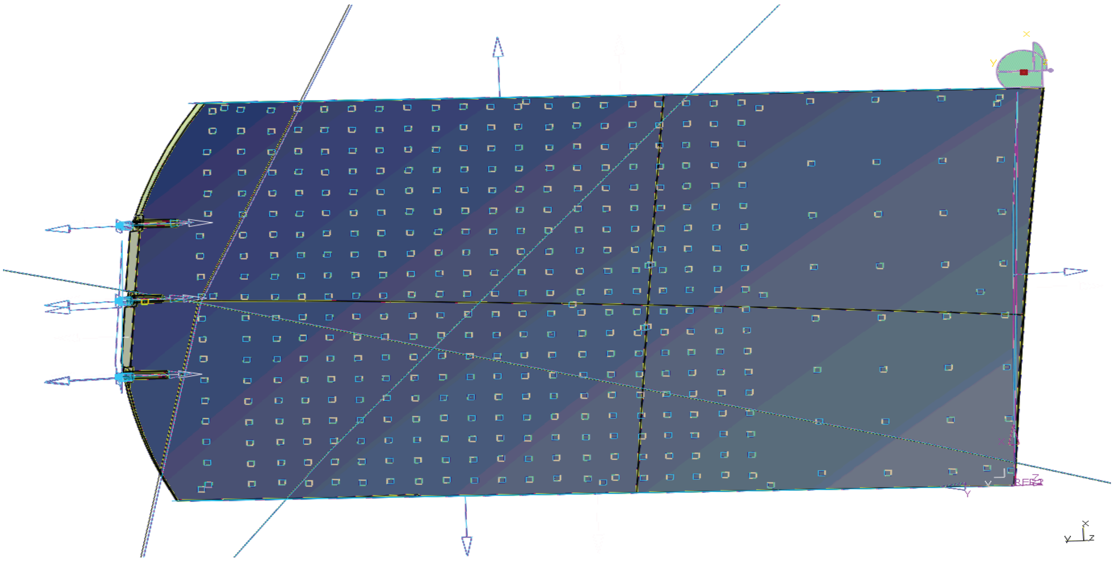

Figure 5.10: Schematic showing the positions of the ~ 400 points on the optical surface measured by the CERN Metrology group. Each square marks the location of a measured point.

with the glass is ~ 4 − 5 mm thick. On average, the mirror consists of a ~ 3.8 mm thick beryllium substrate with a ~ 0.4 mm thick glass layer. The glass layer is thinnest at the centre (~ 0.3 mm) and gradually increasing in thickness towards the edges up to ~ 1 mm. The spatial coordinates of a large number of points (~ 400) were measured on the mirror surface and then fitted to a sphere to extract the mirror radius of curvature and tilt. The position of the points is indicated in figure 5.10. The metrology extracted value of $R = 2677 \pm 1$ mm is close to the optical measurement. The extracted angular mirror tilts are within the tolerances of the design specifications given in figure 5.3.

A summary of the mirror parameters is given in table 5.2. The dimensions refer to

Parameter	Value
Dimensions (mm)	383×660
Substrate Thickness (mm)	3.8 (Be) + 0.4 (glass)
Radius of Curvature, R (mm)	2675
Spot Size, D_0 (mm)	3.33
Contrib. to Radiation Length, X_0 (%)	~ 1.6
Contrib. to Interaction Length, λ_I (%)	~ 1
Weight (kg)	2.7
Surface Roughness, R_z (nm)	< 5

Table 5.2: Parameters of the full-sized prototype beryllium mirror.

the drawings of figure 5.3. The values for the interaction length and radiation length contributions can only be estimated because the exact composition of the glass is not known. The surface roughness of the optical surface was not measured at CERN but certified by the manufacturer to be R_z <5 nm[5].

The mirror is within the RICH 1 specifications, except for the D_0 which should be <2.5 mm; however the measured value of 3.3 mm is tolerable. The specification of the beryllium substrate thickness was relaxed from 3 mm to ∼4 mm because of the high risk of breaking the beryllium blank during machining.

Unfortunately, contractual difficulties with the blank manufacturer has forced a recent change in the preferred technology choice for the RICH 1 mirrors. There are no plans to evaluate the exact impact of the beryllium mirror optical performance at present.

5.5 Conclusion

The prototype spherical beryllium mirror is the first beryllium-glass mirror ever fabricated with large geometrical dimensions (∼ 400 mm× 660 mm) and a thin beryllium substrate (∼ 3.8 mm). The mirror is designed according to the RICH 1 specifications so

---

[5] R_z is the total roughness i.e., the vertical distance from the deepest valley to the highest peak within the sampling length.

that, if acceptable, it can be installed as a final RICH 1 mirror.

A number of pits are present in the optical surface of the mirror due to a defect in the glass-coating process. The glass layer is non-uniform and a smooth increase in thickness is observed towards the edges farthest from the mirror mount point. The variation in glass thickness represents a correction to the radius of curvature of the beryllium substrate.

The mirror was found to have a radius of curvature, R, of 2675 ± 1 mm and a spot diameter, D_0, of 3.33 ± 0.02 mm. The mirror radius of curvature satisfies the requirement of $R = 2700$ mm $\pm 1\%$ but the mirror spot size is slightly larger than the specification of $D_0 < 2.5$ mm. The mirror was deemed suitable for use in RICH 1 but contractual difficulties with the blank manufacturer forced a change in the preferred mirror technology choice.

Chapter 6

LHCb Sensitivity to a_{fs}

6.1 Introduction

$\mathcal{CP}$ violation in $\mathrm{B_s^0}$-$\mathrm{\overline{B}_s^0}$ mixing is expected to be tiny in the Standard Model, but can be significantly enhanced in the presence of new $\mathcal{CP}$-violating phases in general physics models [53]. This can be probed through the measurement of the charge asymmetry in untagged flavour-specific decays:

$$A_{fs}(t) = \frac{\Gamma\left(\mathrm{B^0} \text{ or } \mathrm{\overline{B}^0} \to f\right)(t) - \Gamma\left(\mathrm{B^0} \text{ or } \mathrm{\overline{B}^0} \to \bar{f}\right)(t)}{\Gamma\left(\mathrm{B^0} \text{ or } \mathrm{\overline{B}^0} \to f\right)(t) + \Gamma\left(\mathrm{B^0} \text{ or } \mathrm{\overline{B}^0} \to \bar{f}\right)(t)} \tag{6.1}$$

where the state f is a flavour eigenstate and the subscript on A_{fs} stands for "flavour-specific". Here $A_{fs}(t)$ refers to the untagged time-dependent asymmetry which is different to the physical constant a_{fs}, which parameterises $\mathcal{CP}$ violation in mixing, which we aim to measure. If a_{fs} is measured in the semileptonic channel, it is sometimes also called a_{SL} or A_{SL} as in [54].

In the Standard Model this is expected to be a very small effect [54]:

- For the $\mathrm{B_d^0}$ system, $a_{fs}^d = -\left(4.8^{+1.0}_{-1.2}\right) \cdot 10^{-4}$
- For the $\mathrm{B_s^0}$ system, $a_{fs}^s = +\left(2.06 \pm 0.57\right) \cdot 10^{-5}$.

The LHCb experiment is expected to collect about 1 million $\mathrm{B_s^0} \to \mathrm{D_s^-}\mu^+\nu_\mu$ events in $2\,\mathrm{fb}^{-1}$[55], and 140 k $\mathrm{B_s^0} \to \mathrm{D_s}\pi$[1] events in $2\,\mathrm{fb}^{-1}$[56]. These large event samples will provide an opportunity to measure A_{fs} with a high statistical precision.

The measured untagged time-dependent asymmetry $A_{fs}(t)$ depends on three parameters: the production asymmetry, A_P, and the charge detection asymmetry, A_C and a_{fs}. Two of the parameters can be extracted simultaneously, the remaining parameter must be taken from other measurements. The results of a fast Monte Carlo study of a simultaneous measurement of a_{fs} and the production asymmetry, where we assume the detection asymmetry is well-known, is presented in section 6.5.

Besides the important measurement of a_{fs} itself, the measurement of the production asymmetry provides valuable input to many other analyses. Interestingly, the measurement of the production asymmetry with this technique remains possible even without external constraints on the charge detection asymmetry as long as a_{fs} is small compared to the required precision on the production asymmetry. Since a_{fs} is expected to be tiny, this is the case for most measurements at LHCb (except of course the measurement of a_{fs} itself).

This chapter is organised as follows. The form of the time-dependent asymmetry is established in section 6.2. The fast Monte Carlo simulation method for assessing statistical precision is described in section 6.4. Section 6.5 presents the sensitivity to a_{fs} for two channels, $\mathrm{B_s^0} \to \mathrm{D_s}\mu\nu$ and $\mathrm{B_s^0} \to \mathrm{D_s}\pi$. Conclusions are presented in section 6.6.

6.2 Theory

The relevant parameters involved in $\mathrm{B^0}$ mixing and the time evolution of a $\mathrm{B^0}$ that is a flavour eigenstate at $t = 0$ are discussed in chapter 3. Expressions for the time-dependent asymmetry A_{fs} are developed, taking into account detector effects and the additional production and detection asymmetries.

---

[1] Here this notation always implies charged-conjugate modes with and without oscillation, unless the context requires otherwise. So the combined expected yield of $\mathrm{B_s^0} \to \mathrm{D_s^-}\pi^+$, $\mathrm{B_s^0} \to \mathrm{D_s^+}\pi^-$, $\overline{\mathrm{B}}{}_\mathrm{s}^0 \to \mathrm{D_s^-}\pi^+$ and $\overline{\mathrm{B}}{}_\mathrm{s}^0 \to \mathrm{D_s^+}\pi^-$ is 140 k in $2\,\mathrm{fb}^{-1}$.

6.2.1 a^q_{fs} in the Standard Model

a_{fs} is defined in equation 3.50. Extending the definition to explicitly state the system to which it refers i.e., the B^0_q system where $q = d, s$; we have:

$$a^q_{fs} \equiv \left|\frac{\Gamma^q_{12}}{M^q_{12}}\right| \sin\phi^q, \tag{6.2}$$

where the phase, ϕ^q is defined through:

$$\frac{M^q_{12}}{\Gamma^q_{12}} = -\left|\frac{M^q_{12}}{\Gamma^q_{12}}\right| e^{i\phi^q}. \tag{6.3}$$

M^q_{12} and Γ^q_{12} are predicted in the Standard Model (SM) and related to other CKM parameters [57]:

$$M^q_{12} = -\frac{G_F^2 m_w^2 \eta_B m_{B_q} B_{B_q} f^2_{B_q}}{12\pi^2} S_o\left(\frac{m_t^2}{m_W^2}\right)(V^*_{tq}V_{tb})^2, \tag{6.4}$$

$$\Gamma^q_{12} = \frac{G_F^2 m_b^2 \eta'_B m_{B_q} B_{B_q} f^2_{B_q}}{8\pi^2}\left[(V^*_{tq}V_{tb})^2 + V^*_{tq}V_{tb}V^*_{cq}V_{cb}\mathcal{O}\left(\frac{m_c^2}{m_b^2}\right) + (V^*_{cq}V_{cb})^2\mathcal{O}\left(\frac{m_c^2}{m_b^2}\right)\right], \tag{6.5}$$

where G_F is the Fermi constant, m_W the W boson mass, and m_i the mass of quark i; m_{B_q}, f_{B_q} and B_{B_q} are the B^0_q mass, decay constant and bag parameter respectively. $S_0(x_t)$ is a known Inami-Lin function approximated very well by $0.784\ x_t^{0.76}$, V_{ij} are the elements of the CKM matrix, η_B and η'_B are QCD corrections of order unity.

Within the SM a^q_{fs} is small [58], but non-zero, as (c.f. equation 6.2):

$$\left|\frac{\Gamma^q_{12}}{M^q_{12}}\right| = \mathcal{O}\left(\frac{m_b^2}{m_t^2}\right) \ll 1 \tag{6.6}$$

$$\arg\left(-\frac{\Gamma^q_{12}}{M^q_{12}}\right) = \mathcal{O}\left(\frac{m_c^2}{m_b^2}\right) \ll 1 \tag{6.7}$$

$$a^q_{fs} \propto -\mathsf{Im}\left(\frac{V^*_{cq}V_{cb}}{V^*_{tq}V_{tb}}\right) \tag{6.8}$$

6.2.2 Measuring A_{fs}

Demanding that the decays proceed to flavour-specific states implies that if the observed decays are $\mathrm{B}^0 \to f$ and $\overline{\mathrm{B}}^0 \to \bar{f}$, the decays $\mathrm{B}^0 \to \bar{f}$ and $\overline{\mathrm{B}}^0 \to f$ must be forbidden, i.e.:

$$A_{\bar{f}} = \bar{A}_f = 0, \tag{6.9}$$

therefore:

$$\lambda_f = \frac{1}{\lambda_{\bar{f}}} = 0. \tag{6.10}$$

Additionally, we require that there is no direct CP violation in the decay, i.e.:

$$|A_f| = \left|\bar{A}_{\bar{f}}\right|. \tag{6.11}$$

The rate equations 3.71 to 3.74 now simplify to:

$$\Gamma\left(\mathrm{B}^0 \to f\right)(t) = N_f \left|A_f\right|^2 e^{-\Gamma t} \frac{1}{2}\left[\cosh\left(\frac{1}{2}\Delta\Gamma t\right) + \cos\left(\Delta m t\right)\right] \tag{6.12}$$

$$\Gamma\left(\mathrm{B}^0 \to \bar{f}\right)(t) = N_f \left(1 - a_{fs}\right)\left|\bar{A}_{\bar{f}}\right|^2 e^{-\Gamma t} \frac{1}{2}\left[\cosh\left(\frac{1}{2}\Delta\Gamma t\right) - \cos\left(\Delta m t\right)\right] \tag{6.13}$$

$$\Gamma\left(\overline{\mathrm{B}}^0 \to \bar{f}\right)(t) = N_f \left|\bar{A}_{\bar{f}}\right|^2 e^{-\Gamma t} \frac{1}{2}\left[\cosh\left(\frac{1}{2}\Delta\Gamma t\right) + \cos\left(\Delta m t\right)\right] \tag{6.14}$$

$$\Gamma\left(\overline{\mathrm{B}}^0 \to f\right)(t) = N_f \left(1 + a_{fs}\right)\left|A_f\right|^2 e^{-\Gamma t} \frac{1}{2}\left[\cosh\left(\frac{1}{2}\Delta\Gamma t\right) - \cos\left(\Delta m t\right)\right]. \tag{6.15}$$

Substituting equations 6.12 to 6.15 into 6.1 we find the time-dependent asymmetry takes the form:

$$A_{fs}(t) = \frac{a_{fs}}{2} - \frac{a_{fs}}{2}\frac{\cos\left(\Delta m t\right)}{\cosh\left(\frac{\Delta\Gamma}{2}t\right)}. \tag{6.16}$$

6.2.3 Introducing Detector Resolution

To obtain the measured decay rates with finite time resolution we need to convolve the expressions 6.12 - 6.15 with an appropriate resolution function. Here we choose a Gaussian (more complicated models can be obtained easily from this by adding up Gaussians of different widths). The decay rates as a function of the measured time, t, are therefore obtained by solving:

$$\Gamma_i(t) = f_i(a_{fs}) \int_0^\infty e^{-\Gamma t'} \left(\cosh\left(\frac{1}{2}\Delta\Gamma t'\right) \pm \cos\left(\Delta m t'\right)\right) \frac{1}{\sqrt{2\pi}\sigma_t} e^{\frac{(t'-t)^2}{2\sigma_t^2}} \, dt', \tag{6.17}$$

where the index i labels the four decay rates given in equations 6.12 to 6.15, and f_i is a time-independent parameter that is different for each of the four decay modes. This can be expressed as

$$\begin{aligned}\Gamma_i(t_0) =& f_i(a_{fs})\mathsf{Re}\left\{\frac{1}{\sqrt{2\pi}\sigma_t}\int\limits_0^\infty e^{-\Gamma\,t}\left(\frac{1}{2}e^{\frac{1}{2}\Delta\Gamma\,t}+\frac{1}{2}e^{-\frac{1}{2}\Delta\Gamma\,t}\pm e^{i\Delta m\,t}\right)e^{\frac{(t-t_0)^2}{2\sigma_t^2}}\,dt\right\}\\ =& f_i(a_{fs})\mathsf{Re}\left\{\frac{1}{\sqrt{2\pi}\sigma_t}\int\limits_0^\infty \left(\frac{1}{2}e^{-\left(\Gamma-\frac{1}{2}\Delta\Gamma\right)t}+\frac{1}{2}e^{-\left(\Gamma+\frac{1}{2}\Delta\Gamma\right)t}\pm e^{-(\Gamma-i\Delta m)\,t}\right)e^{\frac{(t-t_0)^2}{2\sigma_t^2}}\,dt\right\}.\end{aligned} \tag{6.18}$$

Hence the problem reduces to calculating

$$\frac{1}{\sqrt{2\pi}\sigma_t}\int\limits_0^\infty e^{-At}e^{-\frac{1}{2}(t-t_0)^2}\,dt \tag{6.19}$$

for different (sometimes complex) values of A. The decay rates in equation 6.17 can be re-written as:

$$\begin{aligned}&\Gamma_i(t) =\\ &f_i(a_{fs})e^{-\Gamma t+\frac{1}{2}\Gamma^2\sigma_t^2}\left[e^{\frac{1}{8}\sigma_t^2(\Delta\Gamma)^2}\cosh\left(\frac{1}{2}\Delta\Gamma\left(t-\sigma_t^2\Gamma\right)\right)\pm e^{-\frac{1}{2}\Delta m^2\sigma_t^2}\cos\left(\Delta m\left(t-\Gamma\sigma_t^2\right)\right)\right].\end{aligned} \tag{6.20}$$

The details of the calculation can be found in Appendix B.

For the purpose of this study, we use the more simple expression 6.20 throughout. This is sufficiently accurate for decay times $t \geq 4\sigma_t$ (then Freq ≈ 1 and erfi $\approx i$ to a very good approximation). To ensure this assumption is valid we apply a minimum lifetime cut of $t > 5\sigma_t$. Since the data selection in all channels considered uses impact parameter cuts to select long-lived particles anyway, this additional cut has only a very small effect except for the set of MC experiments with the worst lifetime resolution.

6.2.4 Measuring a_{fs} with Untagged Decay Rates

If the production rates for B^0 and $\overline{\mathrm{B}}^0$ are the same, and the detection efficiency of f is the same as that for $\bar{f}$, we find:

$$A_{fs}(t) = \frac{\left(\Gamma\left(\mathrm{B}^0\to f\right)(t)+\Gamma\left(\overline{\mathrm{B}}^0\to f\right)\right)(t)-\left(\Gamma\left(\mathrm{B}^0\to \bar{f}\right)(t)+\Gamma\left(\overline{\mathrm{B}}^0\to \bar{f}\right)(t)\right)}{\left(\Gamma\left(\mathrm{B}^0\to f\right)(t)+\Gamma\left(\overline{\mathrm{B}}^0\to f\right)(t)\right)+\left(\Gamma\left(\mathrm{B}^0\to \bar{f}\right)(t)+\Gamma\left(\overline{\mathrm{B}}^0\to \bar{f}\right)(t)\right)}, \tag{6.21}$$

where the Γ are those given in equations 6.12 to 6.15, modified according to 6.20 to take into account finite time resolutions. Note that acceptance effects (as long as they are charge-symmetric) cancel, which is of particular importance for hadronic decays at LHCb where the impact-parameter based trigger biases the lifetime distribution. The time-dependent asymmetry now takes the form:

$$A_{fs}(t) = \frac{a_{fs}}{2} - e^{-\frac{1}{2}\sigma_t^2\left((\Delta m)^2+\left(\frac{1}{2}\Delta\Gamma\right)^2\right)} \left[\frac{a_{fs}}{2}\right] \frac{\cos\left(\Delta m\ \left(t-\sigma_t^2\Gamma\right)\right)}{\cosh\left(\frac{1}{2}\Delta\Gamma\left(t-\sigma_t^2\Gamma\right)\right)}. \tag{6.22}$$

6.2.5 Production and Detection Asymmetry

At a *p*-*p* collider, there will be a production asymmetry between B^0 and $\overline{\mathrm{B}}^0$ mesons [59]. Any realistic detector is also likely to have a detection asymmetry. Defining:

- N, rate of B^0 production; $\bar{N}$, rate of $\overline{\mathrm{B}}^0$ production;
- ϵ_f, detection efficiency for final state f; $\bar{\epsilon}_f$, detection efficiency for final state $\bar{f}$;

the total, measured time-dependent asymmetry is given by

$$A_{fs}(t) = \frac{\left(N\epsilon_f\Gamma(\mathrm{B}^0\to f)+\bar{N}\epsilon_f\Gamma(\overline{\mathrm{B}}^0\to f)\right)-\left(\bar{N}\bar{\epsilon}_f\Gamma(\overline{\mathrm{B}}^0\to \bar{f})+N\bar{\epsilon}_f\Gamma(\mathrm{B}^0\to \bar{f})\right)}{\left(N\epsilon_f\Gamma(\mathrm{B}^0\to f)+\bar{N}\epsilon_f\Gamma(\overline{\mathrm{B}}^0\to f)\right)+\left(\bar{N}\bar{\epsilon}_f\Gamma(\overline{\mathrm{B}}^0\to \bar{f})+\bar{N}\bar{\epsilon}_f\Gamma(\mathrm{B}^0\to \bar{f})\right)}. \tag{6.23}$$

It is useful make the following definitions:

$$\text{the production asymmetry, } A_p \equiv \frac{N-\bar{N}}{N+\bar{N}}, \tag{6.24}$$

$$\text{the detection asymmetry, } A_c \equiv \frac{\epsilon_f-\bar{\epsilon}_f}{\epsilon_f+\bar{\epsilon}_f}. \tag{6.25}$$

Equivalently one can define the following parameters, as in [54]:

$$\delta_p \equiv \frac{\bar{N}}{N}-1, \qquad \delta_c \equiv \frac{\bar{\epsilon}_f}{\epsilon_f}-1, \tag{6.26}$$

which are related to the production and detection asymmetries by

$$A_p = \frac{-\delta_p}{2+\delta_p}, \qquad \delta_p = \frac{-2A_p}{1+A_p}, \tag{6.27}$$

$$A_c = \frac{-\delta_c}{2+\delta_c}, \qquad \delta_c = \frac{-2A_c}{1+A_c}. \tag{6.28}$$

Further we define

$$\begin{array}{rcccll} A'_p & \equiv & -\frac{\delta_p+\frac{1}{2}\delta_p\delta_c}{2+\delta_p+\delta_c} & = & \frac{A_p}{1-A_pA_c} & \text{which is } \mathcal{O}(\delta) \\ A'_c & \equiv & -\frac{\delta_c+\frac{1}{2}\delta_p\delta_c}{2+\delta_p+\delta_c} & = & \frac{A_c}{1-A_pA_c} & \text{which is } \mathcal{O}(\delta) \\ \delta A \equiv A'_p - A'_c & = & \frac{\delta_c-\delta_p}{1+\delta_p+\delta_c} & = & \frac{A_p-A_c}{1-A_pA_c} & \text{which is } \mathcal{O}(\delta) \\ D & \equiv & \frac{\delta_p\delta_c}{2+\delta_p+\delta_c} & = & \frac{A_pA_c}{1-A_pA_c} & \text{which is } \mathcal{O}\big(\delta^2\big) \end{array} \tag{6.29}$$

where we also indicate which order in the small parameter δ each expression is, where $\delta \equiv \max(|\delta_p|, |\delta_c|)$, and we assume that δ_c and δ_p are of similar magnitude. With these definitions we find the following relation for the time-dependent flavour-specific asymmetry $A_{fs}(t)$:

$$A_{fs}(t) = \frac{\frac{a_{fs}}{2} + A'_c - \left[\frac{a_{fs}}{2} - A'_p\right] e^{-\frac{1}{2}\sigma_t^2\left((\Delta m)^2+\left(\frac{1}{2}\Delta\Gamma\right)^2\right)} \frac{\cos\left(\Delta m\left(t-\sigma_t^2\Gamma\right)\right)}{\cosh\left(\frac{1}{2}\Delta\Gamma\left(t-\sigma_t^2\Gamma\right)\right)}}{1 + D - \delta A\frac{a_{fs}}{2} + \left[D + \delta A\frac{a_{fs}}{2}\right] e^{-\frac{1}{2}\sigma_t^2\left((\Delta m)^2+\left(\frac{1}{2}\Delta\Gamma\right)^2\right)} \frac{\cos\left(\Delta m\left(t-\sigma_t^2\Gamma\right)\right)}{\cosh\left(\frac{1}{2}\Delta\Gamma\left(t-\sigma_t^2\Gamma\right)\right)}} \tag{6.30}$$

Neglecting all terms $\mathcal{O}\left(a_{fs}^2\right)$ and higher, as well as terms that contain at least one factor a_{fs} and one factor of $\mathcal{O}\big(\delta^2\big)$ and higher (e.g. $\mathcal{O}\big(a_{fs}\delta^2\big)$, $\mathcal{O}\big(a_{fs}\delta^3, \ldots\big)$) we find:

$$A_{fs}(t) = \frac{\left[\frac{a_{fs}}{2} + A_c\right] - \left[\frac{a_{fs}}{2} - A_p\right] e^{-\frac{1}{2}\sigma_t^2\left((\Delta m)^2+\left(\frac{1}{2}\Delta\Gamma\right)^2\right)} \frac{\cos\left(\Delta m\left(t-\sigma_t^2\Gamma\right)\right)}{\cosh\left(\frac{1}{2}\Delta\Gamma\left(t-\sigma_t^2\Gamma\right)\right)}}{1 + A_cA_pe^{-\frac{1}{2}\sigma_t^2\left((\Delta m)^2+\left(\frac{1}{2}\Delta\Gamma\right)^2\right)} \frac{\cos\left(\Delta m\left(t-\sigma_t^2\Gamma\right)\right)}{\cosh\left(\frac{1}{2}\Delta\Gamma\left(t-\sigma_t^2\Gamma\right)\right)}} \tag{6.31}$$

If we also ignored terms $\mathcal{O}\big(\delta^2\big)$ and higher, in which case $A'_p \approx A_p \approx -\delta_p/2$ and $A'_c \approx A_c \approx -\delta_c/2$, we would recover the expression given in [54]. However, since we expect the production asymmetry to be $\mathcal{O}(\%)$, it is unlikely that $\delta^2 \ll a_{fs}$. For the case that there is no detection asymmetry, the above expression simplifies considerably:

$$A_{fs}(t) = \left[\frac{a_{fs}}{2}\right] - e^{-\frac{1}{2}\sigma_t^2\left((\Delta m)^2+\left(\frac{1}{2}\Delta\Gamma\right)^2\right)} \left[\frac{a_{fs}}{2} - A_p\right] \frac{\cos\left(\Delta m\ \left(t-\sigma_t^2\Gamma\right)\right)}{\cosh\left(\frac{1}{2}\Delta\Gamma\left(t-\sigma_t^2\Gamma\right)\right)} \quad \text{for } A_c = 0 \tag{6.32}$$

Similarly, for the case that there is no production asymmetry we get:

$$A_{fs}(t) = \left[\frac{a_{fs}}{2} + A_c\right] - e^{-\frac{1}{2}\sigma_t^2\left((\Delta m)^2+\left(\frac{1}{2}\Delta\Gamma\right)^2\right)} \left[\frac{a_{fs}}{2}\right] \frac{\cos\left(\Delta m\ \left(t-\sigma_t^2\Gamma\right)\right)}{\cosh\left(\frac{1}{2}\Delta\Gamma\left(t-\sigma_t^2\Gamma\right)\right)} \quad \text{for } A_p = 0 \tag{6.33}$$

So for a situation with no production asymmetry (e.g. an e^+e^- or a $p\bar{p}$ collider), one can in principle fit both at the same time the detection asymmetry and a_{fs}.

However, the LHC is a proton-proton collider with six valence quarks and zero valence antiquarks in the the initial state. Therefore different production rates of B^0 and $\overline{\mathrm{B}}^0$ are expected. This leads to a non-zero production asymmetry, estimated to be of $\mathcal{O}(1\%)$ [59].

For the purpose of the MC study presented we assume $A_p = 1\%$, that the detection asymmetry is well-known and present the statistical uncertainty for a simultaneous fit to the production asymmetry and a_{fs}. For simplicity, we assume $A_C = 0$, the effects of non-zero A_C are discussed in section 6.5.4.

6.3 Current Measurements of a_{fs}^s

At the Tevatron, the CDF and DØ collaborations measure A_{SL}^s indirectly. They examine the di-muon sample which contains a mixture of B_s^0 and B_d^0 decays and measure the time-integrated asymmetry of the rate of same charge muon pairs Γ^{++} and Γ^{--} [60, 61, 62]. The CDF and DØ experiments measure [61, 62] :

$$\text{DØ-indirect:} \quad A_{SL}^s = -(6.4 \pm 10.1) \times 10^{-3} \tag{6.34}$$

$$\text{CDF-indirect:} \quad A_{SL}^s = -(20 \pm 21(stat) \pm 16(syst) \pm 9(inputs)) \times 10^{-3}. \tag{6.35}$$

Recently DØ has also presented a time-integrated direct measurement of A_{SL}^s in the channel $B_s^0 \to D_s^{\pm}\mu^{\mp}\nu_\mu$ [60]. After correcting for detection asymmetry, they measure:

$$\text{DØ-direct:} \quad A_{SL}^s = \frac{N(\mu^+\mathrm{D_s^+}) - N(\mu^-\mathrm{D_s^+})}{N(\mu^+\mathrm{D_s^-}) + N(\mu^-\mathrm{D_s^+})} = a_{fs}^s \tag{6.36}$$

where $N(\mu^{\pm}\mathrm{D_s}^{\mp})$ is the number of time-integrated $\mathrm{B_s^0} \to \mathrm{D_s}^{\pm}\mu^{\mp}\nu\mu$ decays.

This measurement has relatively small systematic contributions, in comparison to the di-lepton sample, however the total error is dominated by the statistical error. For $\sim 27\,\mathrm{K}$ events recorded in $\sim 1\,\mathrm{fb}^{-1}$, with a B/S ~ 0.2, DØ obtain [61]:

$$\text{DØ-direct:} \quad A_{SL}^s = (2.45 \pm 1.93(\mathrm{stat}) \pm 0.35(\mathrm{syst})) \times 10^{-2}. \tag{6.37}$$

6.4 Monte Carlo Study

A fast Monte Carlo generator was written with which it is possible to generate datasets based on the parameters defined in section 6.2.5.

6.4.1 Physics Datasets

Two physics channels were chosen with which to investigate the potential to measure a_{fs} at LHCb, they are:

- $\mathrm{B_s^0} \to \mathrm{D_s}\mu\nu_\mu$ and
- $\mathrm{B_s^0} \to \mathrm{D_s}\pi$.

Both channels have clear experimental signatures and their selection methods at LHCb are well documented.

Simulation studies based on Monte Carlo samples show that a total of 140 thousand $\mathrm{B_s^0} \to \mathrm{D_s}\pi$ events are expected to be reconstructed in $2\,\mathrm{fb}^{-1}$ of data under nominal conditions. The reconstructed sample has a lifetime resolution of 36 fs [56].

The $\mathrm{B_s^0} \to \mathrm{D_s}\mu\nu$ decay reconstructs the $\mathrm{D_s}$ using the $K^+K^-\pi^\pm$ final state. Using the selection methods in [55], one million events are expected to be reconstructed in a nominal year. The presence of a neutrino in the final state means that the decay can't be fully reconstructed and the momentum of the missing neutrino must be corrected for. Imposing a cut on the reconstructed mass of the $\mathrm{D_s}\mu$ combination results in two sub-samples with different lifetime resolutions. Requiring $m\,(\mathrm{D_s}\mu) > 4.5\,\mathrm{GeV}$ produces a sub-sample of 185 thousand events with an average lifetime resolution of 121 fs. The remaining 815 thousand events have an average lifetime resolution of 270 fs [55].

6.4.2 Fast Monte Carlo

The default parameter set is based upon the $\mathrm{B_s^0} \to \mathrm{D_s}\mu\nu$ sub-sample with the best lifetime resolution and is henceforth referred to as the "Standard" settings. The parameters and their default values are listed in table 6.1.

A dataset of observed decay states and proper times is created using standard Monte Carlo [63] methods based on the time-dependent rates defined in 6.12 to 6.15. In order to model the detector efficiency when measuring small lifetimes an acceptance function

Parameter	Symbol	Default value
Production asymmetry	A_P	0.01
Detector asymmetry	A_C	0.00
CP asymmetry due to mixing	a_{fs}	0.005
Acceptance function parameter	β	1.29 ps^{-1}
Average lifetime resolution of the dataset	σ_t	0.120 ps
Number of events required	N	185000
Minimum decay time measurable	t_0	0.60 ps
Maximum decay time expected	$t_{\max}$	15 ps
Mass difference of the two physical states	Δm	17.5 ps^{-1}
Lifetime difference of the two physical states	$\Delta\Gamma$	0.071 ps^{-1}
Average lifetime of the two physical states	Γ	0.71 ps^{-1}

Table 6.1: The standard set of parameters used in the Monte Carlo.

is used. The acceptance function, $\eta(t)$, takes the form [10]:

$$\begin{aligned} \eta(t) = & \quad \frac{(\beta(t-t_0))^3}{1+(\beta(t-t_0))^3} & \text{for } t \geq t_0 \\ \eta(t) = & \quad 0 & \text{for } t < t_0. \end{aligned} \tag{6.38}$$

6.4.3 Likelihood Fit

After generating a dataset using the MC generator, we extract the parameters of the asymmetry probability density function by performing an unbinned likelihood fit on the data using MINUIT [47]. The likelihood function is simply the product of the probabilities of observing each decay in our dataset:

$$L(\theta) = \prod_{i=1}^{n} P(\text{decay}_i|\theta), \tag{6.39}$$

where the vector θ represents all the parameters in the pdf. The likelihood is therefore a function of the pdf parameters, θ_j.

The probability of observing the decay (B or $\overline{\mathrm{B}}$) $\rightarrow f$ rather than (B or $\overline{\mathrm{B}}$) $\rightarrow \bar{f}$ is obtained from the time-dependent asymmetry, A_{fs}:

$$P\left(f\left(t\right)|t\right) = \frac{1}{2}\left(1 + A_{fs}\left(t\right)\right), \tag{6.40}$$

and similarly for (B or $\overline{\mathrm{B}}$) $\rightarrow \bar{f}$ rather than (B or $\overline{\mathrm{B}}$) $\rightarrow f$:

$$P\left(\overline{f}\left(t\right)|t\right) = \frac{1}{2}\left(1 - A_{fs}\left(t\right)\right). \tag{6.41}$$

We can determine the values of the pdf parameters, θ_j, by maximising L. In practise, we actually maximise the log-likelihood, Λ:

$$\Lambda\left(\theta\right) = \log\left(L\left(\theta\right)\right) = \sum_{i=1}^{n} \log\left(P\left(\mathrm{decay}_i|\theta\right)\right), \tag{6.42}$$

because it lends itself more easily to computation.

6.5 Analysis of Results

A number of datasets were considered in addition to the three mentioned in section 6.4 in order to systematically study the parameter space. The settings of the additional datasets are based upon those of the $\mathrm{B_s^0} \rightarrow \mathrm{D_s}\pi$ channel, these are also referred to as the "standard settings". A summary of the average fit results and parameter resolution is presented in table 6.6. Unless otherwise indicated, all results quoted assume zero detection asymmetry. Non-zero detection asymmetry is discussed in section 6.5.4.

6.5.1 General Fit Properties

Plotting the fit value residual divided by the fit error for a large number of identical MC experiments forms a pull distribution [64] i.e., the histogram of

$$\frac{x_i - x_{\mathrm{input}}}{\sigma_i} \tag{6.43}$$

forms a pull distribution, where x_i is the fit output value, x_{input} is the parameter input and σ_i is the fit error provided by MINUIT. The pull distribution for each parameter

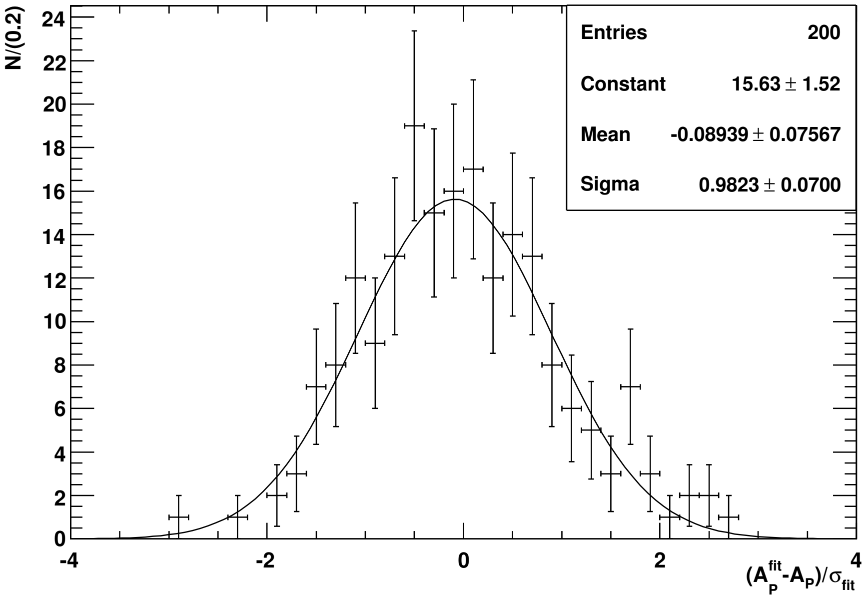

Figure 6.1: A_p pull distribution for the $\mathrm{B_s^0} \to \mathrm{D_s}\mu\nu(> 4.5\,\mathrm{GeV})$ dataset.

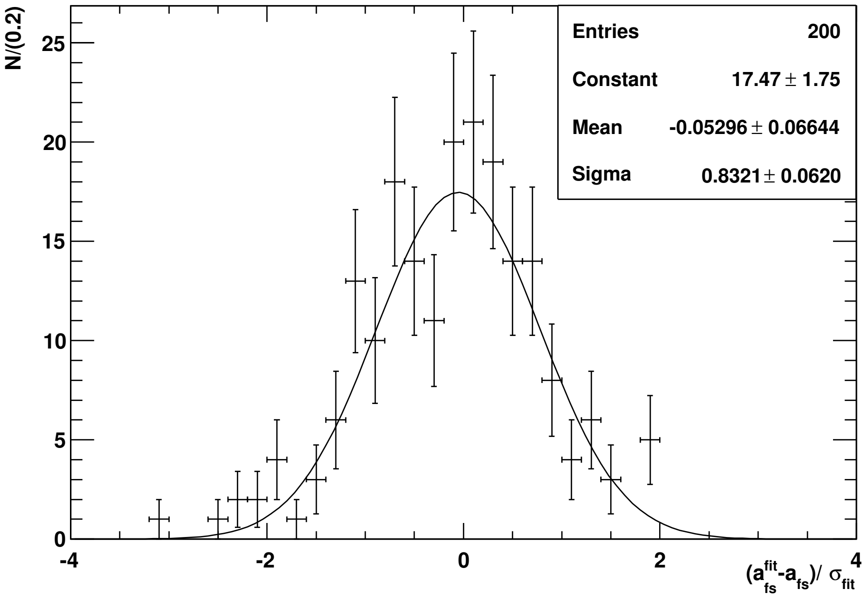

Figure 6.2: a_{fs} pull distribution for the $\mathrm{B_s^0} \to \mathrm{D_s}\mu\nu(> 4.5\,\mathrm{GeV})$ dataset.

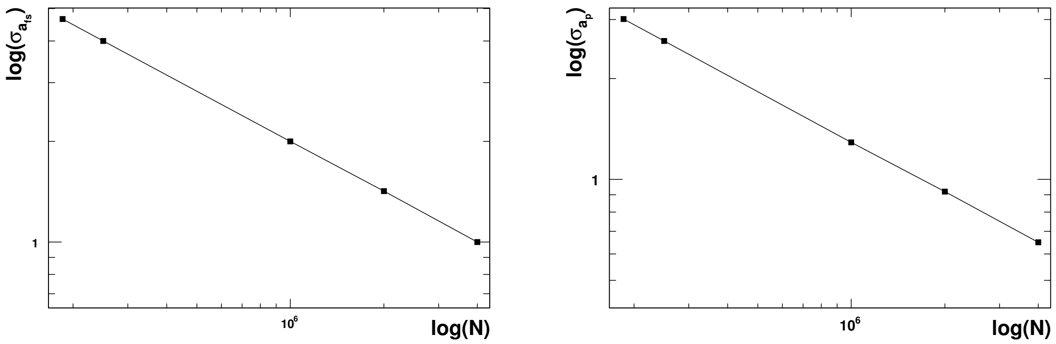

Figure 6.3: Variation of the observed A_P resolution (left) and a_{fs} resolution (right) with the size of the dataset. Both scale with $1/\sqrt{N}$.

forms a Gaussian with width one and mean zero if the data generation and parameter fitting is “well behaved”.

Pull studies were performed with at least 200 experiments for each dataset considered. The pull distributions were found to be consistent with a mean of zero and a width of one. Examples are given in figures 6.1 and 6.2 for dataset $\mathrm{B_s^0} \rightarrow \mathrm{D_s}\mu\nu(> 4.5\,\mathrm{GeV})$.

The variation of fit parameter resolution with N is shown in figure 6.3. Both graphs show that the observed resolution scales with $1/\sqrt{N}$.

6.5.2 Varying Lifetime Resolution

Figures 6.4 to 6.7 show example decay rate and asymmetry distributions for selected settings. The distributions in figures 6.4 and 6.6 were created using a lifetime resolution of 36 fs. Figures 6.5 and 6.7 show the same distributions created using a resolution of 120 fs. Decreasing the lifetime resolution effectively “washes out” the oscillations, thereby decreasing our sensitivity to any parameter proportional to the cosine term in equation 6.31. The precision on A_P is therefore highly dependent on lifetime resolution. The observed fit parameter resolution for selected values of lifetime resolution is given in table 6.2. The precision on a_{fs} remains constant for all lifetime resolutions whereas we lose resolution on A_P for large lifetime resolutions.

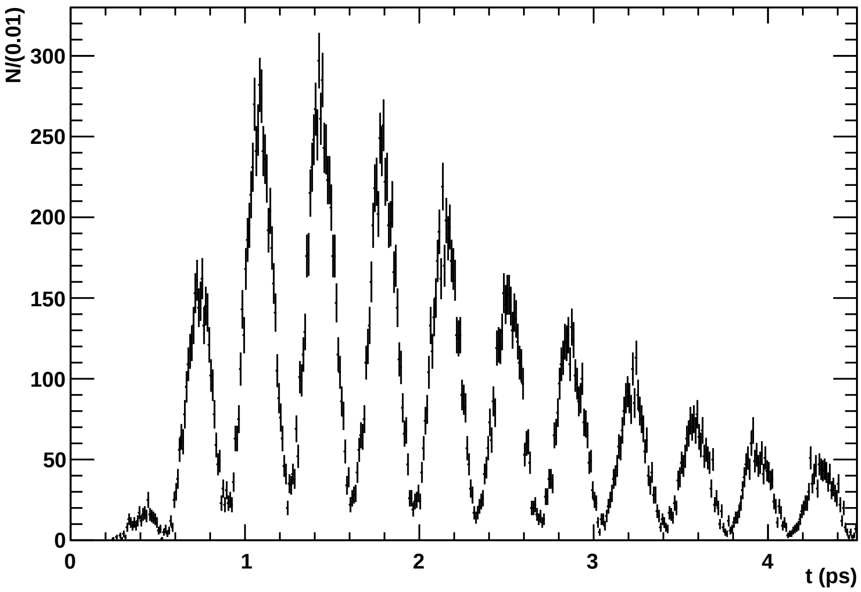

Figure 6.4: $B_s^0 \to D_s\pi$ decay distribution generated using the number of events expected in $2\,\mathrm{fb}^{-1}$ and a lifetime resolution of 36 fs.

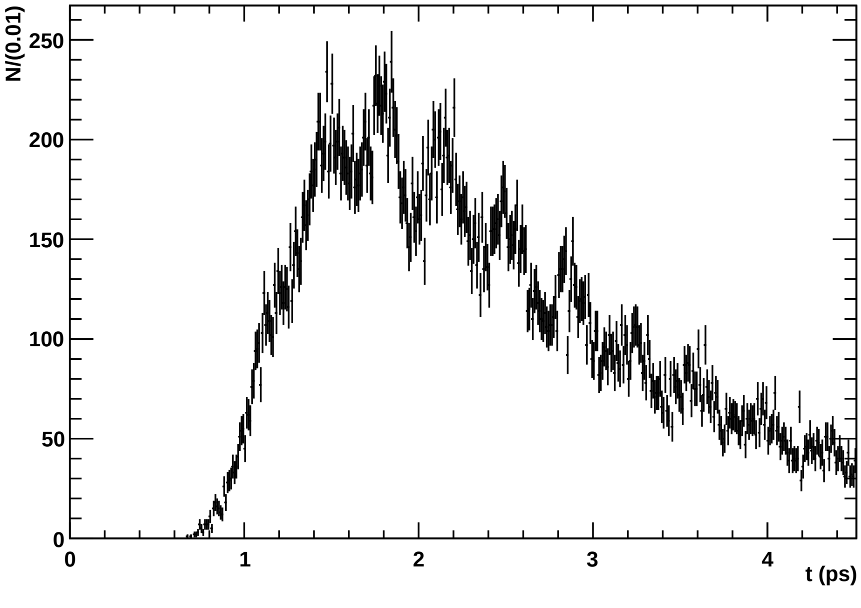

Figure 6.5: $B_s^0 \to D_s^- \mu^+ \nu_\mu$ decay distribution generated using the number of events expected in $2\,\mathrm{fb}^{-1}$ and a lifetime resolution of 120 fs.

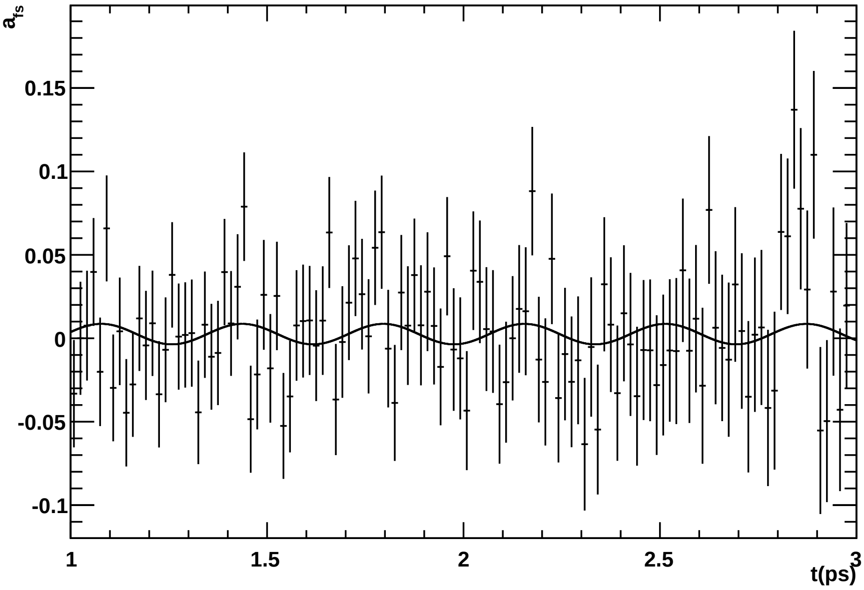

Figure 6.6: An histogram of the time-dependent asymmetry data generated using the standard settings with a lifetime resolution of 36 fs, the analytic asymmetry function is overlaid.

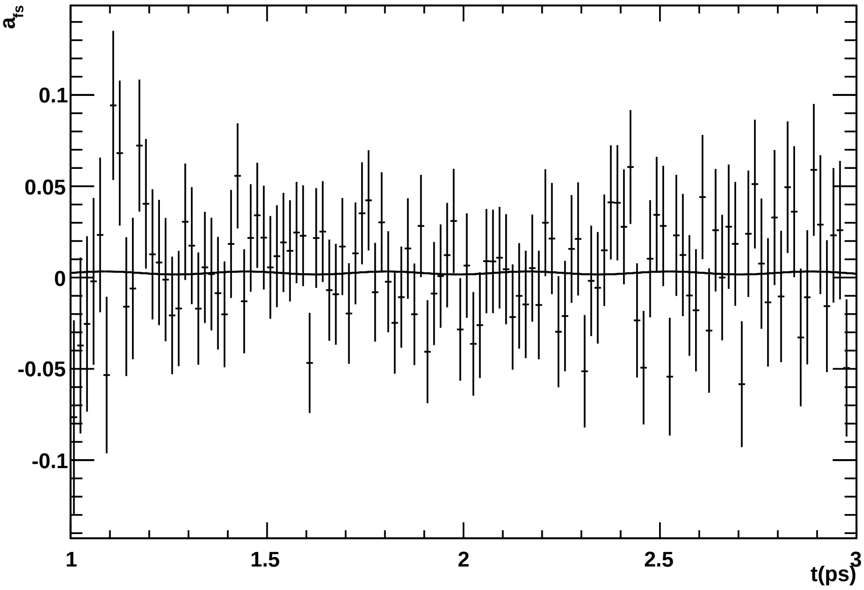

Figure 6.7: An histogram of the time-dependent asymmetry data generated using the standard settings (lifetime resolution of 120 fs) with the analytic asymmetry function overlaid.

Dataset	Resolution/ps	A_P resolution	a_{fs} resolution
$\mathrm{Std}_{\sigma=0\,\mathrm{fs}}$	0.000	0.40	4.65
$\mathrm{Std}_{\sigma=60\,\mathrm{fs}}$	0.060	0.62	4.65
$\mathrm{Std}_{\sigma=120\,\mathrm{fs}}$	0.120	3.01	4.65
$\mathrm{Std}_{\sigma=133\,\mathrm{fs}}$	0.133	4.97	4.65
$\mathrm{Std}_{\sigma=320\,\mathrm{fs}}$	0.320	No Resolution	4.65

Table 6.2: Observed a_{fs} and A_P resolution for various lifetime resolutions.

Dataset $\mathrm{B_s^0} \to \ldots$	Resolution/ps	$\sigma_{A_p}/1\mathrm{M}$	$\sigma_{A_p}/2\,\mathrm{fb}^{-1}$	$\sigma_{a_{fs}}/1\mathrm{M}$	$\sigma_{a_{fs}}/2\,\mathrm{fb}^{-1}$
$\mathrm{D_s}\mu\nu(< 4.5\,\mathrm{GeV})$	0.270	None	None	0.20%	0.22%
$\mathrm{D_s}\mu\nu(> 4.5\,\mathrm{GeV})$	0.120	1.29%	3.01%	0.20%	0.47%
$\mathrm{D_s}\pi$	0.036	0.20%	0.55%	0.20%	0.54%

Table 6.3: A_p and a_{fs} resolution from selected datasets after 1M events and $2\,fb^{-1}$ at LHCb respectively.

The decreased sensitivity to the cosine term reduces the correlation between the fit parameters. The likelihood surfaces in figures 6.8 and 6.10 highlight this rather well. The plots show contours of equal Λ for individual fits to the three physics datasets. The axes of each plot are centred on the parameter fit value and span $\pm 3\sigma$. As σ_t increases, the relative size of the A_P axis increases dramatically and the contours become more circular, i.e. we lose all sensitivity to A_P when σ_t is large.

6.5.3 Sensitivity to a_{fs}

In section 6.5.2 it was shown that the measurement of the production asymmetry is highly dependent on the lifetime resolution. Both $\sigma_{a_{fs}}$ and σ_{A_p} are largely independent of the other input parameters, and scale with $1/\sqrt{N}$. Table 6.3 contains a summary of the obtained resolution per million events for each physics dataset and the corresponding resolutions when scaled to LHCb yearly yields.

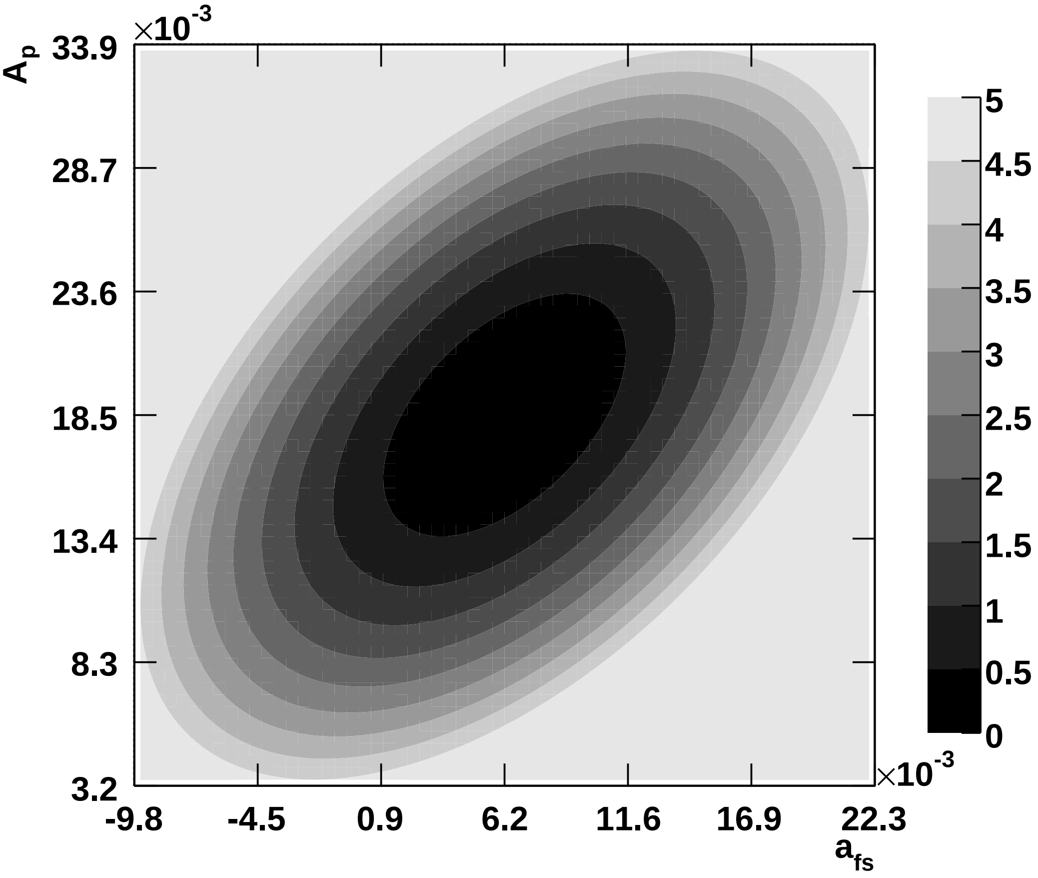

Figure 6.8: Likelihood surface for a fit to $B_s^0 \rightarrow D_s\pi$ data. The horizontal and vertical axes are centred on the fitted value of a_{fs} and A_P respectively. Each axis covers $\pm 3\sigma$. For a lifetime resolution of 0.036 ps the fit parameters are slightly correlated.

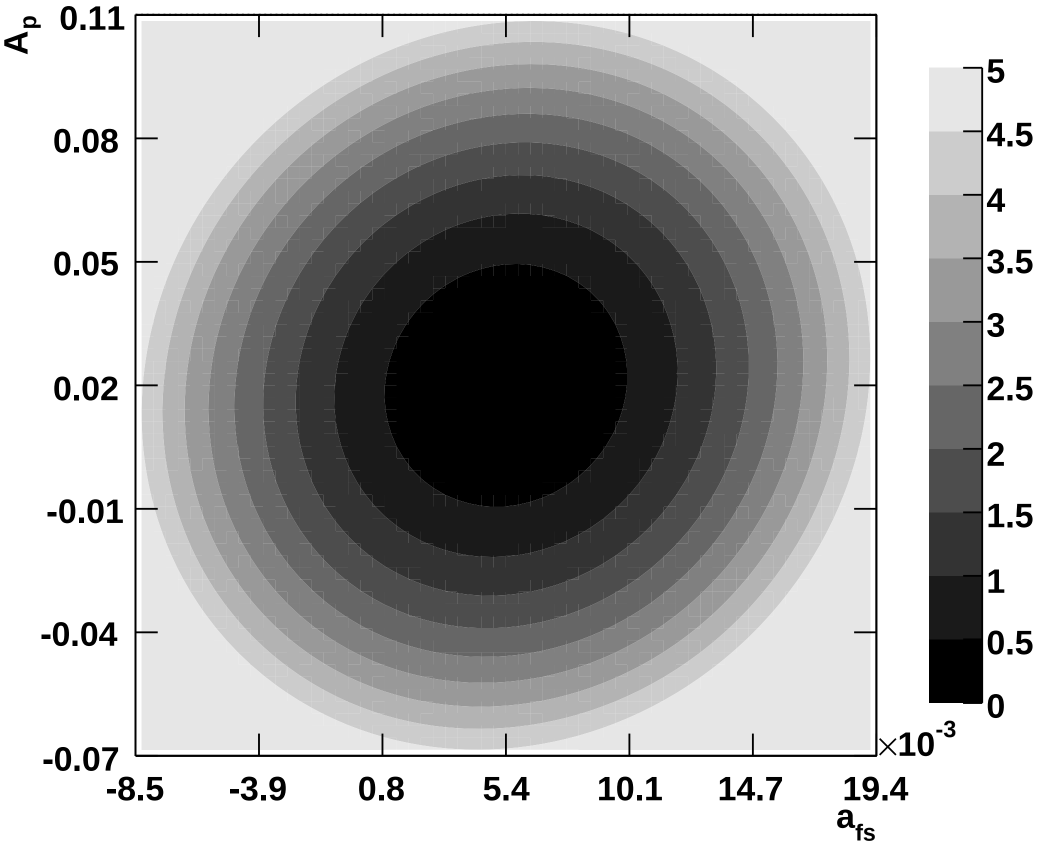

Figure 6.9: Likelihood surface for a fit to the $B_s^0 \to D_s\mu\nu(> 4.5\,\mathrm{GeV})$ dataset. Both axes are centred on the fitted value of a_{fs} (horizontal) and A_P (vertical). Each axis covers $\pm3\sigma$ for the relevant parameter. The parameters are very slightly correlated.

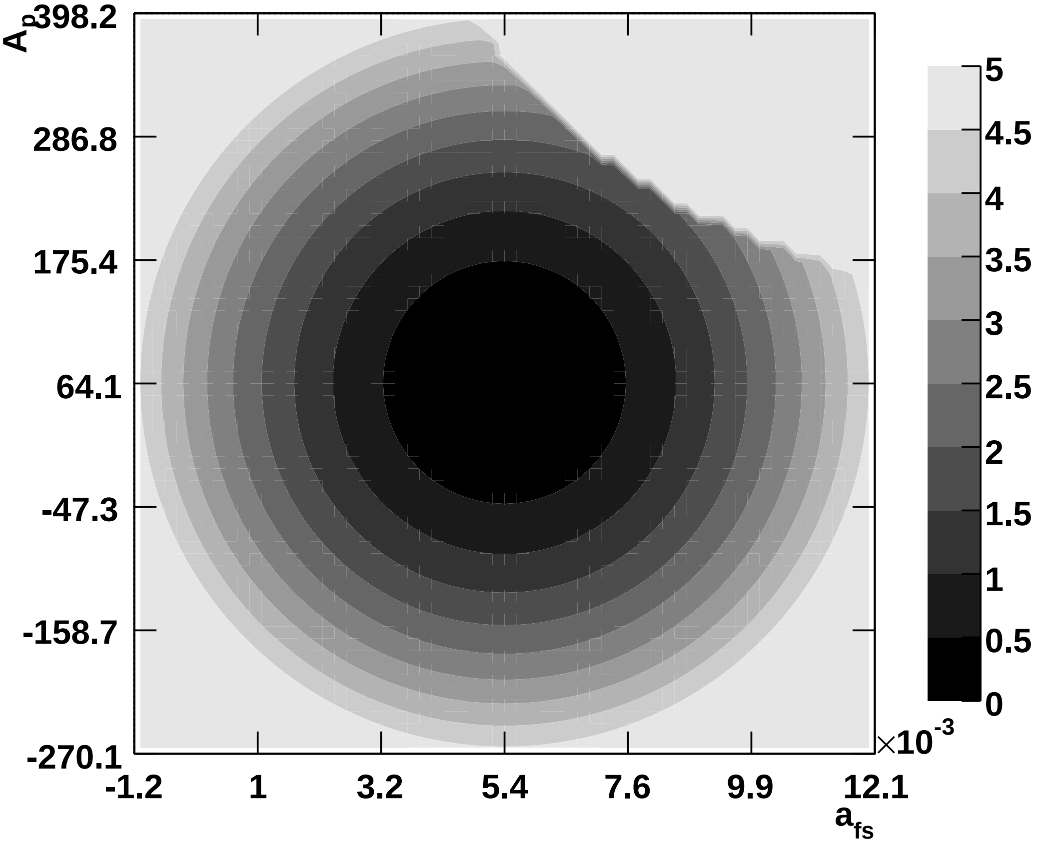

Figure 6.10: Likelihood surface for a fit to the $B_s^0 \to D_s\mu\nu(< 4.5\,\mathrm{GeV})$ dataset. The axes of both plots are centred on the fitted value of a_{fs} (horizontal) and A_P (vertical). Each axis covers $\pm 3\sigma$ for the relevant parameter. The parameters are uncorrelated because the fit is insensitive to A_P c.f. the A_P scale in figure 6.8. (Note that the majority of this plot, including the upper-right region, covers unphysical regions of the parameter space.)

Dataset	Resolution/ps	A_P Fit Result	a_{fs} Fit Result
$\mathrm{B_s^0} \to \mathrm{D_s}\mu\nu$	0.270	No Resolution	$0.46\% \pm 0.22\%$
$\mathrm{B_s^0} \to \mathrm{D_s}\mu\nu$	0.120	$0.86\% \pm 3.01\%$	$0.54\% \pm 0.47\%$
$\mathrm{B_s^0} \to \mathrm{D_s}\pi$	0.030	$0.96\% \pm 0.53\%$	$0.52\% \pm 0.54\%$

Table 6.4: Effect of non-zero (but well-known) charge detection asymmetry on fit parameter resolution for the three physics datasets. A_C was set to 2%.

6.5.4 Fit Parameter Resolution with $A_C \neq 0$

Ignoring terms of order a_{fs}^2 and higher as well as $a_{fs}\delta^2$ and higher, as in equation 6.31 and used throughout this note, the time-independent part of the asymmetry is given by

$$A_{\text{time-independent}} = \frac{a_{fs}}{2} + A_C \tag{6.44}$$

and the only effect of a precisely known charge-detection asymmetry is to add a constant to the measurement of a_{fs}. If we included higher order terms, we would also find that a non-zero A_C introduces a slight dependence of the time-independent part on A_P, but this effect is $\mathcal{O}\big(a_{fs}\delta^2\big)$, and can safely be ignored.

Table 6.4 shows results of fits A_P and a_{fs} assuming a precisely known charge detection asymmetry of 2% for three Monte Carlo samples according to the three physics datasets considered. Fits were performed to the samples with good time resolution ($\sigma_t = 36\,\text{fs}$ and $\sigma_t = 120\,\text{fs}$) without any constraint on A_P; in the fit to the sample with $\sigma_t = 270\,\text{fs}$ we constrained A_P to $1\% \pm 3\%$. We find that the resolutions on a_{fs} and A_P for $A_C = 2\%$ are compatible with those observed for $A_C = 0$.

6.5.5 Simultaneous Fits to A_P and A_C Assuming $a_{fs}^{s,SM}$

The size of the Standard Model prediction of a_{fs} is small, $\mathcal{O}(a_{fs}^{s,SM}) = 10^{-5}$, even in comparison to the expected production and detection asymmetries. Performing a simultaneous fit of A_P and A_C assuming $a_{fs} = 0$ we instead measure $A_P - \frac{a_{fs}}{2}$ and $A_C + \frac{a_{fs}}{2}$ respectively. A measurement of the production asymmetry with this technique

Dataset	A_C	$\sigma_{A_P}/10^{-2}$	$\sigma_{A_C}/10^{-3}$
Std	0.000	3.00	2.33
$\mathrm{Std}_{A_C\neq 0}$	0.005	3.00	2.33
$\mathrm{Std}_{A_C\neq 0}$	0.010	3.00	2.33
$\mathrm{Std}_{A_C\neq 0}$	0.015	3.00	2.33
$\mathrm{Std}_{A_C\neq 0}$	0.020	3.00	2.33
$\mathrm{Std}_{A_C\neq 0}$	0.025	3.00	2.34
$\mathrm{Std}_{A_C\neq 0}$	0.050	3.00	2.32
$\mathrm{Std}_{A_C\neq 0}$	0.100	3.01	2.31

Table 6.5: Fit resolutions obtained when fitting A_P and A_C to the standard settings with varying A_C and assuming $a_{fs} = 0$.

is therefore possible even without external constraints on the charge detection asymmetry as long as a^s_{fs} is small compared to the required precision on the production asymmetry.

Table 6.5 contains the observed precision on A_C and A_P for simultaneous fits to data generated using the standard settings assuming $a_{fs} = 0$. The precision on both A_C and A_P is largely unaffected for $A_C \in [0, 0.1]$.

6.5.6 Future Studies

The analysis presented uses a fast MC to generate data based on the selection algorithms presented in [55] and [56]. Future studies should take advantage of the comprehensive simulation and analysis tools provided by the LHCb software framework (Section 2.11) to better understand the effects of background events passing the selections and detector-specific effects.

6.6 Conclusions

The ability of LHCb to perform a measurement of the parameter a^s_{fs} (equivalent to $2 \cdot A^s_{sl}$), which parameterises CP violation in $\mathrm{B^0_s}$ mixing, is investigated. a^s_{fs} is extracted from time-dependent, untagged decay-rate asymmetries in decays to semileptonic and hadronic flavour eigenstates, as proposed in [65]. In the expression for the time-dependent asymmetry, acceptance effects due to the LHCb trigger cancel. The measured asymmetry depends on a^s_{fs} itself, the B-production asymmetry A_P and the charge detection asymmetry A_C. Two of these three parameters can be extracted simultaneously, the third needs to be measured externally.

We performed a simultaneous fit to a^s_{fs} and A_P in a Monte Carlo study. The detection asymmetry was assumed to be well-known and background effects were ignored. With this we find a statistical precision on a^s_{fs} of $\sim 0.2\%$ for 1 M events for all values of a^s_{fs}. For $2\,\mathrm{fb}^{-1}$ of LHCb data, this corresponds to $\sigma_{a^s_{fs}} \sim 0.2\%$ in the $\mathrm{D_s} \rightarrow \mathrm{D_s}\mu\nu$ channel, and $\sigma_{a^s_{fs}} \sim 0.5\%$ for $\mathrm{B^0_s} \rightarrow \mathrm{D_s}\pi$. This represents a factor of ten improvement compared to the current direct measurement by DØ.

Dataset	Resolution/ps	$\Delta\Gamma/ps^{-1}$	t_0/ps	N_{evts}	A_P	a_{fs}	A_P Fit Result/10^{-2}	a_{fs} Fit Result/10^{-3}
$B_s \to D_s\mu\nu$	0.270	0.071	1.50	815000	0.01	0.005	No resolution	5.05 ± 2.22
$B_s \to D_s\mu\nu$	0.120	0.071	0.60	185000	0.01	0.005	0.98 ± 3.01	5.12 ± 4.65
$B_s \to D_s\pi$	0.036	0.071	0.18	140000	0.01	0.005	1.07 ± 0.53	5.40 ± 5.35
Std settings	0.120	0.071	0.60	185000	0.01	0.005	0.98 ± 3.01	5.12 ± 4.65
$\text{Std}_{\Delta\Gamma=0\%\times\Gamma}$	0.120	0.000	0.60	185000	0.01	0.005	0.76 ± 2.99	6.91 ± 4.65
$\text{Std}_{\Delta\Gamma=5\%\times\Gamma}$	0.120	0.036	0.60	185000	0.01	0.005	1.18 ± 3.00	6.03 ± 4.65
$\text{Std}_{\Delta\Gamma=15\%\times\Gamma}$	0.120	0.107	0.60	185000	0.01	0.005	0.76 ± 3.03	6.59 ± 4.65
$\text{Std}_{\sigma=0\text{ fs}}$	0.000	0.071	0.60	185000	0.01	0.005	0.99 ± 0.40	5.96 ± 4.65
$\text{Std}_{\sigma=60\text{ fs}}$	0.060	0.071	0.60	185000	0.01	0.005	1.12 ± 0.62	6.48 ± 4.65
$\text{Std}_{\sigma=133\text{ fs}}$	0.133	0.071	0.60	185000	0.01	0.005	1.12 ± 4.97	6.06 ± 4.65
$\text{Std}_{\sigma=320\text{ fs}}$	0.320	0.071	1.60	185000	0.01	0.005	No resolution	8.51 ± 4.64
$\text{Std}_{a_{fs}=0.00}$	0.120	0.071	0.60	185000	0.01	0.000	0.87 ± 3.01	0.44 ± 4.65
$\text{Std}_{a_{fs}=0.01}$	0.120	0.071	0.60	185000	0.01	0.001	0.71 ± 3.01	2.89 ± 4.65
$\text{Std}_{a_{fs}=0.05}$	0.120	0.071	0.60	185000	0.01	0.005	0.98 ± 3.01	5.12 ± 4.65
$\text{Std}_{a_{fs}=0.10}$	0.120	0.071	0.60	185000	0.01	0.010	1.03 ± 3.01	12.4 ± 4.65
$\text{Std}_{a_{fs}=0.15}$	0.120	0.071	0.60	185000	0.01	0.015	0.69 ± 3.01	16.2 ± 4.65
$\text{Std}_{A_P=0.00}$	0.120	0.071	0.60	185000	0.00	0.005	0.01 ± 3.01	6.96 ± 4.65
$\text{Std}_{A_P=0.02}$	0.120	0.071	0.60	185000	0.02	0.005	1.03 ± 3.01	6.23 ± 4.65
$\text{Std}_{A_P=0.05}$	0.120	0.071	0.60	185000	0.05	0.005	5.05 ± 3.01	6.42 ± 4.65
$B_s \to D_s\mu\nu_{A_C=2\%}$	0.270	0.071	1.50	815000	0.01	0.005	No resolution	4.97 ± 2.22
$B_s \to D_s\mu\nu_{A_C=2\%}$	0.120	0.071	0.60	185000	0.01	0.005	0.86 ± 3.01	5.38 ± 4.65
$B_s \to D_s\pi_{A_C=2\%}$	0.036	0.071	0.18	140000	0.01	0.005	0.96 ± 0.53	5.23 ± 5.35

Table 6.6: Settings used in each scenario with the corresponding A_P and a^s_{fs} resolution. Scenarios investigated include the physics scenarios mentioned in Section 6.4 and the systematic variation of the input parameters from a "Standard" set based upon the expected $\mathrm{B}^0_\mathrm{s} \to \mathrm{D_s}\mu\nu$ lifetime resolution.

Chapter 7

Conclusions

The main Monte Carlo generator used by the LHCb collaboration is Pythia. Orbitally excited meson states, which provide a mechanism to identify the flavour of a meson, were introduced to the LHCb generator settings. An increase in minimum bias event multiplicity was observed at the centre of mass energies used to determine the value of the Pythia parameter, $p_{\perp_{\mathrm{Min}}}$. This parameter controls the multiple interaction model implemented in Pythia and represents an effective cutoff below which the parton-parton cross section is no longer given by purturbative QCD.

The $p_{\perp_{\mathrm{Min}}}$ parameter of Pythia v6.226 was re-tuned using minimum bias multiplicity data from the UA5 and CDF experiments at centre of mass energies in the range $\sqrt{s} =$ 53 to 1800 GeV. Values of $p_{\perp_{\mathrm{Min}}}$ which reproduce the observed central multiplicity data at each $\sqrt{s}$ were obtained. A fit to the obtained values was performed using the energy dependence of $p_{\perp_{\mathrm{Min}}}$ suggested by Pythia. An extrapolation of $p_{\perp\mathrm{Min}}$ to LHC energies gives $P^{LHC}_{\perp_{\mathrm{Min}}} = 3.39 \pm 0.16$ with a corresponding central multiplicity of $\langle n_{ch} \rangle |_{\eta=0} = 6.37 \pm 0.52$ in minimum bias events. The tuned central multiplicity is consistent with the phenomenological extrapolation of 6.27 ± 0.50.

The RICH 1 prototype spherical beryllium mirror is characterised and factors affecting the quality of the optical surface identified. It is the first beryllium-glass mirror ever fabricated with large geometrical dimensions ($\sim 400\,\mathrm{mm} \times 660\,\mathrm{mm}$) and a thin beryllium substrate ($\sim 3.8\,\mathrm{mm}$). The mirror is designed according to the RICH 1 specifications so that, if acceptable, it can be installed as a final RICH 1 mirror.

A number of pits are present in the optical surface of the mirror due to a defect in the glass-coating process. The glass layer is non-uniform and a smooth increase in thickness is observed towards the edges farthest from the mirror mount point. The variation in glass thickness represents a correction to the radius of curvature of the beryllium substrate.

The mirror was found to have a radius of curvature, R, of $2675 \pm 1\,\mathrm{mm}$ and a spot diameter, D_0, of $3.33 \pm 0.02\,\mathrm{mm}$. The mirror radius of curvature satisfies the requirement of $R = 2700\,\mathrm{mm} \pm 1\%$ but the mirror spot size is slightly larger than the specification of $D_0 < 2.5\,\mathrm{mm}$. The mirror was deemed suitable for use in RICH 1 but contractual difficulties with the blank manufacturer forced a change in the preferred mirror technology choice.

The ability of LHCb to perform a measurement of the parameter a^s_{fs}, which parameterises $\mathcal{CP}$ violation in B^0_s mixing, was investigated. The parameter is extracted from time-dependent, untagged decay-rate asymmetries in decays to semileptonic and hadronic flavour eigenstates, as proposed in [65]. In the expression for the time-dependent asymmetry, acceptance effects due to the LHCb trigger cancel. The measured asymmetry depends on a^s_{fs} itself, the B-production asymmetry, A_P, and the charge detection asymmetry, A_C. Two of these three parameters can be extracted simultaneously, the third needs to be measured externally.

A fast Monte Carlo generator was written which can simulate the untagged decay data of B-mesons. The generator was used to determine the sensitivity to both a^s_{fs} and the B-meson production asymmetry. The detection asymmetry was assumed to be well-known and background effects were ignored. With this we find a statistical precision on a^s_{fs} of $\sim 0.2\%$ for $1M$ events for all values of a_{fs}. For $2\,\mathrm{fb}^{-1}$ of LHCb data, this corresponds to $\sigma_{a^s_{fs}} \sim 0.2\%$ in the $\mathrm{D_s} \to \mathrm{D_s}\mu\nu$ channel, and $\sigma_{a^s_{fs}} \sim 0.5\%$ for $\mathrm{B}^0_\mathrm{s} \to \mathrm{D_s}\pi$. This represents a factor of ten improvement compared to the current direct measurement by DØ.

Appendix A

Pythia Parameters

Settings used in the tuning process described in chapter 4 are given. Parameters which differ from the PYTHIAv6.226 defaults are given in tables A.1 and A.2. Meson production settings are given in table A.1. The settings used for minimum bias production compared to “general” LHCb settings can be found in table A.3.

Parameter	Value	Description
PARJ(1)	0.10	Baryon production
PARJ(2)	0.30	Strangeness production
PARJ(11)	0.50	P(light meson has spin 1)
PARJ(12)	0.60	P(strange meson has spin 1)
PARJ(13)	0.75	P(heavy meson has spin 1) (b,c)
PARJ(14)	0.162	$P(S = 0, L = 1, J = 1)$
PARJ(15)	0.018	$P(S = 1, L = 1, J = 0)$
PARJ(16)	0.054	$P(S = 1, L = 1, J = 1)$
PARJ(17)	0.09	$P(S = 1, L = 1, J = 2)$
PARP(82)	3.39	Multiple interaction regularisation scale, $p_{\perp min}$
PARP(89)	14000.	Reference energy scale
PARP(90)	0.162	Power of $p_{\perp min}$energy rescaling term

Table A.1: Settings which affect heavy and light-meson production (PARJ parameters) and the average multiplicity of non-single-diffractive events (PARP parameters) in the final LHCb tune. Non-zero values of parameters PARJ(14) to PARJ(17) allow B^{**} production.

Parameter	$\sqrt{s}$ =14 TeV	$\sqrt{s}$ <14 TeV	Description
MSEL	0	0	User-selected processes
MSUB(11)	1	1	$f_i f_j \rightarrow f_i f_j$
MSUB(12)	1	1	$f_i \overline{f}_j \rightarrow f_k \overline{f}_k$
MSUB(13)	1	1	$f_i \overline{f}_j \rightarrow gg$
MSUB(28)	1	1	$f_i g \rightarrow f_i g$
MSUB(53)	1	1	$gg \rightarrow f_k \overline{f}_k$
MSUB(68)	1	1	$gg \rightarrow gg$
MSUB(86)	1	0	$gg \rightarrow \mathrm{J}/\psi g$
MSUB(87)	1	0	$gg \rightarrow \chi_{0c} g$
MSUB(88)	1	0	$gg \rightarrow \chi_{1c} g$
MSUB(89)	1	0	$gg \rightarrow \chi_{2c} g$
MSUB(91)	0	0	Elastic scattering
MSUB(92)	1	0	Single diffraction (XB)
MSUB(93)	1	0	Single diffraction (AX)
MSUB(94)	0	1	Double diffraction
MSUB(95)	1	1	Low-$p_\perp$ production
MSUB(106)	1	0	$gg \rightarrow \mathrm{J}/\psi \gamma$
MSTP(2)	2	2	First-order α_s calculation
MSTP(33)	3	3	K factor switch
MSTP(51)	4032	4032	CTEQ 4L PDF library
MSTP(52)	2	2	Proton PDF library choice
MSTP(82)	3	3	Multiple interaction model
MDCY(PYCODE(130),1)	0	0	Turn off $\mathrm{K^0_S}$ decays
MDCY(PYCODE(310),1)	0	0	Turn off $\mathrm{K^0_L}$ decays
MDCY(PYCODE(3122),1)	0	0	Turn off Λ decays
MDCY(PYCODE(-130),1)	0	0	Turn off $\mathrm{K^0_S}$ decays
MDCY(PYCODE(-310),1)	0	0	Turn off $\mathrm{K^0_L}$ decays
MDCY(PYCODE(-3122),1)	0	0	Turn off $\overline{\Lambda}$ decays
MDME(4178,1)	-1	-1	Bug correction

Table A.2: PYTHIAv6.226 settings used in the LHCb tune ($\sqrt{s}$ = 14 TeV) and to simulate minimum bias events at sub-LHC energies ($\sqrt{s}$ < 14 TeV). Meson production settings common to both scenarios are listed in table A.1.

Parameter	Minimum Bias	General	Description
MSEL	0	0	User-selected processes
MSUB(11)	1	1	$f_i f_j \to f_i f_j$
MSUB(12)	1	1	$f_i \overline{f}_j \to f_k \overline{f}_k$
MSUB(13)	1	1	$f_i \overline{f}_j \to gg$
MSUB(28)	1	1	$f_i g \to f_i g$
MSUB(53)	1	1	$gg \to f_k \overline{f}_k$
MSUB(68)	1	1	$gg \to gg$
MSUB(86)	0	1	$gg \to \mathrm{J}/\psi g$
MSUB(87)	0	1	$gg \to \chi_{0c} g$
MSUB(88)	0	1	$gg \to \chi_{1c} g$
MSUB(89)	0	1	$gg \to \chi_{2c} g$
MSUB(91)	0	1	Elastic scattering
MSUB(92)	1	1	Single diffraction (XB)
MSUB(93)	1	1	Single diffraction (AX)
MSUB(94)	0	1	Double diffraction
MSUB(95)	1	1	Low-$p_\perp$ production
MSUB(106)	0	1	$gg \to \mathrm{J}/\psi \gamma$
MSUB(107)	0	1	$g\gamma \to \mathrm{J}/\psi g$
MSUB(108)	0	1	$\gamma\gamma \to \mathrm{J}/\psi \gamma$
MSTP(2)	2	2	First-order α_s calculation
MSTP(33)	3	3	K factor switch
MSTP(51)	4032	4032	CTEQ 4L PDF library
MSTP(52)	2	2	Proton PDF library choice
MSTP(82)	3	3	Multiple interaction model
MDCY(PYCODE(130),1)	0	0	Turn off K^0_S decays
MDCY(PYCODE(310),1)	0	0	Turn off K^0_L decays
MDCY(PYCODE(3122),1)	0	0	Turn off Λ decays
MDCY(PYCODE(-130),1)	0	0	Turn off K^0_S decays
MDCY(PYCODE(-310),1)	0	0	Turn off K^0_L decays
MDCY(PYCODE(-3122),1)	0	0	Turn off $\overline{\Lambda}$ decays
MDME(4178,1)	-1	-1	Bug correction

Table A.3: Comparison of LHCb general settings (including b production, minimum bias events, etc.) and minimum bias settings at 14 TeV. Meson production settings are listed separately in table A.1.

Appendix B

Time-Dependent Decay Rates with Lifetime Resolution

In this appendix, the expressions used in the fast Monte Carlo to generate the asymmetry data discussed in chapter 6 are developed. The expressions can be obtained by convolving the ideal decayrates with a Gaussian of suitable width:

$$\Gamma_i(t) = f_i(a_{fs}) \int\limits_0^\infty e^{-\Gamma t'} \left(\cosh\left(\frac{1}{2}\Delta\Gamma\, t'\right) \pm \cos\left(\Delta m\, t'\right) \right) \frac{1}{\sqrt{2\pi}\sigma} e^{\frac{(t'-t)^2}{2\sigma^2}} dt', \tag{B.1}$$

where the index i labels the four decay rates given in equations 6.12 to 6.15, and f_i is a time-independent parameter that is different for each of the four decay modes. This can be expressed as:

$$\begin{aligned} \Gamma_i(t_0) =& f_i(a_{fs}) \mathsf{Re} \left\{ \frac{1}{\sqrt{2\pi}\sigma} \int\limits_0^\infty e^{-\Gamma t} \left(\frac{1}{2} e^{\frac{1}{2}\Delta\Gamma\, t} + \frac{1}{2} e^{-\frac{1}{2}\Delta\Gamma\, t} \pm e^{i\Delta m\, t} \right) e^{\frac{(t-t_0)^2}{2\sigma^2}} dt \right\} \\ =& f_i(a_{fs}) \mathsf{Re} \left\{ \frac{1}{\sqrt{2\pi}\sigma} \int\limits_0^\infty \left(\frac{1}{2} e^{-(\Gamma - \frac{1}{2}\Delta\Gamma)\, t} + \frac{1}{2} e^{-(\Gamma + \frac{1}{2}\Delta\Gamma)\, t} \pm e^{-(\Gamma - i\Delta m)\, t} \right) e^{\frac{(t-t_0)^2}{2\sigma^2}} dt \right\}. \end{aligned} \tag{B.2}$$

We note that this reduces to calculating

$$\frac{1}{\sqrt{2\pi}\sigma} \int\limits_0^\infty e^{-At} e^{-\frac{1}{2}(t-t_0)^2}\, dt, \tag{B.3}$$

for different (sometimes complex) values of A. Equation B.3 can be re-written as:

$$\frac{1}{\sqrt{2\pi}\sigma} e^{-At_0+\frac{1}{2}A^2\sigma^2} \int\limits_0^\infty e^{-\frac{1}{2\sigma^2}\left(t-\left(t_0-\sigma^2 A\right)\right)^2}\, dt. \tag{B.4}$$

Changing the integration variable to $x \equiv \frac{t}{\sigma}$:

$$\frac{1}{\sqrt{2\pi}\sigma} \int\limits_0^\infty e^{-\frac{1}{2\sigma^2}\left(t-\left(t_0-\sigma^2 A\right)\right)^2}\, dt = \int\limits_0^\infty e^{-\frac{1}{2}\left(x-\left(\frac{t_0}{\sigma}-\sigma A\right)\right)^2}\, dx = \int\limits_{-\infty+\left(\frac{t_0}{\sigma}-\sigma A\right)}^{\left(\frac{t_0}{\sigma}-\sigma A\right)} e^{-\frac{1}{2}x^2}\, dx.$$

For real A:

$$\int\limits_{-\infty+\left(\frac{t_0}{\sigma}-\sigma\, A\right)}^{+\left(\frac{t_0}{\sigma}-\sigma\, A\right)} e^{-\frac{1}{2}x^2}\, dx = \int\limits_{-\infty}^{\left(\frac{t_0}{\sigma}-\sigma\, A\right)} e^{-\frac{1}{2}x^2}\, dx = \mathrm{Freq}\left(\frac{t_0}{\sigma} - \sigma\, A\right) \tag{B.5}$$

where Freq is the frequency function, defined by:

$$\mathrm{Freq}(y) \equiv \int\limits_{-\infty}^{y} e^{-\frac{1}{2}x^2}\, dx. \tag{B.6}$$

The frequency function is related to the more familiar error function by

$$\mathrm{Freq}(y) = \frac{1}{2} + \frac{1}{2}\mathrm{erf}\left(\frac{y}{\sqrt{2}}\right). \tag{B.7}$$

For complex $A = \Gamma - i\Delta m$ we find

$$\frac{1}{\sqrt{2\pi}} \int\limits_{-\infty+\left(\frac{t_0}{\sigma}-\sigma\, A\right)}^{\left(\frac{t_0}{\sigma}-\sigma\, A\right)} e^{-\frac{1}{2}x^2}\, dx = -i\frac{1}{2}\mathrm{erfi}\left(\frac{\Delta m\sigma + i\left(\frac{t_0}{\sigma} - \sigma\Gamma\right)}{\sqrt{2}}\right) + \frac{1}{2}, \tag{B.8}$$

where erfi is the imaginary error function defined by:

$$\mathrm{erfi}(z) = -i\mathrm{erf}(-iz), \tag{B.9}$$

which is related to the complex error function:

$$w(z) = e^{-z^2}\left(1 - i\mathrm{erfi}(iz)\right). \tag{B.10}$$

With this, Equation B.2 becomes:

$$\int_0^\infty e^{-\Gamma t}\left(\cosh\left(\frac{1}{2}\Delta\Gamma\, t\right)\pm\cos\left(\Delta m\, t\right)\right)\frac{1}{\sqrt{2\pi}\sigma}e^{\frac{(t-t_0)^2}{2\sigma^2}}dt =$$

$$\frac{1}{2}\exp\left(-\left(\Gamma-\frac{1}{2}\Delta\Gamma\right)t_0+\frac{1}{2}\sigma^2\left(\Gamma-\frac{1}{2}\Delta\Gamma\right)^2\right)\mathrm{Freq}\left(\frac{t_0}{\sigma}-\sigma\left(\Gamma-\frac{1}{2}\Delta\Gamma\right)\right)$$

$$+\frac{1}{2}\exp\left(-\left(\Gamma+\frac{1}{2}\Delta\Gamma\right)t_0+\frac{1}{2}\sigma^2\left(\Gamma+\frac{1}{2}\Delta\Gamma\right)^2\right)\mathrm{Freq}\left(\frac{t_0}{\sigma}-\sigma\left(\Gamma+\frac{1}{2}\Delta\Gamma\right)\right)$$

$$\pm\mathsf{Re}\Bigg\{\exp\left(-\Gamma\, t_0+\frac{1}{2}\sigma^2\Gamma^2-\frac{1}{2}\Delta m^2\sigma^2\right)\exp\left(i\Delta m\left(t_0-\Gamma\sigma^2\right)\right)$$

$$\times\left(\frac{1}{2}-i\frac{1}{2}\mathrm{erfi}\left(\frac{\Delta m\sigma+i\left(\frac{t_0}{\sigma}-\sigma\Gamma\right)}{\sqrt{2}}\right)\right).\Bigg\} \quad \text{(B.11)}$$

Taking out common factors:

$$\int_0^\infty e^{-\Gamma t}\left(\cosh\left(\frac{1}{2}\Delta\Gamma\, t\right)\pm\cos\left(\Delta m\, t\right)\right)\frac{1}{\sqrt{2\pi}\sigma}e^{\frac{(t-t_0)^2}{2\sigma^2}}dt = e^{-\Gamma t_0}\;e^{\frac{1}{2}\Gamma^2\sigma^2}\Bigg[e^{\frac{1}{8}\sigma^2(\Delta\Gamma)^2}$$

$$\left\{\frac{1}{2}\,e^{\frac{1}{2}\Delta\Gamma\left(t_0-\sigma^2\Gamma\right)}\left(\mathrm{Freq}\left(\frac{t_0}{\sigma}-\sigma\Gamma-\frac{\sigma\Delta\Gamma}{2}\right)+\mathrm{Freq}\left(\frac{t_0}{\sigma}-\sigma\Gamma+\frac{\sigma\Delta\Gamma}{2}\right)\right)\right\}$$

$$\pm e^{-\frac{1}{2}\Delta m^2\sigma^2}\mathsf{Re}\left\{e^{i\Delta m\left(t_0-\Gamma\sigma^2\right)}\times\left(\frac{1}{2}-i\frac{1}{2}\mathrm{erfi}\left(\frac{\Delta m\sigma+i\left(\frac{t_0}{\sigma}-\sigma\Gamma\right)}{\sqrt{2}}\right)\right)\right\}\Bigg]. \quad \text{(B.12)}$$

The expression simplifies significantly if we assume that $t_0 \gg \sigma$, because then the Freq terms tend towards 1 and erfi towards i:

$$\int_0^\infty e^{-\Gamma t}\left(\cosh\left(\frac{1}{2}\Delta\Gamma\, t\right)\pm\cos\left(\Delta m\, t\right)\right)\frac{1}{\sqrt{2\pi}\sigma}e^{\frac{(t-t_0)^2}{2\sigma^2}}dt =$$

$$e^{-\Gamma t_0}\;e^{\frac{1}{2}\Gamma^2\sigma^2}\left[e^{\frac{1}{8}\sigma^2(\Delta\Gamma)^2}\cosh\left(\frac{1}{2}\Delta\Gamma\,\left(t_0-\sigma^2\Gamma\right)\right)\pm e^{-\frac{1}{2}\Delta m^2\sigma^2}\cos\left(\Delta m\left(t_0-\Gamma\sigma^2\right)\right)\right]. \quad \text{(B.13)}$$

The decay rates in equations 6.12 to 6.15 can therefore be re-written as:

$$\Gamma_i(t) =$$

$$f_i(a_{fs})e^{-\Gamma t+\frac{1}{2}\Gamma^2\sigma^2}\left[e^{\frac{1}{8}\sigma^2(\Delta\Gamma)^2}\cosh\left(\frac{1}{2}\Delta\Gamma\left(t-\sigma^2\Gamma\right)\right)\pm e^{-\frac{1}{2}\Delta m^2\sigma^2}\cos\left(\Delta m\left(t-\Gamma\sigma^2\right)\right)\right]. \quad \text{(B.14)}$$

References

[1] T. Sjostrand, S. Mrenna, and P. Skands, JHEP **0605**, 026 (2006), hep-ph/0603175.

[2] J. Charles *et al.*, European Physical Journal C **41**, 1 (2005).

[3] M. Bona *et al.*, J. High Energy Phys. **10**, 081. 16 p (2006).

[4] UA5, G. J. Alner *et al.*, Z. Phys. **C33**, 1 (1986).

[5] CDF, F. Abe *et al.*, Phys. Rev. **D41**, 2330 (1990).

[6] R. Schmidt, Report No. LHC-Project-Report-569. CERN-LHC-Project-Report-569, 2002 (unpublished).

[7] *ALICE Technical Proposal for a Large Ion Collider Experiment at the CERN LHC*, LHC Tech. Proposal (CERN, Geneva, 1995).

[8] W. Kienzle *et al.*, CERN Report No. CERN-LHCC-99-007. LHCC-P-5, 1999 (unpublished).

[9] O. Adriani *et al.*, *LHCf experiment Technical Design Report*, Technical Design Report LHCf (CERN, Geneva, 2006).

[10] R. Antunes-Nobrega *et al.*, *LHCb reoptimized detector design and performance Technical Design Report*, Technical Design Report LHCb (CERN, Geneva, 2003).

[11] P. R. Barbosa-Marinho *et al.*, *LHCb VELO (VErtex LOcator): Technical Design Report*, Technical Design Report LHCb (CERN, Geneva, 2001).

[12] S. Amato *et al.*, *LHCb magnet: Technical Design Report*, Technical Design Report LHCb (CERN, Geneva, 1999).

[13] P. R. Barbosa-Marinho *et al.*, *LHCb online system, data acquisition and experiment control: Technical Design Report*, Technical Design Report LHCb (CERN, Geneva, 2001).

[14] M. Needham and D. Volyanskyy, CERN Report No. LHCb-2006-032. CERN-LHCb-2006-032, 2006 (unpublished).

[15] P. R. Barbosa-Marinho *et al.*, *LHCb outer tracker: Technical Design Report*, Technical Design Report LHCb (CERN, Geneva, 2001).

[16] L. B. A. Hommels, CERN Report No. LHCb-2005-014. CERN-LHCb-2005-014, 2005 (unpublished).

[17] S. Bachmann, CERN Report No. LHCb-2003-053, 2003 (unpublished).

[18] V. P. Zrelov, *Cherenkov radiation in high-energy physics* (ERDA Div. Phys. Res., Washington, DC, 1973), Trans. from the Russsian.

[19] R. W. Forty and O. Schneider, CERN Report No. LHCb-98-040, 1998 (unpublished).

[20] S. Amato *et al.*, *LHCb RICH: Technical Design Report*, Technical Design Report LHCb (CERN, Geneva, 2000).

[21] *LHCb Particle Identification and Performance*, , Lake Louise Winter Institute 2007: Fundamental Interactions, 2007.

[22] S. Amato *et al.*, *LHCb calorimeters: Technical Design Report*, Technical Design Report LHCb (CERN, Geneva, 2000).

[23] H. Fessler *et al.*, Nucl. Instrum. Meth. **A240**, 284 (1985).

[24] P. R. Barbosa-Marinho *et al.*, *LHCb muon system: Technical Design Report*, Technical Design Report LHCb (CERN, Geneva, 2001).

[25] R. Antunes-Nobrega *et al.*, *LHCb trigger system: Technical Design Report*, Technical Design Report LHCb (CERN, Geneva, 2003), revised version number 1 submitted on 2003-09-24 12:12:22.

[26] A. Barczyk, G. Haefeli, R. Jacobsson, B. Jost, and N. Neufeld, CERN Report No. LHCb-2005-062. CERN-LHCb-2005-062, 2005 (unpublished).

[27] E. Rodrigues, CERN Report No. LHCb-2006-065. CERN-LHCb-2006-065, 2006 (unpublished), revised version submitted on 2007-01-26 11:11:17.

[28] L. Fernandez and P. Koppenburg, CERN Report No. LHCb-2005-047. CERN-LHCb-2005-047, 2006 (unpublished), revised version submitted on 2006-08-09 12:16:25.

[29] J. Allison *et al.*, Nuclear Science, IEEE Transactions on **53**, 270 (Feb. 2006).

[30] R. Antunes-Nobrega *et al.*, *LHCb computing: Technical Design Report*, Technical Design Report LHCb (CERN, Geneva, 2005), Submitted on 11 May 2005.

[31] G. Lueders, Annals Phys. **2**, 1 (1957).

[32] I. I. Y. Bigi and A. I. Sanda, *CP violation*, Cambridge monographs on particle physics, nuclear physics, and cosmology (Cambridge Univ. Press, Cambridge, 2000).

[33] A. Lenz and U. Nierste, Theoretical update of B_s-$\overline{B}_s$ mixing, 2006.

[34] W.-M. Yao *et al.*, Journal of Physics G **33**, 1+ (2006).

[35] A. Abulencia *et al.*, Phys. Rev. Lett. **97**, 062003. 7 p (2006).

[36] A. J. Buras, Mnchen Univ. Fachber. Phys. Report No. hep-ph/0307203. TUM-HEP-523, 2003 (unpublished).

[37] Heavy Flavor Averaging Group (HFAG), E. Barberio *et al.*, (2007), arXiv:0704.3575 [hep-ex].

[38] T. Sjostrand, L. Lonnblad, and S. Mrenna, (2001), hep-ph/0108264.

[39] R. Barate *et al.*, Phys. Lett. B **425**, 215. 13 p (1998).

[40] R. J. Akers *et al.*, Z. Phys. C **66**, 19 (1994).

[41] P. Abreu *et al.*, Phys. Lett. B **345**, 598 (1995).

[42] CDF, T. Affolder *et al.*, Phys. Rev. **D64**, 072002 (2001).

[43] H. F. A. Group, Averages of b-hadron properties as of summer 2004, 2004.

[44] F. Abe *et al.*, Phys. Rev. D **41**, 2330 (1990).

[45] A. Donnachie and P. V. Landshoff, Phys. Lett. B **296**, 227 (1992).

[46] W.-K. Tung, H. L. Lai, J. Pumplin, P. Nadolsky, and C. P. Yuan, Report No. arXiv:0707.0275, 2007 (unpublished).

[47] F. James and M. Roos, Comput. Phys. Commun. **10**, 343 (1975).

[48] Brush Wellman Inc., Designing with Beryllium, www.brushwellman.com.

[49] The American Society for Metals, ASM Handbook, www.asm-intl.org.

[50] A. Braem and M. E. Kostrikov, Protvino Inst. High Energy Phys. Report No. IHEP-93-129, 1993 (unpublished).

[51] A. Braem, C. David, and C. Joram, Nucl. Instrum. Meth. **A553**, 182 (2005).

[52] M. Laub, C. D'Ambrosio, and O. Ullaland, *Development of opto-mechanical tools and procedures for the new generation of RICH-detectors at CERN*, PhD thesis, Cesk vysok ucen technick v Praze, Prague, 2001, Presented on 01 Jan 2001.

[53] Z. Ligeti, M. Papucci, and G. Prez, Phys. Rev. Lett. **97**, 101801. 5 p (2006).

[54] U. Nierste, CP asymmetry in flavour-specific B decays, 2004, hep-ph/0406300.

[55] O. Leroy, F. Muheim, S. Poss, and Y. Xie, CERN Report No. LHCb-2007-029. CERN-LHCb-2007-029, 2007 (unpublished).

[56] J. Borel, L. Nicolas, O. Schneider, and J. Van Hunen, CERN Report No. LHCb-2007-017. CERN-LHCb-2007-017. LPHE Note 2007-03, 2007 (unpublished).

[57] O. Schneider, Review of particle physics, 2006.

[58] S. Laplace, Z. Ligeti, Y. Nir, and G. Perez, Physical Review D **65**, 094040 (2002).

[59] E. Norrbin and T. Sjostrand, European Physical Journal C **17**, 137 (2000).

[60] V. M. Abazov *et al.*, FERMILAB Report No. hep-ex/0701007. FERMILAB-PUB-2007-005-E, 2007 (unpublished).

[61] V. M. Abazov *et al.*, Report No. hep-ex/0702030, 2007 (unpublished).

[62] T. Aaltonen and A. Other, Measurement of CP Asymmetry in Semileptonic B Decays, 2007.

[63] G. COWAN, *Statistical data analysis* (Clarendon Press, Oxford, 1998).

[64] F. E. James, *Statistical methods in experimental physics* (World Scientific, Singapore, 2006).

[65] I. Dunietz, R. Fleischer, and U. Nierste, Physical Review D **63**, 114015 (2001).